Antarctic-like temperature variations in the Tropical Andes recorded by glaciers and lakes during the last deglaciation

L. C P Martin, P.-H Blard, J Lavé, Vincent Jomelli, J. Charreau, T. Condom, M. Lupker, Maurice Arnold, Georges Aumaitre, D.L. L Bourlès, et al.

Antarctic-like temperature variations in the Tropical Andes recorded by glaciers and lakes during the last deglaciation

L.C.P. Martin[a,b*], P.-H. Blard[a,c*], J. Lavé[a], V. Jomelli[d,e], J. Charreau[a], T. Condom[f], M. Lupker[g], ASTER Team[e#]

a. CRPG, UMR7358 CNRS - Université de Lorraine, 54500 Vandœuvre-lès-Nancy, France
b. Department of Geosciences, University of Oslo, P.O. Box 1047, Blindern, 0316 Oslo, Norway
c. Laboratoire de Glaciologie, DGES-IGEOS, Université Libre de Bruxelles, 1050 Brussels, Belgium
d. Université Paris 1 Panthéon-Sorbonne, CNRS Laboratoire de Géographie Physique, Meudon, France
e. Aix-Marseille Université, CNRS-IRD-Collège de France-INRAE, UM 34 CEREGE, Aix-en-Provence, France
f. Université Grenoble Alpes, CNRS, IRD, G-INP, Institut des Geosciences de l'Environnement (IGE) – UMR 5001, Grenoble, France
g. ETH, Geological Institute, Sonneggstrasse 5, 8092 Zurich, Switzerland

M. Arnold, G. Aumaître, D. L. Bourlès, K. Keddadouche

* Corresponding authors:

leo.doug.martin@gmail.com; blard@crpg.cnrs-nancy.fr
Centre de Recherches Pétrographiques et Géochimiques
15 rue Notre Dame des Pauvres
54501 Vandœuvre-lès-Nancy
France

- Words: 14,986
- Tables: 7
- Figures: 18
- Supplementary Information: 1,247 words, 3 Tables,4 figures

Keywords: paleoclimate dynamics; Tropical Andes; paleoglaciers; cosmogenic nuclides; ^{10}Be, ^{3}He; glacial geomorphology; last deglaciation; Termination 1; continental paleotemperature and precipitation reconstruction, global and regional climate.

Highlights

- Cosmic ray exposure ages and paleo-ELAs determined for Bolivian Andes late-glacial moraines
- New ^{14}C shoreline ages constrain the depth of paleolake Coipasa (~12.5 cal kyr BP)
- Temperature and precipitation reconstructed from coupled glacier-lake modeling
- Lake-induced precipitation recycling effect accounted in reconstruction
- Precipitation modulated by Northern Hemisphere, temperatures by Antarctic during 19–11 ka BP

Abstract

The respective impacts of Northern and Southern Hemispheric climatic changes on the Tropics during the last deglaciation remain poorly understood. In the High Tropical Andes, the Antarctic Cold Reversal (ACR, 14.3-12.9 ka BP) is better represented among morainic records than the Younger Dryas (12.9-11.7 ka BP). However, in the Altiplano basin (Bolivia), two cold periods of the Northern Hemisphere (Heinrich Stadial 1a, 16.5-14.5 ka BP, and the Younger Dryas) are synchronous with (i) major advances or standstills of paleoglaciers and (ii) the highstands of giant paleolakes Tauca and Coipasa.

Here, we present new cosmic ray exposure (CRE) ages from glacial landforms of the Bolivian Andes that formed during the last deglaciation (Termination 1). We reconstruct the equilibrium line altitudes (ELA) associated with each moraine and use them in an inverse algorithm combining paleoglaciers and paleolake budgets to derive temperature and precipitation during the last deglaciation.

Our temperature reconstruction (ΔT relative to present day) yields a consistent regional trend of progressive warming from $\Delta T = -5$ to -2.5 °C during 17–14.5 ka BP, followed by a return to colder conditions around –4°C during the ACR (14.5-12.9 ka BP). The Coipasa highstand (12.9-11.8 ka BP) is coeval with another warming trend followed by ΔT stabilization at the onset of the Holocene (ca. 10 ka BP), around –3°C. Our results suggest that, during the last deglaciation (20 – 10 ka BP) atmospheric temperatures in the Tropical Andes mimicked Antarctic variability, whereas precipitation over the Altiplano was driven by changes in the Northern Hemisphere.

1. Introduction

The last deglaciation was characterized by major reorganizations of the continental and oceanic climate systems, including modifications of oceanic circulations (McManus et al., 2004), and the monsoon systems (Cruz et al., 2005), shifts of the wind belts (Denton et al., 2010; Toggweiler, 2009), and opposing north/south temperature variations (Barker et al., 2009; Broecker, 1998). During this period, antiphase warming/cooling events (such as the Northern Hemisphere, NH, warm Bølling-Allerød and the Southern Hemisphere, SH, Antarctic Cold Reversal, Andersen et al., 2004; Jouzel et al., 2007) may have influenced both hemispheres and triggered major continental hydro-climatic changes (e.g. Barker et al., 2011; Blard et al., 2011a, 2009; Broecker and Putnam, 2012; Jomelli et al., 2014; Martin et al., 2018; Placzek et al., 2006; Sylvestre et al., 1999). However, the respective interhemispheric impacts of oceanic and atmospheric changes remain controversial and the subject of various investigations (e.g. Blard et al., 2009; Fritz et al., 2007; Jomelli et al., 2014).

Because the tropics are intersectional between the Northern and Southern Hemispheres, this region is key to addressing the respective impacts of both hemispheres on global and regional climates (Jackson et al., 2019). The Tropical Andes, and particularly the Altiplano Basin, exhibit outstanding hydro-climatic archives of climatic changes during the last deglaciation. Indeed, the Antarctic Cold Reversal (a SH event) was reported to have exerted a major influence on glacial dynamics throughout the tropical and sub-tropical Andes (Jomelli et al., 2014). Furthermore, in the Altiplano, paleo-highstands of Lakes Tauca (52,000 km^2) and Coipasa (32,000 km^2) are synchronous with the second half of the Heinrich Stadial 1 (16.5 – 14.5 ka BP) and the Younger Dryas (12.9 – 11.7 ka BP), respectively (NH events, Blard et al., 2011a; Placzek et al., 2006; Sylvestre et al., 1999). These lake cycles are characterized by abrupt transgressions and regressions within 1 kyr, implying drastic and fast climatic changes that occurred synchronously with abrupt changes within the northern Atlantic region (Andersen et al., 2004; McManus et al., 2004). Throughout the Altiplano Basin, moraine records evidence glacial standstills or re-advances synchronous with the Lake Tauca highstand, which Martin et al. (2018) used to reconstruct the regional distribution of precipitation during Heinrich Stadial 1 (16.5 – 14.5 ka BP), for which they computed a regional precipitation increase of 130% (i.e. a factor of 2.3).

Relying on their reconstructed spatial distribution of precipitation, they concluded that the change in rainfall regime during Heinrich Stadial 1 resulted from modifications of the South American Summer Monsoon (SASM), involving a southward shift of synoptic atmospheric features compared to the present.

Numerous studies have provided local chronologies of glaciers fluctuations in the tropical Andes for the last glacial maximum (LGM) and late-glacial period (e.g. Bromley et al., 2016; Carcaillet et al., 2013; Farber et al., 2005; Palacios et al., 2020; Shakun et al., 2015; Smith, 2005; Ward et al., 2015; Zech et al., 2009) and climatic reconstructions from glacial landforms in the vicinity of the Altiplano have already been reported (Jomelli et al., 2011; 2016, Kull et al.,, 2008; Kull and Grosjean, 2000; Malone et al., 2015). In the Altiplano, Blard et al. (2009) and Placzek et al. (2013) quantified temperature variations based on joint lake- and glacier-budget calculations during the Lake Tauca cycle. However, these previous approaches suffered from substantial uncertainties on the spatial distribution of precipitation over the Altiplano because very few climatic reconstructions are available before and after the Lake Tauca highstand. Notably, little is known about Tropical Andean temperatures and precipitation during the LGM-Heinrich 1 transition, the ACR and the Younger Dryas. In this regard, climatic reconstructions spanning the last deglaciation in the High Tropical Andes are critical to establishing the extent and influence of these major and potentially opposing climatic changes recorded at high latitudes of the Northern and Southern Hemisphere.

Here we present new glacial chronologies from four sites of the Bolivian Altiplano: the Zongo valley (16.3°S, 68.1°W), Nevado Sajama (18.1°S, 68.9°W), Cerro Tunupa (19.8°S, 67.6°W), and Cerro Luxar (21.0°S, 68.0°W). These chronologies are based on cosmic ray exposure (CRE) dating of recessional moraine sequences and glacially abraded bedrock surfaces. These new data extend the existing chronologies of Smith et al. (2005), Jomelli et al. (2011), Blard et al. (2009, 2013) and Martin et al. (2018). Considering lake-level variations over the same period, we applied an inversion method that builds on our previous studies (Blard et al. 2009, Martin et al. 2018). By coupling glacier- and lake-budget calculations, we took advantage of their contrasting sensitivities to temperature and precipitation, and reconstructed temperature and precipitation ranges that jointly satisfy glacial and lacustrine extents for a given moment of the last deglaciation.

2. Geological Setting

2.1. Climate of the Altiplano

The Altiplano is a wide intra-mountain plateau covering an area of 196,000 km^2 and bounded by the eastern and western Andes Cordilleras (Fig. 1). Due to its regional topography, this area is an endorheic basin (hereafter, the "Altiplano Basin"). This basin extends from 15.5°S (Peru) to 22.5°S (Bolivia), and ranges in elevation from 3,658 m above sea level (asl) at Salar de Uyuni to 6,542 m asl at Sajama volcano.

The precipitation regime of the Altiplano is under the climatic influence of the SASM, which brings most of the annual rainfall during the austral summer (December, January, February, Vera et al., 2006; Zhou and Lau, 1998). During this period, the dry westerlies are weakened by subtropical jet modulations and a concomitant southward expansion of the tropical easterlies. This modification promotes the transport of humidity from the Amazonian basin and central Brazil towards the Altiplano (Garreaud et al., 2003, 2009; Segura et al., 2019; Vuille, 1999; Vuille and Keimig, 2004). The orographic effect of the Eastern Cordillera modulates this transport and creates an important precipitation gradient over the Altiplano. Annual rainfall presently ranges from 800 mm on the shores of Lake Titicaca to 60 mm in the vicinity of the Laguna Colorada, southwest Bolivia (Fig. 1).

Present temperatures are relatively uniform over the Altiplano, and the daily temperature variability is larger than the seasonal variability (Aceituno, 1996) as is often observed in the tropics (Hastenrath, 1991). Maximum daily temperatures occur around 2 pm LT when solar radiation is maximal. For most of the year, daily temperature variations are constrained by night radiative loss from the surface. Therefore, the daily amplitude of temperature variations is reduced during the wet season when cloudiness is important (Condom, 2002). Climatic conditions at the glacial sites are presented in Table 1.

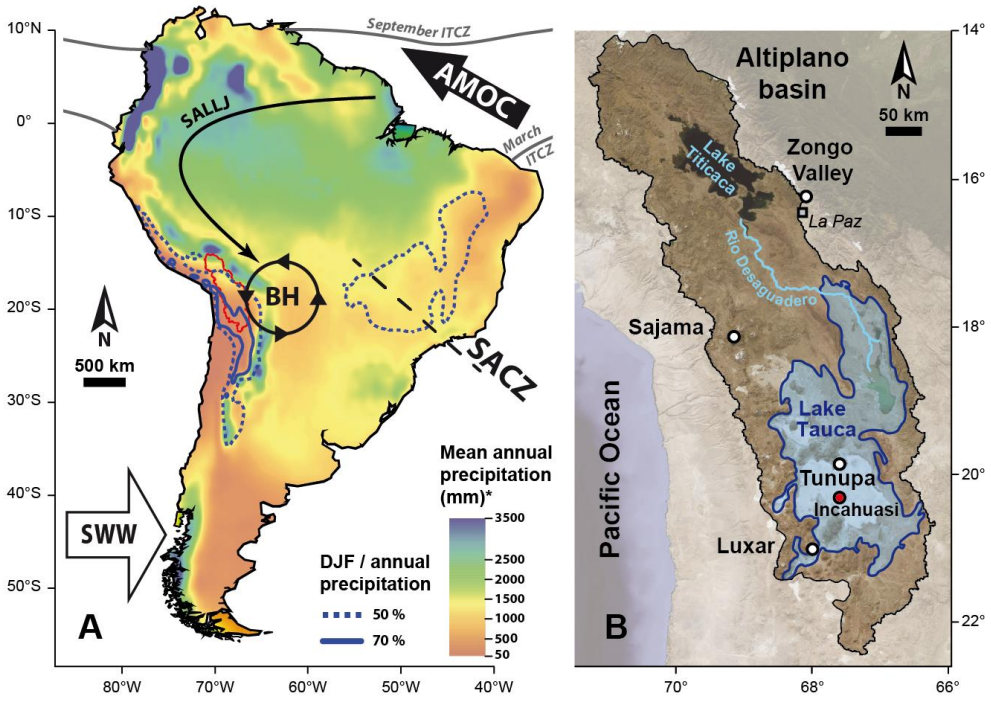

*Figure 1. South American climate and the Altiplano Basin. (A) Modern features of the South American climate, with particular focus on the summer monsoon. SWW, southern westerly winds; AMOC, Atlantic meridional overturning circulation; ITCZ, intertropical convergence zone; SALLJ, South American low-level jets; SACZ, South Atlantic convergence zone; BH, Bolivian High. The colored background indicates mean annual rainfall (*color scale truncated at 3,500 mm). Blue contours show the December–February (DJF) to annual precipitation ratio. Precipitation data are mean values during 1979–2016 from ERA-Interim (Dee et al., 2011). (B) The Altiplano Basin and the locations of sites analyzed herein overlaid on SPOT Imagery. White dots indicate glacial valleys, and the red dot indicates lacustrine deposits sampled and analyzed herein. The maximum paleo-extent of Lake Tauca is shaded in blue. The black line delimits the Altiplano endorheic basin.*

2.2. Altiplano hydrology and paleolake records

The Altiplano endorheic basin comprises a north-south succession of four adjacent sub-basins (Fig. 2). The Titicaca watershed in the northern Altiplano is the highest (lake altitude, 3,812 m asl) and wettest sub-basin. It drains to the southeast via Rio Desaguadero (Figs. 1 and 2) to the Poopo watershed. Lake Poopo was a shallow lake (<3 m deep) that vanished in 2015 due to ongoing climate change and excessive irrigation (Satgé et al., 2017). The small Coipasa watershed is to the southwest of Poopo watershed, and the two are separated by an elevation threshold of 3,703 m asl (Fig. 2). The Uyuni watershed (bottom at 3,660 m asl) is to the south of Coipasa watershed, from which it is separated by an elevation threshold of 3,672 m asl. Channels and paleochannels between the different basins indicate that they were hydrologically connected during wetter periods.

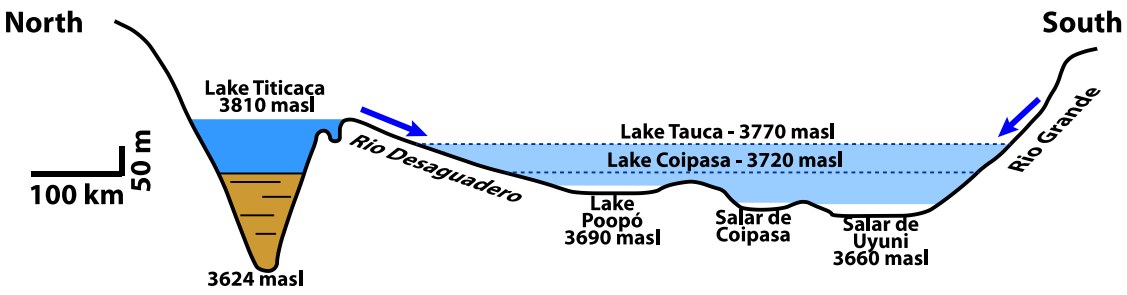

Figure 2. Topographic cross section of the Altiplano showing the hydrological relationships between lake and salar watersheds (modified from Argollo and Mourguiart, 2000). The threshold between the Poopo and Coipasa watersheds is 3,703 m asl. The threshold between the Coipasa and Uyuni watersheds is 3,672 m asl. The elevation reported for paleolake Coipasa is based on our new shoreline ^{14}C ages (see Section 4.1.1).

The three southernmost basins of the Altiplano are dry at present, but were covered by large lakes during the wettest periods of the Quaternary (Placzek et al., 2006; Sylvestre et al., 1999). Of the several lake episodes that occurred during the last 120 kyr, the Lake Tauca episode was the widest and deepest (~110 to 120 m deep, Placzek et al., 2006; Blard et al., 2011). During the Lake Tauca highstand (3,770 m asl), the lake extent covered the totality of the three southernmost basins (Poopo, Coipasa and Uyuni; Figs. 1 and 2).

U-Th and ^{14}C dating of its shorelines constrain the timing of the Lake Tauca cycle, i.e. the transgression (18-16.5 ka BP), highstand (16.5-15.5 ka BP) and regression phases (14.5-13.5 ka BP, Blard et al., 2013a). During its highstand, the lake level reached a maximum altitude of 3,770 m asl and covered 52,000 km^2. The Coipasa Lake cycle is characterized by a transgression from 13.3 to 12.9 ka BP, a highstand from 12.9 to 11.8 ka BP and a regression from 11.8 to 10.2 ka BP (Blard et al., 2011a; Placzek et al., 2006; Sylvestre et al., 1999). Placzek et al. (2013) reported that the highstand lake level reached 3,700 m asl, covering 28 400 km^2.

To expand the existing age dataset, we sampled two new bioherms on Isla Incahuasi (20.24°S - 67.62°W, Table 2), a rocky hill in the center of Salar de Uyuni (Fig. 3). The first bioherm lies 5 m below the top of the hill (3,715 masl). Dislocations in the calcareous crust revealed a radial cross section of its cortical structure. We took advantage of this exposure and sampled the outermost cortex (INC-13-1), which presents a fine radial branching structure, and a more inner region of the bioherm (INC-13-2),

exhibiting a massive algal facies with no visible laminations. The second bioherm is located atop the hill (3,720 m asl), and we sampled the outermost cortex (INC-13-3).

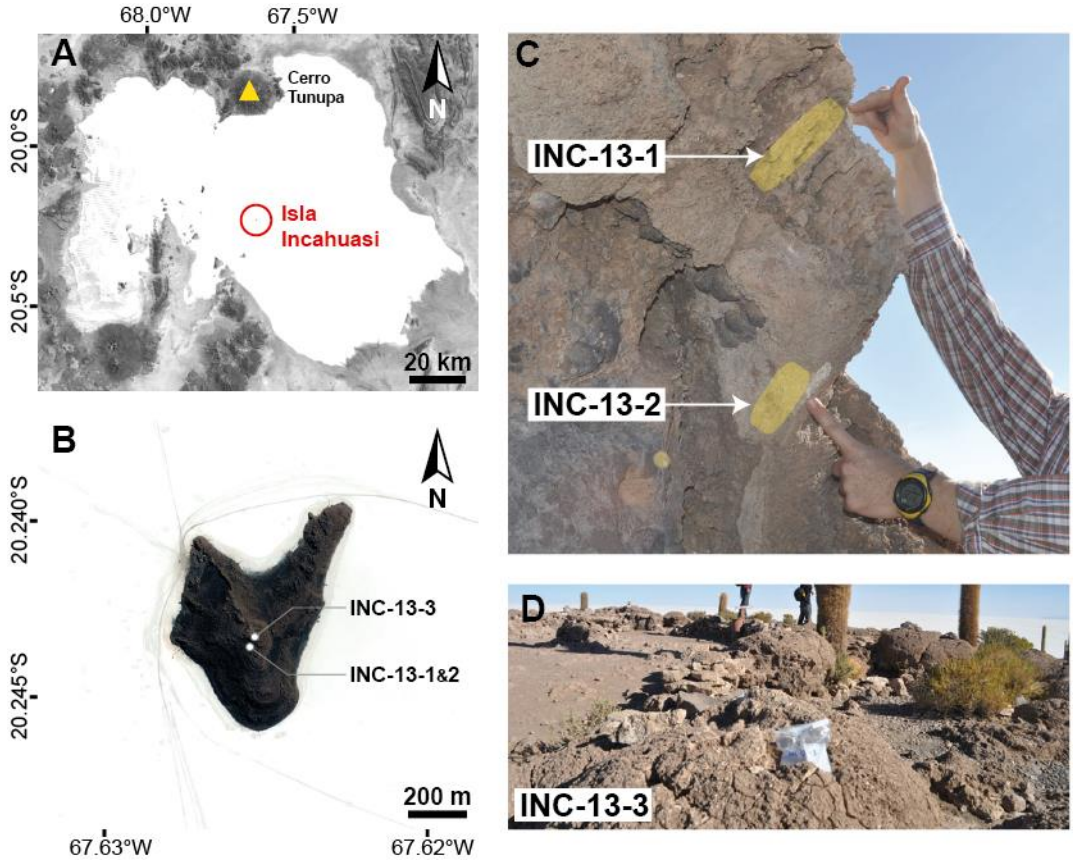

Figure 3. Bioherm samples on Isla Incahuasi. (A) The location of Isla Incahuasi within Salar de Uyuni. (B) Bioherm sampling locations on Isla Incahuasi. (C) INC-13-1 and INC-13-2 sample different parts of the same bioherm; yellow shaded areas indicate the sampled portions of the bioherm. (D) Sample INC-13-3 atop the hill.

2.3. Moraine Settings

The four paleoglaciated sites presented in this study span the latitudinal range from 16.3°S to 21.0°S (Fig. 1).

2.3.1. Zongo Valley (16.2°S - 68.1°W)

Zongo valley is in the Cordillera Real in the northern part of the Bolivian Altiplano (Fig. 1). It is a northward-orientated valley, draining a mountainous area of about 150 km^2 towards the Amazonian basin and culminating at Huayna Potosi (6,088 m asl). Presently glaciated areas have small extents. Huayna Potosi presently bears a retreating slope glacier on its southern face which has been monitored by the IRD-GREAT ICE team since 1991 (Rabatel et al., 2013; Soruco et al., 2009). Other summits in

194 the valley (Telata, Charquini) only bear small glaciers or perennial snow patches. The valley exhibits
195 geomorphic evidence of important past glaciations including several moraines and roches moutonnées.
196 This part of the Cordillera Real massif mainly comprises granitic rocks. The glacial geomorphic features
197 of Zongo Valley are thus suitable for CRE dating by measuring ^{10}Be in quartz. Such data have already
198 been reported for this valley (Jomelli et al., 2011; Martin et al., 2018; Smith et al., 2005). We sampled
199 23 new moraine boulders and combined our and previous results to better constrain the timing of the
200 deglaciation in the valley (Fig. 4, Table 3).

201 The different moraines are classified into four groups. The Cerro Illampu group (green moraines
202 on Fig. 4) includes the five most distal moraines (IP1 to 5) and a perched frontal moraine left by a small
203 glacier of local origin (IPα). Moraines IP1 to 5 are LGM moraines studied by Smith et al. (2005) and
204 Martin et al. (2018). Downstream from these moraines, glacial morphologies vanish and the U-shaped
205 valley gradually becomes V-shaped, indicating the former extent of past glacial activities. IP1 to 3 are
206 lateral moraines and IP4 and 5 are frontal moraines in the bottom of the valley. Due to their distal
207 position in the valley, the former ice tongues associated with moraines IP1 to 3 resulted from the
208 convergence of 5 ice streams flowing down from Huayna Potosi, Charquini, Telata, Cerro Illampu and
209 Jiskha Choquela (Fig. 4A). The IP 4 and 5 ice tongues flowed from the Cerro Illampu summit alone.

210 The Main Valley (MV) moraine gathers a complex of small recessional (lateral and frontal)
211 moraines that lie upstream within a portion of the Zongo valley that flows straight north (Fig. 4A). The
212 associated ice tongue resulted from the convergence of ice flows from Huayna Potosi, Cerro Charquini
213 and Cerro Telata. The T1 to T3 moraines are associated with ice flows downstream from Cerro Telata.
214 These sets of frontal moraines were dated to the Pleistocene - Holocene transition by Jomelli et al.
215 (2011). CQ1 and CQ3 are lateral moraines and CQ4 is a frontal moraine. Whereas the ice tongue
216 associated with CQ1 must have resulted from the convergence of ice streams from Huayna Potosi and
217 Charquini, CQ3 and CQ4 are only associated with downstream ice flows from Cerro Charquini. The
218 MV and CQ moraines were sampled for the present study (see Table 3). From IP1 to CQ4, the glacial
219 record spans over 15 km horizontally and over 1200 m vertically. Examples of collected samples are
220 shown on Fig. 5.

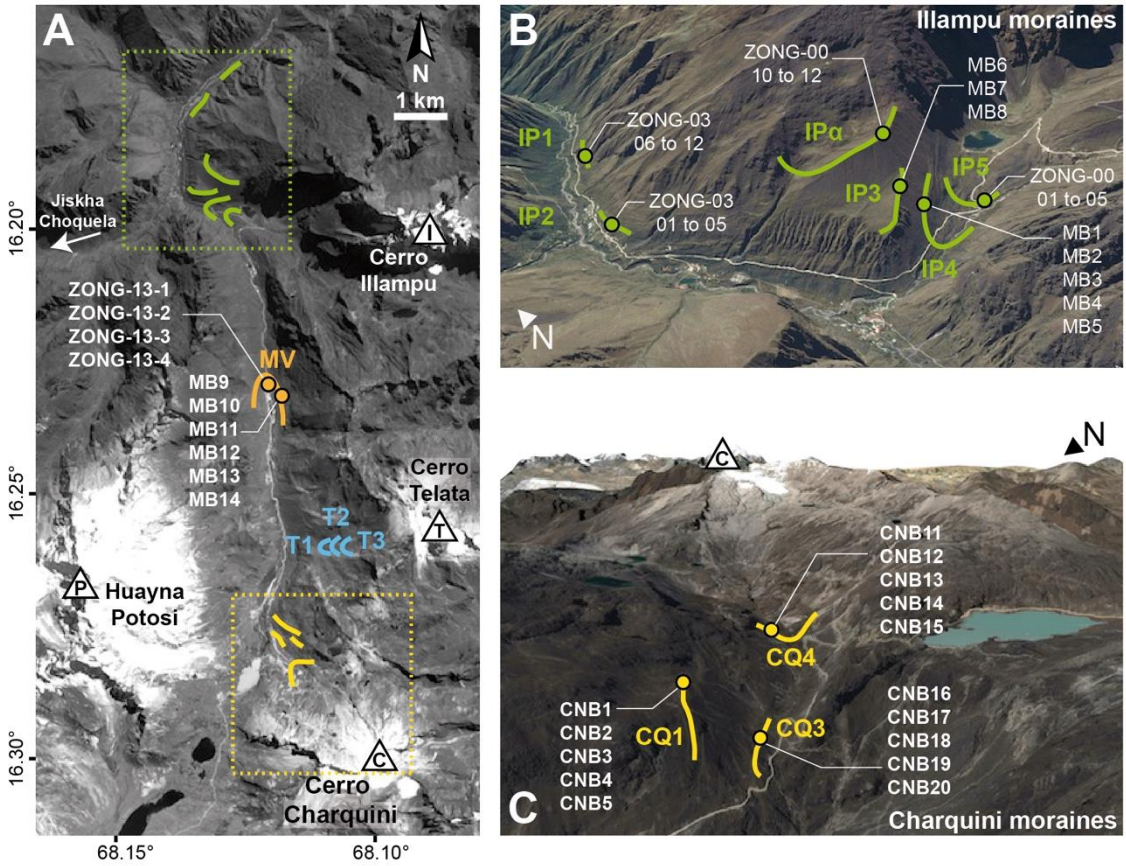

Figure 4. Moraine samples in Zongo Valley. (A) Overview of moraine groups and samples. (B) Cerro Illampu moraines (sample numbers from Smith et al., 2005 and Martin et al., 2018). (C) Charquini moraines. Sample names in bold font are original samples from this study (MV and CQ groups). Samples from the T moraine group (blue) are from Jomelli et al. (2011), and are not detailed here (see Table 3).

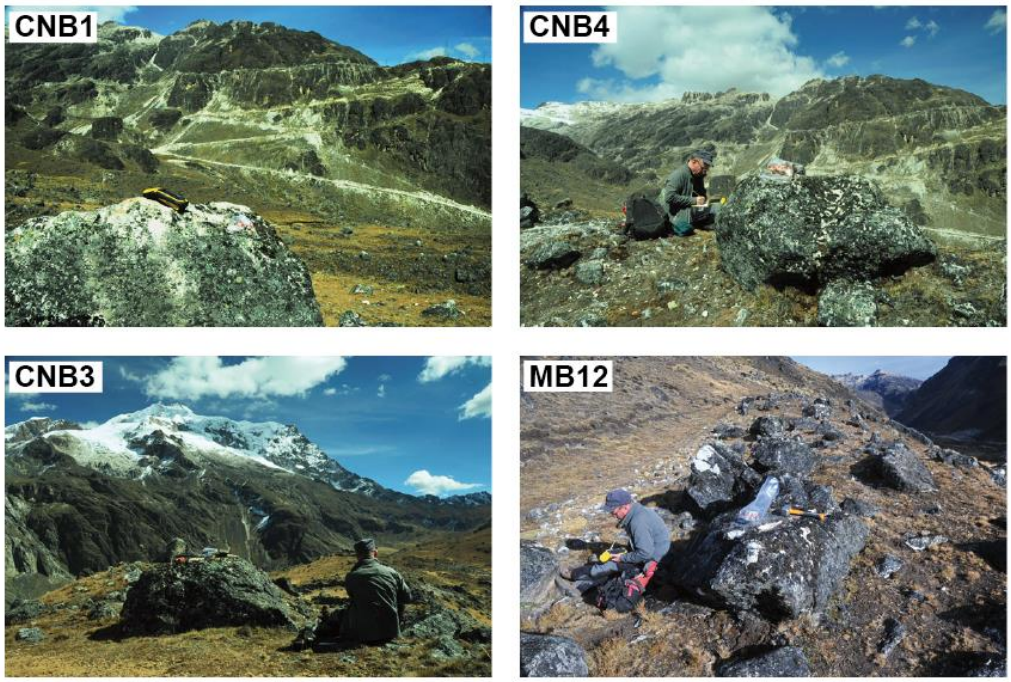

Figure 5. Examples of sampled boulders in Zongo Valley. Samples shown here belong to the CQ1 (CNB1, 3, and 4) and MV (MB12) moraines.

2.3.2. Nevado Sajama (18.1°S - 68.9°W)

Nevado Sajama is an andesitic and rhyodacitic stratovolcano in the western part of the central Altiplano, and the highest summit of Bolivia (6,542 m asl). Nevado Sajama presently bears a small ice cap of ~5 km^2 spanning 5,500–6,500 m asl. Larger past glacial activities carved numerous glacial valleys into the flanks of the volcano radiating from the summit. We collected 18 samples on four moraines and three roches moutonnées in the main southward valley of Nevado Sajama, where a former glacier left a prominent moraine and smaller cordons (Fig. 6). The M1 moraine was CRE dated (^{3}He in pyroxenes) at 15.1 ± 1.1 ka BP by Martin et al. (2018).

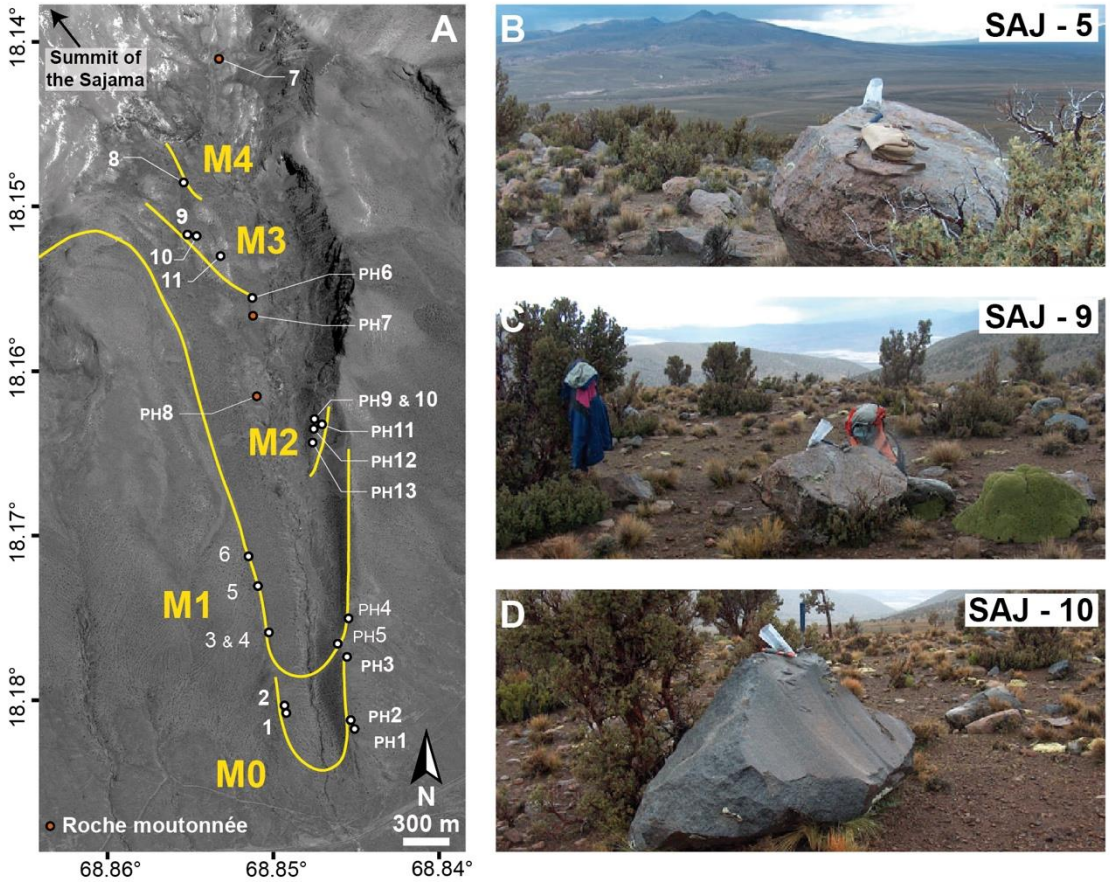

Figure 6. Moraine and roche moutonnée samples in the main southward valley of Nevado Sajama. (A) Detailed samplings of each moraine. White and orange dots indicate morainic boulder and roches moutonnées samples, respectively. Solid yellow lines delimit the moraines in the main scope of this study. Full sample names include the prefix 'SAJ-'. Only samples listed in bold font are from this study (i.e. all samples except those from M1, which are from Martin et al., 2018). (B–D) Representative morainic boulder samples.

Terminal moraine M0 was formed by the maximal ice extent in the valley, and M1–4 are recessional moraines deposited subsequently. These moraines lie in the bottom part of the valley, towards the southwest. The terminus of M1 is 700 m upstream from that of M0 (horizontal distance);

M1 is more sharp-crested than M0 and was built laterally atop M0 lateral moraines. Recessional moraines M2 and M3 are probably associated with short standstills as they are much smaller than M1. Additionally, the geometry of M3 suggests a narrower ice flow associated with a reduced upstream accumulation area (Fig. 6). Two roches moutonnées were sampled between M2 and M3 (SAJ-PH7 and SAJ-PH8) and another upstream of M4 (SAJ-7). This glacial record spans over 5 km horizontally and over 300 m vertically. The andesitic composition of the samples led us to establish CRE ages from in-situ cosmogenic ^{3}He concentrations in pyroxenes. CRE ^{36}Cl ages reported by Smith et al. (2009) for the eastward valleys of Nevado Sajama indicate late-glacial and Holocene moraines. Scatter among their samples from the late-glacial period precludes a precise chronology.

2.3.3. Cerro Tunupa (19.8°S - 67.6°W)

Cerro Tunupa (summit elevation, 5,321 m asl) is an andesitic stratovolcano in the center of the southern Altiplano, above the northern edge of Salar de Uyuni. Cerro Tunupa does not presently bear permanent ice cover, although numerous glacial landforms are preserved in its southern flank (Blard et al., 2009; Clayton and Clapperton, 1997). Chalchala valley is the main glacial valley, extending from the glacial cirque towards the southeast. Downstream, the glacial carving gradually disappears and the valley widens on the Chalchala glacial fan (Fig. 7). In this valley, Blard et al. (2009, 2013a) studied four moraines (M0–3) and the Chalchala fan delta (Fig. 7). M0 is a pre-LGM moraine outlet cross-cut by moraine M1. M1 and M2 have cosmogenic ^{3}He exposure ages contemporaneous with the Lake Tauca highstand (Blard et al., 2009, 2013a). Martin et al. (2018) recalculated the age of M2 to be 15.7 ± 0.6 ka BP based on the data of Blard et al. (2009) and additional Bayesian conditions based on the upper-lying roche moutonnées TU-2 and TU-4. The recession indicated by M3 was dated to 14.5 ka BP by Blard et al. (2009, 2013).

As shown on Fig. 7, the lateral part of M2 was sampled but evidence of its frontal part remains unclear. The M3 moraine complex corresponds to small ice tongues that stood as the downstream digitations of a small-extent cirque glacier. A complete description of the Chalchala moraines is available in Blard et al. (2009). Samples from the Chalchala valley span over 400 m vertically and 4 km horizontally.

In this study, we completed the sampling of the M3 moraine complex. We sampled two new roches moutonnées and six new morainic boulders (sample names including "13"). These samples were collected for CRE age determinations from in-situ ^{3}He concentrations in pyroxenes.

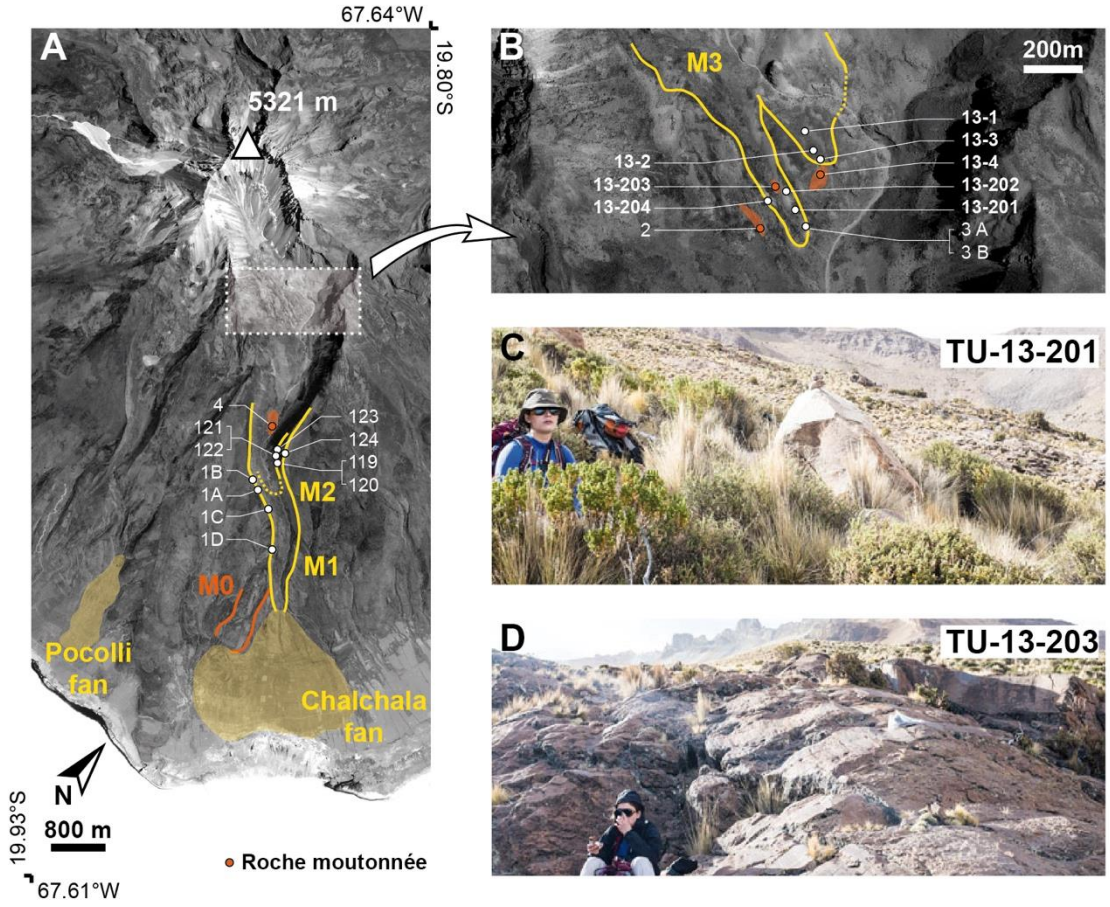

Figure 7. Moraine samples on Cerro Tunupa. (A) Location of the moraines and samples in the main glacial valley. White and orange dots indicate morainic boulder and roches moutonnées samples, respectively. Solid yellow lines delimit the moraines in the main scope of this study. (B) Enlarged view of the upstream samples associated with the M3 morainic complex. (C) The TU-13-201 moraine boulder. (D) The TU-13-203 roche moutonnée. Full sample names include the prefix 'TU-'. Only samples labelled in bold font are from this study (samples including "13-" in (B)); other samples were presented in Blard et al. (2009, 2013a).

2.3.4. Cerro Luxar (21.0°S - 68.0°W)

Cerro Luxar is an andesitic stratovolcano in the southwestern Altiplano, 70 km south of Salar de Uyuni; it belongs to a wide volcanic province extending from the western Cordillera to the center of the Altiplano. Cerro Luxar does not currently have permanent ice cover, but numerous glacial geomorphic features are observed in the valleys carved into its flanks. Because of the andesitic composition of the Luxar volcano, in-situ cosmogenic ^{3}He concentrations in pyroxenes can be used to date the glacial features. The M1 moraine (Fig. 8) is the terminal moraine, corresponding to the last maximal extent of the ice tongue; it is a sharp-crested moraine extending continuously over more than 1 km and delimiting a narrow and sinuous ice tongue. The M2 and M3 moraines are recessional moraines located upstream in the valley. M2 extends over 500 m on the left bank and over 200 m on the right bank. Martin et al. (2018) measured exposure ages on morainic boulders of moraines M1 and M2 (Fig. 8) and dated them at 16.6 ± 0.7 ka BP and 15.4 ± 0.9 ka BP, respectively. Here we extend their results with two samples on boulders of moraine M3 (sampled on the more prominent right bank) and two upper-lying roches moutonnées (located upstream of the three moraines, in the glacial cirque). Combined with the samples of Martin et al. (2018), this glacial landform record spans 1.2 km horizontally and 450 m vertically.

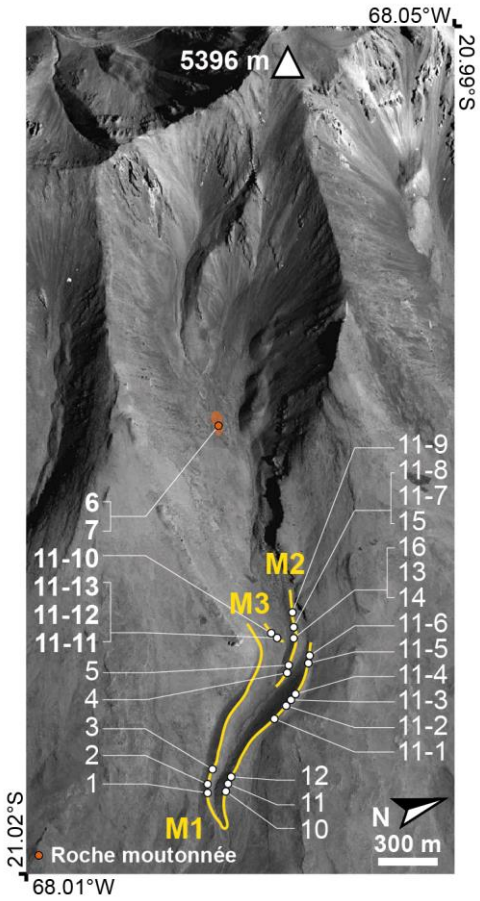

Figure 8. Moraine samples on Cerro Luxar detailed on a map of the valley. White and orange dots indicate morainic boulder and roches moutonnées samples, respectively. Solid yellow lines delimit the moraines in the main scope of this study. Full sample names include the prefix 'LUX-'. Only samples labelled in bold font are from this study (M3 and roche moutonnées samples); other samples are from Martin et al. (2018)

3. Methods

3.1. CRE dating methods

3.1.1. Sampling methods

Boulders were sampled using a hammer and a chisel. We favored large angular boulders to minimize the possibility of recent surface deflation of the diamict matrix. For both boulders and roches moutonnées. the thicknesses of the samples ranged between 2 and 5 cm (Tables 3–6). The tops of many boulders presented flat or slightly sloping surfaces, generally smooth and clean without any evidence of exfoliation or physical weathering. This suggests that they have experienced only negligible denudation (i.e. less than a few mm) since their deposition.

3.1.2. In-situ ^{10}Be concentration measurement

To measure cosmogenic ^{10}Be concentrations in quartz mineral fractions, samples were prepared at the CRPG (Nancy, France) to obtain pure BeO targets for subsequent ^{10}Be/^{9}Be isotopic analysis. Samples were first crushed and wet-sieved to collect the 200–800 μm fraction. Quartz grains were magnetically and electrostatically separated, then isolated through selective dissolution in a concentrated H_2SiF_6-HCl solution. Once pure quartz was obtained, 30% of the mass of each sample was dissolved during three successive HF leaching steps in order to remove any atmospheric ^{10}Be contamination from the quartz. We then added 150–300 mg of an in-house ^{9}Be carrier (2,020 ppm ^{9}Be) to the samples and completely dissolved them in concentrated HF. To isolate beryllium, samples were fractionated in three alkaline precipitations alternating with two separations on ionic-exchange columns and a final dehydration at 700 °C.

The resulting BeO was mixed with niobium powder, introduced into a copper cathode, and pressed. The ^{10}Be/^{9}Be ratios were analyzed by accelerator mass spectrometry at the French national facility ASTER (LN2C, CEREGE, Aix-en-Provence, France). During each analytical session, the measured ^{10}Be/^{9}Be ratios were normalized to the ^{10}Be/^{9}Be ratio of the NIST SRM 4325 reference material (^{10}Be/^{9}Be = (2.79 ± 0.03) × 10^{-11}; Nishiizumi et al., 2007). During the three analytical sessions,

blank values were $(2.7 \pm 1.7) \times 10^{-15}$, $(1.5 \pm 0.4) \times 10^{-15}$ and 3.9×10^{-15}, respectively, yielding respective maximum blank corrections of sample $^{10}Be/^{9}Be$ ratios of 6%, 3%, and 3%.

3.1.3. In-situ ^{3}He concentration measurements

For cosmogenic ^{3}He measurements, all samples were prepared and analyzed at the CRPG. Samples were crushed and wet-sieved to collect the 180–800 μm fraction. We concentrated heavy minerals by density separation in sodium polytungstate solutions (d~3.1 g cm^{-3}) and rinsed them with deionized water. Black and green pyroxenes were observed and identified by scanning electron microscopy, then mono-mineral grains without any adhering lava were handpicked under a binocular microscope and packed into stain capsules. The prepared pyroxene aliquots weighed between 11.4 and 57.2 mg.

The total ^{3}He concentrations of the samples were measured by split flight tube mass spectrometry following a previously established procedure (Blard et al., 2015; Mabry et al., 2012; Zimmermann et al., 2012) summarized here. Pyroxene aliquots were fused in a single vacuum resistance furnace during 15 min at 1400–1500 °C. The extracted gas was purified using activated carbons, getters, and a cryogenic pump, and ^{3}He and ^{4}He concentrations were analyzed in the spectrometer. Furnace blanks induced a mean correction of 4 ± 3% (with a maximal value of 12%). The sensitivity of the mass spectrometer was calibrated using the HESJ standard (Matsuda et al., 2002) as described in Blard et al. (2013a) over a range of helium pressures that encompassed those of the measured samples, and from which the adequate sensitivity could be interpolated. Mean 1σ external reproducibilities for ^{3}He and ^{4}He of 2.0 ± 0.6% and 1.9 ± 2.3%, respectively, with respective maximum values of 3.1% and 7.0%. During each analytical session, we measured CRONUS-P pyroxene standard aliquots, which yielded a mean concentration of $(4.92 \pm 0.16) \times 10^{9}$ at g^{-1}, in agreement with the mean reported value of $(5.02 \pm 0.06) \times 10^{9}$ at g^{-1} (Blard et al., 2015).

Blard et al. (2013a, 2014) measured magmatic ^{3}He concentrations in pyroxenes from Cerro Tunupa and Cerro Uturuncu via prolonged vacuum step-crushing. They showed that magmatic ^{3}He concentrations were 2–3 orders of magnitude below cosmogenic ^{3}He concentrations in volcanic

formations of the Altiplano. Relying on their data, we derived and applied a magmatic ^{3}He correction of 8.50×10^{4} at g^{-1} to all our samples,

Nucleogenic ^{3}He concentrations were calculated from the major and trace element compositions of both lavas and phenocrysts, as in Blard et al. (2013a) (measurements performed by SARM-CNRS). We calculated both (U-Th-Sm)/^{4}He eruption ages and nucleogenic ^{3}He production rates (following Andrews and Kay, 1982 and Andrews, 1985) to derive ^{3}He nucleogenic concentrations. For each sample, the final cosmogenic ^{3}He concentration was obtained by subtracting the magmatic and nucleogenic components from the total ^{3}He concentration. These corrections represent less than 3% of the total measured ^{3}He concentrations in all samples.

3.1.4. Cosmogenic exposure age computation

Because the cosmogenic production rate is a pivotal parameter in the calculation of exposure ages, we relied on the weighted means of local calibration values (detailed below). This approach has two advantages: (i) local calibration values limit potential inaccuracies arising from the spatial scaling procedure (Martin et al., 2015), and (ii) the use of more than one calibration study makes the final calibration value used in the age calculations more robust. The Sea Level High Latitude (SLHL) production rate used to calculate the ^{10}Be CRE ages is the weighted mean of the production rates of Blard et al. (2013a), Kelly et al. (2015), and Martin et al. (2015); these production rates were obtained in the High Tropical Andes from calibration sites within limited distances from the glacial landforms dated in the present study (all are within the Altiplano Basin, except that of Kelly et al., 2015, which is 30 km away). Similarly, ^{3}He CRE ages were calculated using the weighted mean of the production rates of Blard et al. (2013b, within the basin) and Delunel et al. (2016, 60 km away). We took the uncertainties of both production rates as the weighted standard deviations (Martin et al., 2017) taken over the individual production rate values and propagated it in the computed ages.

CRE computations were performed using the online CREp calculator (Martin et al., 2017) and the modified Lal (1991) time-dependent scaling scheme (Balco et al., 2008; Stone, 2000) with the ERA-40 spatialized atmosphere (Uppala et al., 2005) and the virtual dipolar moment (VDM) reconstruction of Muscheler et al. (2005). Borchers et al. (2016) showed that the modified Lal model and the LSD

model (Lifton et al., 2014) were the most efficient models available to reduce discrepancies between the different calibration studies at SLHL conditions. Martin et al. (2015) similarly showed that the modified Lal scheme performs better in the High Tropical Andes, especially when combined with the ERA-40 atmosphere and the VDM reconstruction of Muscheler et al. (2005).

3.1.5. Bayesian filtering of CRE ages from stratigraphic relationships

For each moraine in this study, we computed a normalized sum of the probability density function (PDF) of the age of each sample and applied a Bayesian age filtering. Stratigraphic relations between moraines and roches moutonnées bring additional time constraints to the objects that they bracket. These can be formulated in terms of Bayesian conditions (conditional probability) to produce or refine age probability densities associated with moraines (Parnell et al., 2011). We used the approach of Blard et al. (2013b) and Martin et al. (2015) on some of the studied moraines to refine their age distributions and limit the influence of possible outliers on the final results. We consider f_{Object} as the non-filtered initial PDF of the dated object (a function of time t). Stratigraphic observations enable the identification of an older and a younger object, each associated with its own PDF ($f_{\mathrm{OlderObject}}$ and $f_{\mathrm{YoungerObject}}$, respectively). A new filtered PDF f^*_{Object} can then be recalculated as:

$$f^*_{Object}(t) = f_{Object}(t) \times \int_t^{\infty} f_{OlderObject}(\tau)d\tau \times \int_0^t f_{YoungerObject}(\tau)d\tau \quad (\mathbf{1})$$

If no measurements are available for the object of interest, or if scatter is too important, a PDF can be derived for the bracketed object by replacing f_{Object} by 1.

We systematically used this approach to filter and refine the age distributions of the moraines in this study. For each moraine, a raw PDF was first established as the normalized sum of the PDF of each sample of that moraine. Then, we used Bayesian conditions based on the raw PDFs of older and younger objects to bracket the age to be refined. This was not possible for the oldest and youngest objects at a given site, which only benefited from one Bayesian condition (based on the second oldest or second youngest objects, respectively). This framework was adjusted for special cases exhibiting particularly large scatter among the individual ages associated with the central or bracketing objects.

When the age of the older/younger object was characterized by significant scatter, it was replaced by the object immediately older/younger than itself. When the central object to be refined presented scattered ages older and/or younger than those of the bracketing objects, but the bracketing PDFs were available, we replaced f_{Object} by 1. Final moraine ages were determined using the median and 1σ-range of the thusly-refined moraine PDFs. For simplicity, the uncertainty associated with each moraine age is the mean of the left and right 1σ distances to the median. Illustration of the Bayesian processing on age data is illustrated on Fig. S6 (Supplementary Information).

3.2. Equilibrium line altitude calculation methods

At the equilibrium line altitude (ELA) of a glacier, the glacier's mean annual mass balance is null. Because ELA is an integrative signal of the climatic conditions driving glacial dynamics (Ohmura et al., 1992), paleo-ELAs have been extensively used over the past 40 years for climate reconstructions (Loibl et al., 2014; Porter, 2000; Sissons and Sutherland, 1976; Stauch and Lehmkuhl, 2010). Several methods have been reported and compared to infer paleo-ELAs from the geomorphic features of glacial valleys (Benn et al., 2005; Benn and Lehmkuhl, 2000; Meierding, 1982). These methods rely on different observations, such as the glacial cirque altitude, the maximum elevation of lateral moraines, the terminus altitude, or the hypsometry of the valley, and require variable amounts of knowledge about past glacial extents. Here we used the accumulation area ratio (AAR) method, which enables ELA determination for several glacial standstills in the same valley. This method does not require any balance ratio or index, and is thus less precise than the balance ratio or area altitude balance ratio methods (Osmaston, 2005). However, because the AAR method accounts for the surfaces of the ablation and accumulation zones, it is a more explicit reference to the surface glacier mass balance than the widely used toe-to-summit and toe-to-headwall altitude ratios (Benn and Lehmkuhl, 2000; Osmaston, 2005). The AAR method has been applied to derive accurate ELA values in various mountain glacier settings (e.g. Martin et al., 2018).

ELA determinations using the AAR method rely on the use of an appropriate AAR parameter, which ranges between 0.5 and 0.8 for present glaciers around the world (see Benn and Lehmkuhl, 2000, and Benn et al., 2005, for reviews). Here, we used AAR values based on mass balance measurements

conducted on three Andean glaciers by the GLACIOCLIM-IRD National Observation Service (Rabatel et al., 2013; Soruco et al., 2009). Observed present-day AAR values were regressed against annual mass balance measurements to account for the non-equilibrium conditions that characterize most glaciological years over the last three decades in the Andes. We established AAR values for this study as the *y*-intercepts of these regressions (i.e. the AAR for a null mass balance, see supplementary material of Martin et al., 2018, for details). Thus, we used an AAR range of 0.63–0.73 (average 0.68), consistent with Martin et al. (2018), to account for uncertainties (see review of AAR variability in Benn and Lehmkuhl, 2000). Required hypsometry data were derived from the NASA-USGS SRTM 1-arcsecond global digital elevation model (DEM).

3.3. Climatic inversion methods

3.3.1. Glacial extent and climatic conditions

Climate controls glacial dynamics through accumulation (snowfall) and ablation (mainly melting and sublimation). Glaciers, and, more precisely, the past glacial extent indicated by moraine records, have thus been used as proxies of past climatic changes. Sagredo and Lowell (2012) proposed a complete climatic setting for Andean glaciers. They proposed classifying glaciers into different groups characterized by common climate settings. The glacial records presented in this study span two groups, the Cordillera Real and the southeast Altiplano, both characterized by cold and homogenous temperatures throughout the year and low precipitation inputs during the Austral summer (see Section 1). The main difference between these two groups is annual rainfall, with the Cordillera Real receiving more precipitation than the southeast Altiplano (700 vs. 300 mm yr^{-1}). In the southern Altiplano, although their summits stand above the 0 °C isotherm during the ablation season, volcanoes such as Cerro Tunupa (5,321 m asl) and Cerro Luxar (5,396 m asl) do not presently have permanent ice cover due to the low annual precipitation. This primary dependence of glacial dynamics on precipitation makes the region *precipitation-limited* (Ammann et al., 2001; Kull et al., 2008).

Considering the characteristic response time of several decades for mountain glaciers (Leclercq et al., 2014), we consider them to be in equilibrium with climatic conditions for our reconstructions. Therefore, we followed Martin et al. (2018, methodological comparison and discussion provided in their

Supplementary Information) and used empirical relations between ELA and the present climate derived from statistical analyses of modern glaciers. These relations consider that the ELA position depends primarily on mean temperature and precipitation values; enhanced accumulation concomitant with lowering of the ELA is associated with decreased temperature and/or increased precipitation, whereas the opposite trend is associated with raising of the ELA (Condom et al., 2007; Kuhn, 1989; Ohmura et al., 1992; Seltzer, 1994). For the Central Andes, Condom et al. (2007) extended the work of Fox (1993) to derive ELA (m asl) as:

$$ELA = 3427 - 1148 \times log_{10}(P) + \frac{T(z)}{LR} + z \quad (\mathbf{2})$$

where P is the annual rainfall (mm), T is mean annual temperature (°C), LR is the atmospheric lapse rate (°C m^{-1}), and z is the altitude of the temperature measurement (m asl). As in Martin et al. (2018), we chose this modeling approach for several reasons: (i) Equation (2) directly links ELA to the investigated climatic variables; (ii) it is easy to use in terms of data availability, calculation, and error propagation; (iii) contrary to energy balance models, it requires limited atmospheric variables; and (iv) it performs well for Bolivian glaciers (see Fig. S13 in Martin et al., 2018).

3.3.2. Present-day temperature and precipitation at the glacial sites

To document paleoclimatic variations, we consider the present as a reference state. We used homogenized monthly weather station data (Vuille et al., 2008; Martin et al., 2018) to establish the reference climatic conditions at the four studied paleoglacial sites (Table 1). This record includes 57 temperature stations and 102 precipitation stations spanning 14–23°S (including the cordilleras and the Altiplano) over the observational periods 1948–2001 (precipitation) and 1948–2007 (temperature). The derived mean temperature and annual precipitation values for the four paleoglacial sites studied herein are reported in Table 1.

Sites	Zongo	Sajama	Tunupa	Luxar
Latitude (°S)	16.2	18.1	19.8	21.0
Longitude (°W)	68.1	68.9	67.6	68.0
Summit elevation (masl)	6088	6542	5321	5440
Mean annual Rainfall (mm)	529 ± 9	329 ± 7	201 ± 15	136 ± 16
Mean annual temperature normalized to 3800 masl[a] (°C)	8.5 ± 0.2	7.7 ± 0.6	6.3 ± 0.2	7.5 ± 0.7

[a] Normalization calculated for a lapse rate of 6.5°C/km

Table 1. Present annual rainfall and mean temperature at the studied sites derived from weather station measurements (Vuille et al., 2008; Martin et al., 2018). Observation from 1948 to 2001 for precipitation and 1948 to 2007 for temperature. Temperatures normalized at 3800 masl for comparison purpose.

Equation (2) implies that a given ELA could correspond to several local precipitation-temperature pairs. Therefore, additional constraints are required to derive unique precipitation and temperature pairs for each ELA. To do so, we couple glacier and lake modeling following Blard et al. (2009), Placzek et al. (2013) and Martin et al. (2018), but we extend their approach to the entire deglaciation, between 18 and 10 ka BP.

3.3.3. Lake model

We used the lake model of Condom et al. (2004) as modified by Martin et al. (2018). This model divides the Altiplano Basin into lake and soil pixels. All soil pixels are considered to be a reservoir that can be filled until its overflow threshold (*CapaS*) is reached. When precipitation fills the reservoir above *CapaS*, water flows directly to the lake. The flow path of water from the watershed pixel to the lake is not taken into account. As in Blard et al. (2009), the equation used to calculate evaporation is derived from the generalized equation of Xu and Singh (2000) that relies on a simplified energy balance budget. The model is run at a quarterly time resolution and a 5-km spatial resolution. Because gridded products are necessary for the lake model, the temperature and precipitation inputs are derived from the dataset of New et al. (2002). Elevation is based on the 1-arcsecond SRTM DEM. The *CapaS* value was calibrated from the Titicaca watershed for the present period. The modifications of Martin et al. (2018) to the original model of Condom et al. (2004) account for the potential yearly accumulation of seasonal snow stock on watershed pixels. The distributed model computes the melting of this stock using a

positive degree day (PDD) value of 6 mm $°C^{-1}$ d^{-1}. Melted snow first fills the soil reservoir until reaching *CapaS* and overflowing. Further details are available in the Supplementary Information of Martin et al. (2018).

3.3.4. Coupled lake and glacier modeling

The complete inversion workflow is presented in Fig. 9 and operates as follows. For a given late-glacial moraine of a paleoglacier, we have access to its age via CRE dating and its ELA via the AAR method. From this ELA, the relation of Condom et al. (2007) provides a set of local *P*-*T* solutions that respect the glacial extent (green path in Fig. 9). From the moraine age, the algorithm considers the synchronous lake shoreline in the updated dataset of the lake level chronology (see Section 4.1.1). The paleolake extent corresponding to the selected level is then used to compute the correct hydrologic balance for different cooling and precipitation values (blue path in Fig. 9). The precipitation field used in the model includes a local anomaly of enhanced rainfall over the lake region (see Section 3.3.5 and Supplementary Information). The intersection of these two computed *P*-*T* curves (sets of solutions) then defines the precise climatic conditions (i.e. a single *P*-*T* pair) associated with the glacial extent. We note that, despite major lake-size variations, both the continuous sediment accumulation in the Coipasa Basin throughout the study period (Nunnery et al., 2019) and the presence of shoreline records indicate that the lake did not completely dry prior to the Holocene; this algorithm is therefore applicable to the entire last deglaciation.

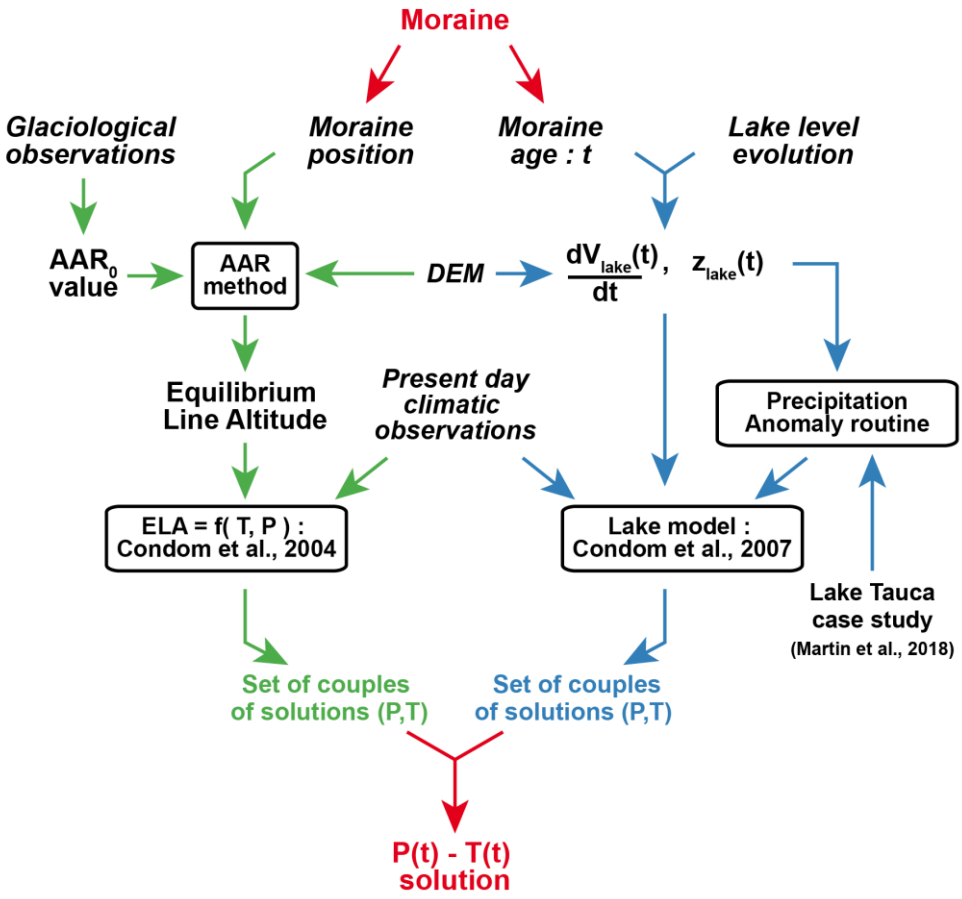

Figure 9. Workflow for paleoclimatic inversions in this study. Lake level evolutions are based on Sylvestre et al. (1999), Placzek et al. (2006), and Blard et al. (2011a), and include the updated Coipasa highstand of the present study (see Section 2.2 and 4.1.1). Glaciological observations are from Soruco et al. (2009) and Rabatel et al. (2013). Moraine ages are either original ages from this study or ages from the literature (see Section 2.3). Present day climatic observations are from New et al. (2002) for gridded products (lake model inputs) and station data (Vuille et al., 2008) for site-specific data (ELA(P,T) inputs). We used the NASA-USGS SRTM 1-arcsecond DEM. Details on the Precipitation Anomaly routine are provided in Section 3.3.5. Input data are italicized.

3.3.5. Spatial variability of precipitation induced by precipitation recycling

Martin et al. (2018) recently established the spatial distribution of precipitation during the Tauca Highstand, which evidences the local recycling of lake water superimposed on the global rainfall field. Here, we develop a novel algorithm to account for this lake-induced local precipitation anomaly. In practice, this routine uses the case study of Martin et al. (2018) to mimic the Lake Tauca rainfall anomaly for any given lake geometry and extent. This routine is necessary because they showed this recycling effect to have a non-negligible impact on the spatial distribution of rainfall. Moreover, the four studied glacial sites are contrastingly impacted by this regional precipitation anomaly: whereas Zongo Valley is far from any paleolake influence, the Tunupa and Luxar glaciers, being close to the paleolake centers, were highly impacted by this recycling. To define the geometry of this regional rainfall recycling, we chose an empirical approach that aims to adapt the radial evolution of the Tauca anomaly for any lake configuration of the last deglaciation. In this simplified framework, we define the paleoprecipitation grid as:

$$P(x,y,t) = P_{Present}(x,y) \times \alpha(t) \times \left\{1 + \beta\big(lake(t)\big) \times A\big(x,y,lake(t)\big)\right\} \quad (\mathbf{3})$$

where P is the precipitation field over the basin (two spatial dimensions x and y) at a given time t of the last deglaciation, P_{Present} is the present day precipitation field over the basin, α is a scalar regional amplification factor, β is the amplitude of the recycling anomaly based on the lake surface, and A is the normalized anomaly grid. β is empirically calibrated using hydrological data from several intertropical lakes (Lakes Mweru, Malawi, Titicaca, and Victoria; see Supplementary Information S4). We obtained a relation fitting β to the lake surface (S_{lake}, km^2) with a coefficient of determination (R^2) of 0.97.

$$\beta = 0.27 \times ln(S_{lake}) - 2.10 \quad (\mathbf{4})$$

We then used the Tauca highstand case study of Martin et al. (2018) to establish the matrix $A(x, y, t = \text{Tauca highstand}) = A_{\text{Tauca}}$ and thus isolate the recycling anomaly. To do so, we inverted Equation (3) for t = Tauca highstand. The value of α_{Tauca} was taken as 2.4, the mean $P_{\text{Tauca}}/P_{\text{Present}}$ ratio for Zongo Valley and Nevado Sajama, which corresponds to the increased precipitation far from the Tauca paleolake influence. Then, β_{Tauca} was computed using Equation (4).

564 To adapt the shape of the recycling anomaly to the different lacustrine configurations of the last
565 deglaciation, we first approached the Tauca anomaly as follows. We first computed the barycenter of
566 Lake Tauca, which we defined as the point of the lake surface for which the sum of the distances to all
567 other points on the lake surface is minimal. From this barycenter, we discretized the Altiplano Basin
568 into 20 regular angular sectors ("pie slices"). The mean radius of the lake for a given sector was
569 computed considering the mean distance from the barycenter to all Lake Tauca points within that sector.
570 Then, the radially decreasing anomaly profile (from the barycenter towards the watershed edges) was
571 averaged per sector and normalized by the mean lake radius of each sector.

572 For the different lake configurations during deglaciation, we then assumed that the recycling
573 anomaly can be deduced from the Tauca anomaly by some kind of homothety (a transformation
574 preserving angles and length ratios) centered on the paleo-barycenter of the lake. We therefore implicitly
575 assume that the redistribution of the local lake-evaporation moisture is primarily driven by the
576 geographic extent of the water body, and that the wind regime has not drastically changed. For each
577 paleo-lake extension, we then calculated its barycenter, the angular sectors, and the mean lake radius
578 per sector, and applied the normalized radial profile (defined by the Lake Tauca extent) to derive $A(x,$
579 $y, t)$.

580 Once $A(x, y, t)$ was established, $\beta(t)$ was calculated using Equation (4) and $\alpha(t)$ was numerically
581 adjusted so that the climatic input to the lake model is in accordance with the prescribed lake budget
582 (Fig. 9). The reconstructed anomaly fields (given as $\beta \times A$) for the Lake Coipasa and Lake Tauca
583 highstands are shown in Figure 10. Further details of the anomaly algorithm are provided in the
584 Supplementary Information (and graphically illustrated in Fig. S3). The resulting precipitation field is
585 in excellent agreement with the ELA-derived precipitation map of Martin et al. (2018; see their Fig.
586 3D).

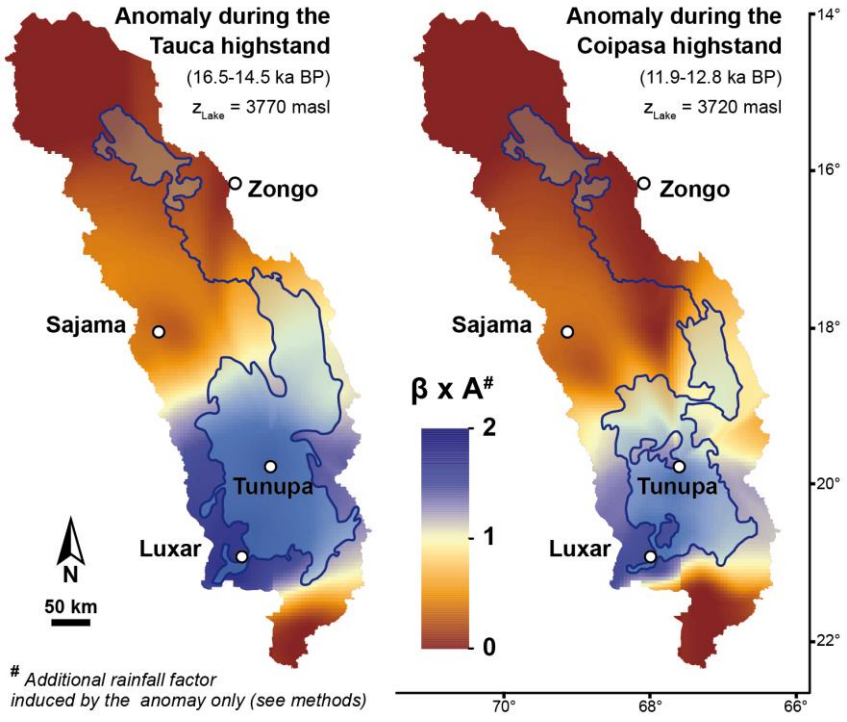

587

588 *Figure 10. Reconstructed precipitation anomaly fields of the Tauca and Coipasa highstands using the*
589 *anomaly algorithm (see Section 3.3.5 and Supp. Info. S2) compared to the present. Reported values are*
590 *the product $\beta \times A$.*
591

4. Results

4.1. Dating results

4.1.1. New shoreline ^{14}C ages from Incahuasi Island

Our new ^{14}C ages (Table 2) and all previously published radiocarbon ages were calibrated relative to 2010 using OxCal 4.2 (Ramsey, 2009) and the IntCal13 calibration curve (Reimer, 2013). This updated dataset was used to refine our knowledge of the evolution of the lake level through time (Fig. 11). Our four new calibrated ages span the Tauca and Coipasa lake cycles, with sample INC-13-2 (15.97 ± 0.11 cal kyr BP) belonging to the transgressive or deep part of the Lake Tauca cycle. Both replicates of INC-13-3 (INC-13-3A and INC-13-3B) yield ages of 12.75 ± 0.03 and 12.09 ± 0.13 cal kyr BP, respectively, precisely coeval with the Lake Coipasa highstand. However, sample INC-13-1 does not fit the lake level curve established by Blard et al. (2011a); its age of 13.44 ± 0.05 cal kyr BP is 1 kyr too young to belong to the Tauca highstand and 1 kyr too old for the Coipasa highstand. This single sample is at odds with the complete dataset, which supports the near-complete evaporation of the lake between 14 and 13 ka BP (see summary in Blard et al., 2011a). Thus, we consider sample INC-13-1 to be partially contaminated by modern or dead carbon and exclude it from further discussion.

Sample	Material	Latitude *Dec°*	Longitude *Dec°*	Elevation *masl*	Mass *mg*	$\delta^{13}C$ *‰ vs PDB*	Modern C *%*	^{14}C age[a] *yr*	Calendar age (1σ)[b] *ka BP*
INC-13-1	Bioherm, white massive algal carbonate (external part)	-20.2435	-67.6255	**3715**	0.35	2.28	23.8 ± 0.2	11550 ± 50	**13.44 ± 0.05**
INC-13-2	Bioherm, cream-coloured carbonate (internal part)				0.37	1.53	19.2 ± 0.2	13240 ± 60	**15.97 ± 0.11**
INC-13-3-A	Bioherm, white massive algal carbonate	-20.2432	-67.6254	**3720**	0.62	2.65	26.2 ± 0.1	10745 ± 45	**12.75 ± 0.03**
INC-13-3-B					0.69	3.49	27.9 ± 0.2	10270 ± 45	**12.09 ± 0.10**

[a] Uncalibrated ages

[b] Present refers to 2010. Calibration performed with IntCal13, OxCal 4.2 (Ramsey, 2009; Reimer, 2013)

Table 2. Radiocarbon results for lacustrine bioherms of Incahuasi Island.

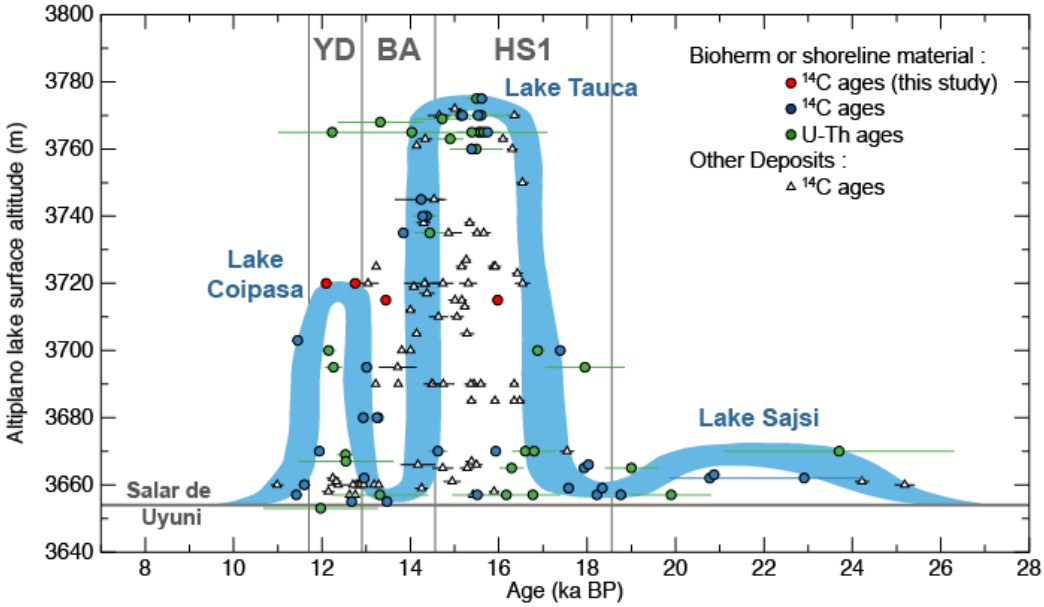

Figure 11. Paleolake chronology of the southern Altiplano. The blue curve is updated from Blard et al., (2011a) to fit a Lake Coipasa highstand 15-20 m above their values, as indicated by our new data (red points). Other data (blue, green, and white points) are from Blard et al. (2011a), Placzek et al. (2006), and Sylvestre et al. (1999).

The most important update from this new dataset is that the two ^{14}C ages of bioherms INC-13-3A and B belong to the Lake Coipasa (Younger Dryas) event (Fig. 11). These samples stand at 3,720 m asl, indicating that the Coipasa highstand was probably 15–20 m higher than previously reported (Blard et al., 2011a; Placzek et al., 2006) (Table 2; Fig. 11). This additional lake volume will induce a different hydrological balance for Lake Coipasa compared with previous studies.

4.1.2. ^{10}Be moraine chronology of Zongo Valley

The CRE age results from Zongo Valley are presented in Table 3 and Figure 12. Moraines IP1 and IP2 (from Smith et al., 2005) exhibit extreme scatter; although it is hard to identify their precise timing in the late-glacial period, their position in the valley necessitates that they are older than the other moraines. Therefore, they are probably older than IP3 and have an age of at least 17 ka BP. The three IP3 ages of Martin et al. (2018) are consistent with the four from Smith et al. (2005). By imposing the Bayesian condition that IP4 is a younger object, the age distribution of IP3 is narrowed by a few centuries towards older ages, yielding a final age of 16.9 ± 0.8 ka BP. Sample MB4 from moraine IP4 has an age two times older than those of two other samples from the same moraine that cluster well

(36.9 ka BP compared to 16.6 ka BP). This outlier was filtered out by our Bayesian processing when using IP3 as an older object, giving a final age of 16.0 ± 0.8 ka BP for moraine IP4. The exposure ages of samples from moraines IP5, CQ1, CQ3, and CQ4 cluster well and form a unique age peak in the PDF. Our Bayesian processing has only a marginal effect on these ages, which yield respective average values of 13.6 ± 0.8, 11.6 ± 0.5, 10.7 ± 0.4, and 10.1 ± 0.4 ka BP. Due to its upper position and its being disconnected from the other glacier systems, we could not refine the ages for moraine IPα via Bayesian filtering and its age PDF is bimodal; the main peak yields an age of 14.9 ± 0.9 ka BP.

With CRE ages ranging from 9 to 21 ka BP, moraine MV exhibits substantial scatter. However, imposing the Bayesian conditions that IP5 and CQ1 are older and younger than MV, respectively, narrows its age distribution to 12.6 ± 0.8 ka BP. Bayesian filtering also substantially modifies the PDF of moraine T1, yielding an age of 12.4 ± 1.5 ka BP. Bayesian modifications are more marginal for T2 and T3, yielding respective ages of 11.0 ± 0.8 and 9.8 ± 0.9 ka BP.

Moraine	Source	Sample	Latitude	Longitude	Altitude	^{10}Be (1σ)	Thickness	Thick. Corr.[a]	Shielding[b]	Scaling Factor[c]	Age (1σ)[d]
			Dec°	*Dec°*	*masl*	*10^5 at.g^{-1}*	*cm*	-	-	-	*ka*
		ZONG-03-06	-16.1310	-68.1697	3417	3.57 ± 0.14	1	0.99	0.87	6.1	**16.8 ± 0.7**
		ZONG-03-07	-16.1314	-68.1697	3408	3.47 ± 0.15	4	0.97	0.89	6.0	**16.5 ± 0.7**
		ZONG-03-08	-16.1310	-68.1693	3399	1.15 ± 0.05	3	0.98	0.85	5.4	**6.3 ± 0.3**
IP1	Smith et al., 2005	ZONG-03-09	-16.1310	-68.1693	3393	3.33 ± 0.09	3	0.98	0.89	6.0	**15.9 ± 0.5**
		ZONG-03-10	-16.1309	-68.1692	3391	1.31 ± 0.05	3	0.98	0.89	5.5	**6.8 ± 0.3**
		ZONG-03-11	-16.1310	-68.1691	3383	0.69 ± 0.04	3	0.98	0.89	5.2	**3.8 ± 0.3**
		ZONG-03-12	-16.1309	-68.1692	3386	2.51 ± 0.07	2	0.98	0.89	5.8	**12.2 ± 0.5**
		ZONG-03-01	-16.1366	-68.1755	3489	4.73 ± 0.24	1	0.99	0.95	6.5	**19.2 ± 0.9**
		ZONG-03-02	-16.1366	-68.1755	3500	4.15 ± 0.12	3	0.98	0.95	6.4	**17.4 ± 0.6**
IP2	Smith et al., 2005	ZONG-03-03	-16.1367	-68.1757	3503	3.27 ± 0.12	2	0.98	0.95	6.2	**14.0 ± 0.6**
		ZONG-03-04	-16.1367	-68.1757	3503	1.97 ± 0.09	1	0.99	0.95	6.0	**8.7 ± 0.4**
		ZONG-03-05	-16.1368	-68.1757	3505	3.54 ± 0.14	1	0.99	0.95	6.2	**14.9 ± 0.6**
		MB6	-16.1915	-68.1330	3870	5.02 ± 0.19	1	0.99	0.97	7.7	**16.8 ± 0.7**
	Martin et al., 2018	MB7	-16.1918	-68.1326	3886	5.02 ± 0.16	1	0.99	0.97	7.7	**16.7 ± 0.6**
		MB8	-16.1918	-68.1325	3887	4.69 ± 0.25	3	0.98	0.97	7.7	**15.9 ± 0.8**
IP3		ZONG-00-06	-16.1333	-68.1919	3895	4.76 ± 0.21	5	0.96	0.98	7.7	**16.2 ± 0.7**
	Smith et al., 2005	ZONG-00-07	-16.1333	-68.1919	3895	5.14 ± 0.21	5	0.96	0.95	7.8	**17.7 ± 0.7**
		ZONG-00-08	-16.1333	-68.1919	3895	4.71 ± 0.16	5	0.96	0.98	7.7	**16.0 ± 0.6**
		ZONG-00-09	-16.1333	-68.1919	3895	4.30 ± 0.15	5	0.96	0.98	7.6	**14.9 ± 0.5**
		MB1	-16.1932	-68.1328	3768	4.65 ± 0.42	2	0.98	0.97	7.3	**16.6 ± 1.3**
IP4	Martin et al., 2018	MB2	-16.1933	-68.1320	3784	4.66 ± 0.22	2	0.98	0.96	7.3	**16.6 ± 0.8**
		MB4	-16.1933	-68.1317	3790	11.05 ± 0.92	0.5	1.00	0.96	7.7	**36.9 ± 2.8**
		ZONG-00-01	-16.1308	-68.1962	3806	3.56 ± 0.18	5	0.96	0.95	7.2	**13.5 ± 0.7**
		ZONG-00-02	-16.1308	-68.1962	3806	3.75 ± 0.22	5	0.96	0.95	7.2	**14.1 ± 0.8**
IP5	Smith et al., 2005	ZONG-00-03	-16.1308	-68.1962	3806	3.33 ± 0.23	5	0.96	0.95	7.2	**12.6 ± 0.9**
		ZONG-00-04	-16.1308	-68.1962	3806	3.57 ± 0.16	5	0.96	0.95	7.2	**13.5 ± 0.7**
		ZONG-00-05	-16.1308	-68.1962	3806	3.71 ± 0.14	5	0.96	0.95	7.2	**14.0 ± 0.6**
		MB9	-16.2321	-68.1179	4255	5.38 ± 0.29	3	0.98	0.97	9.1	**15.5 ± 0.8**
		MB10	-16.2322	-68.1178	4256	5.16 ± 0.16	3	0.98	0.97	9.0	**15.0 ± 0.5**
		MB11	-16.2329	-68.1177	4264	4.38 ± 0.16	1	0.99	0.97	8.9	**12.6 ± 0.6**
		MB12	-16.2330	-68.1177	4265	7.82 ± 0.38	2	0.98	0.97	9.6	**21.0 ± 1.0**
MV	**This Study**	MB13	-16.2330	-68.1177	4265	3.79 ± 0.24	2	0.98	0.97	8.8	**11.1 ± 0.7**
		MB14	-16.2330	-68.1177	4265	5.16 ± 0.26	3	0.98	0.97	9.0	**14.8 ± 0.7**
		Zong-13-01	-16.2302	-68.1199	4183	2.97 ± 0.11	2	0.99	0.97	8.3	**9.1 ± 0.4**
		Zong-13-02	-16.2301	-68.1201	4177	2.90 ± 0.11	2	0.99	0.97	8.3	**9.0 ± 0.4**
		Zong-13-03	-16.2281	-68.1225	4180	2.08 ± 0.10	0.5	1.00	0.97	8.0	**6.6 ± 0.3**
		Zong-13-04	-16.2300	-68.1200	4191	3.43 ± 0.15	1	0.99	0.97	8.4	**10.4 ± 0.5**
		ZONG-00-10	-16.1301	-68.1902	4105	5.28 ± 0.21	5	0.96	0.99	8.5	**16.1 ± 0.6**
IP alpha	Smith et al., 2005	ZONG-00-11	-16.1301	-68.1902	4105	4.66 ± 0.22	5	0.96	0.99	8.3	**14.5 ± 0.6**
		ZONG-00-12	-16.1301	-68.1902	4105	4.72 ± 0.16	5	0.96	0.99	8.3	**14.7 ± 0.5**
		CNB1	-16.2751	-68.1158	4630	4.99 ± 0.31	2	0.99	0.99	10.5	**12.0 ± 0.8**
		CNB2	-16.2751	-68.1158	4631	4.74 ± 0.16	3	0.98	0.99	10.5	**11.6 ± 0.4**
CQ1	**This Study**	CNB3	-16.2750	-68.1160	4630	4.85 ± 0.16	2	0.98	0.99	10.5	**11.7 ± 0.4**
		CNB4	-16.2750	-68.1162	4628	4.56 ± 0.19	3	0.98	0.99	10.4	**11.2 ± 0.5**
		CNB5	-16.2750	-68.1159	4629	4.76 ± 0.19	2	0.98	0.99	10.5	**11.6 ± 0.5**
		CNB16	-16.2749	-68.1192	4486	3.77 ± 0.13	1	0.99	0.97	9.6	**10.0 ± 0.4**
		CNB17	-16.2748	-68.1193	4488	4.15 ± 0.15	1	0.99	0.97	9.7	**10.9 ± 0.4**
CQ3	**This Study**	CNB18	-16.2748	-68.1191	4493	4.03 ± 0.13	1	0.99	0.97	9.7	**10.6 ± 0.4**
		CNB19	-16.2748	-68.1190	4492	4.11 ± 0.25	1	0.99	0.97	9.7	**10.8 ± 0.6**
		CNB20	-16.2748	-68.1192	4489	3.71 ± 0.14	2	0.99	0.98	9.6	**9.8 ± 0.4**
		CNB11	-16.2814	-68.1148	4585	3.94 ± 0.13	2	0.98	0.95	10.1	**10.2 ± 0.4**
CQ4	Jomelli et al., in prep.	CNB13	-16.2748	-68.1190	4492	3.96 ± 0.17	3	0.98	0.97	9.7	**10.6 ± 0.5**
		CNB15	-16.2814	-68.1144	4594	3.88 ± 0.13	2	0.98	0.96	10.1	**10.0 ± 0.4**

[a] Calculated with a density of 2.7 g.cm^{-3} and an attenuation length of 160 g.cm^{-2}

[b] Calculated using the CRONUS shielding application

[c] Global scaling factor that accounts for the geomagnetic correction

[d] PR: weighted mean of Kelly et al. (2013), Blard et al. (2013b) and Martin et al. (2015) - Scaling: Lal modified - Atmosphere: ERA40 - VDM: Muscheler et al. (2005)

Table 3. Zongo Valley ^{10}Be CRE age results. Recalculated ages from Cerro Telata (Jomelli et al., 2011) are presented in the Supplementary Information (Table S1a) as well as the raw ^{10}Be and ^{9}Be measurements of the new samples (Table S1b).

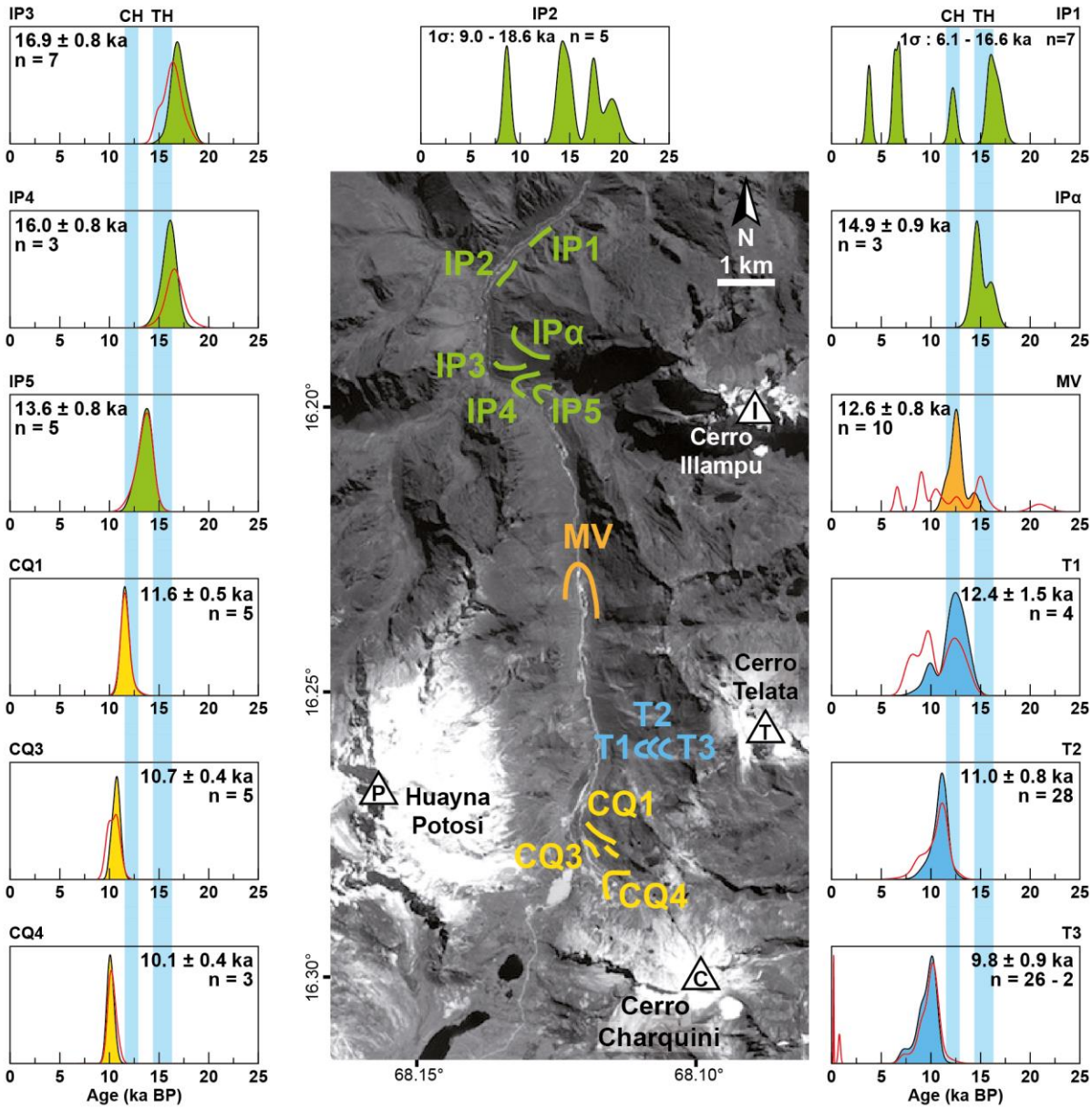

Figure 12. Moraine ^{10}Be CRE ages in Zongo Valley. The age PDFs of each moraine are color coded to the map colors. For each PDF, the median age and mean 1σ range are indicated. Boulder ages contributing to the moraine PDFs beyond 25 ka BP are not represented. Red curves are the raw PDFs before Bayesian processing, and the shaded histograms are the final PDFs from which ages were derived (see Section 3.1.5). For moraines IP1 and IP2, the scatter is too important to propose a relevant central value, and only the central 1σ range is indicated. 'n' indicates the number of samples. When n is reported as 'n = A – B', A is the total number of boulders dated on the moraine and B is the number of boulders considered to be outliers. The blue bars labeled 'TH' and 'CH' indicate the Tauca and Coipasa highstands, respectively.

4.1.3. ^{3}He moraine chronology of Nevado Sajama

CRE age results for Nevado Sajama are presented in Table 4 and Figure 13. Ages of moraine M0 show important scatter; imposing the Bayesian condition that M1 is younger does not substantially narrow the age distribution, which finally yields an age of 16.1 ± 1.5 ka BP. The M1 age PDF comprises a main peak at c. 15 ka BP, corresponding to four statistically consistent boulder ages, and two minor peaks corresponding to two older single-boulder ages at 19 and 29 ka BP. We attributed these two older ages to the production of ^{3}He in these blocks prior to their deposition atop the moraine (i.e. inheritance) and thus consider them to be outliers. After Bayesian processing using M0 and M2 as respectively older and younger objects, the age PDF computed from the four main-peak samples gives an age of 15.3 ± 0.7 ka BP. The raw age distribution of M2 presents important scatter; imposing the Bayesian conditions that M1 and M3 are respectively older and younger narrows its age range to 15.1 ± 0.8 ka BP.

The four boulders of M3 yielded clustered ages, with the Bayesian processing only marginally refining the PDF to yield an age of 14.9 ± 0.8 ka BP. The M4 age is based on a single boulder (SAJ-8) whose age of 11.8 ± 0.7 ka BP is coherent with the ages of the younger SAJ-7 roche moutonnée (10.8 ± 0.5 ka BP) and the older M3 moraine. The ages of the SAJPH-8 roches moutonnées (15.1 ± 0.7 ka BP) is in good agreement with the moraine ages, whereas SAJPH-7 yields an age that is several thousand years younger than the well-established age of M3. Therefore, SAJPH-7 is probably at odds with the global chronology and must have been affected by shielding, either by remnants of basal till or by hillslope colluvium.

Glacial Feature	Source	Sample	Latitude	Longitude	Altitude	Pyroxene Color	Li	Eruption age[a]	Pn	^3He_n	^3He_c (1σ)[b]	Thickness	Thick. Corr.[c]	Shielding[d]	Scaling Factor[e]	Age (1σ)[f]
			Dec°	*Dec°*	*masl*		*ppm*	*Ma*	*at.g^{-1}.yr^{-1}*	*10^5 at.g^{-1}*	*10^7 at.g^{-1}*	*cm*	-	-	-	*ka*
		SAJ 1	-18.1817	-68.8494	4400	Black	68	4.9	0.17	8.55	**2.06 ± 0.09**	2.0	0.98	1.00	10.03	**15.7 ± 0.7**
		SAJ 2	-18.1813	-68.8496	4407	Black	21	3.5	0.06	2.04	**1.90 ± 0.14**	1.0	0.99	1.00	9.90	**14.6 ± 1.0**
M0	**This study**	SAJ PH 1	-18.1823	-68.8451	4422	Black	15	3.5	0.05	1.77	**1.77 ± 0.20**	1.0	0.99	1.00	9.87	**13.6 ± 1.5**
		SAJ PH 2	-18.1820	-68.8452	4436	Black	28	3.8	0.10	3.69	**1.83 ± 0.09**	1.5	0.99	1.00	9.95	**14.0 ± 0.8**
		SAJ PH 3	-18.1779	-68.8458	4498	Black	51	4.4	0.17	7.37	**2.47 ± 0.12**	2.0	0.98	1.00	10.71	**17.6 ± 0.9**
		SAJ 3	-18.1761	-68.8505	4532	Black	67	0.2	2.10	4.16	**2.14 ± 0.11**	1.5	0.99	1.00	10.61	**15.4 ± 0.8**
		SAJ 3 -R	-18.1761	-68.8505	4532	Green	47	0.2	1.48	3.22	**2.15 ± 0.14**	1.5	0.99	1.00	10.62	**15.4 ± 0.9**
		SAJ 4	-18.1761	-68.8505	4532	Black	54	0.2	0.82	1.78	**1.86 ± 0.09**	2.0	0.98	1.00	10.37	**13.7 ± 0.8**
M1	Martin et al., 2018	SAJ 5	-18.1734	-68.8510	4570	Black	115	0.3	1.88	5.37	**2.26 ± 0.11**	1.0	0.99	1.00	10.86	**15.8 ± 0.8**
		SAJ 6	-18.1717	-68.8516	4580	Black	53	0.3	0.90	2.31	**2.13 ± 0.10**	3.0	0.97	1.00	10.81	**15.2 ± 0.7**
		SAJ PH 4	-18.1755	-68.8456	4527	Black	43	4.1	0.14	5.58	**4.42 ± 0.18**	1.0	0.99	1.00	11.44	**29.2 ± 1.6**
		SAJ PH 5	-18.1771	-68.8464	4480	Black	148	2.9	0.46	13.19	**2.75 ± 0.12**	2.0	0.98	1.00	10.83	**19.4 ± 0.9**
		SAJ PH 9	-18.1632	-68.8474	4584	Black	52	5.6	0.17	9.72	**3.90 ± 0.14**	0.5	1.00	0.99	11.48	**25.6 ± 1.1**
		SAJ PH 10	-18.1632	-68.8474	4584	Black	89	0.6	0.20	1.15	**3.44 ± 0.17**	1.0	0.99	0.99	11.61	**22.4 ± 1.4**
M2	**This study**	SAJ PH 11	-18.1632	-68.8477	4578	Black	43	4.6	0.15	6.91	**2.02 ± 0.07**	0.5	1.00	0.99	10.65	**14.3 ± 0.6**
		SAJ PH 12	-18.1637	-68.8476	4569	Black	99	5.5	0.32	17.50	**2.23 ± 0.10**	3.0	0.97	0.99	10.85	**15.8 ± 0.7**
		SAJ PH 13	-18.1643	-68.8478	4565	Black	27	3.8	0.08	2.88	**2.56 ± 0.12**	1.5	0.99	0.99	11.03	**17.6 ± 0.8**
Roches Moutonnées	**This study**	SAJ PH 8	-18.1617	-68.8510	4545	Black	65	7.6	0.20	15.54	**2.10 ± 0.10**	2.0	0.98	0.99	10.63	**15.1 ± 0.7**
		SAJ PH 7	-18.1565	-68.8514	4593	Black	33	7.2	0.09	6.48	**1.61 ± 0.09**	3.0	0.97	0.99	10.61	**11.7 ± 0.7**
		SAJ 9	-18.1518	-68.8553	4662	Black	126	0.2	2.05	3.94	**2.24 ± 0.12**	1.5	0.99	1.00	11.21	**15.2 ± 0.8**
		SAJ 10	-18.1518	-68.8550	4660	Black	68	0.4	1.88	8.27	**2.27 ± 0.14**	1.0	0.99	1.00	11.22	**15.4 ± 0.9**
M3	**This study**	SAJ 10 -R	-18.1518	-68.8550	4660	Green	24	0.5	0.66	3.45	**2.15 ± 0.12**	1.0	0.99	1.00	11.10	**14.7 ± 0.8**
		SAJ 11	-18.1532	-68.8534	4640	Black	36	0.4	0.19	0.82	**2.25 ± 0.15**	1.5	0.99	1.00	11.12	**15.4 ± 0.9**
		SAJ 11 - R	-18.1532	-68.8534	4640	Green	8	0.5	0.04	0.21	**2.26 ± 0.15**	1.5	0.99	1.00	11.14	**15.4 ± 1.0**
		SAJ PH 6	-18.1555	-68.8516	4604	Black & Green	22	0.4	0.13	0.56	**2.06 ± 0.10**	0.5	1.00	0.99	10.78	**14.4 ± 0.7**
M4	**This study**	SAJ 8	-18.1485	-68.8552	4670	Black & Green	25	0.2	0.31	0.71	**1.70 ± 0.09**	1.5	0.99	1.00	10.98	**11.8 ± 0.7**
R. Mout.	**This study**	SAJ 7	-18.1413	-68.8535	4706	Black	16	5.1	0.07	3.65	**1.57 ± 0.06**	1.0	0.99	0.99	11.01	**10.8 ± 0.5**

R replicate. For the sample from this study, replicates have been used to compare ^3He concentrations from black and green pyroxenes

[a] (U-Th-Sm)/^4He age

[b] $He_c = He_{tot} - He_n - He_m$ (we considered $He_m = 8.5 \times 10^4$ at.g^{-1} for all samples)

[c] Calculated with a density of 2.7 g.cm^{-3} and an attenuation length of 160 g.cm^{-2}

[d] Shielding is negligible

[e] Global scaling factor that accounts for the geomagnetic correction

[f] SLHL PR: weighted mean of the rates from Blard et al. (2013a) and Delunel et al. (2016) - Scaling scheme: Lal modified - Atmosphere: ERA40 - VDM: Muscheler et al. (2005)

675
676 *Table 4. Nevado Sajama ^3He CRE age results.*

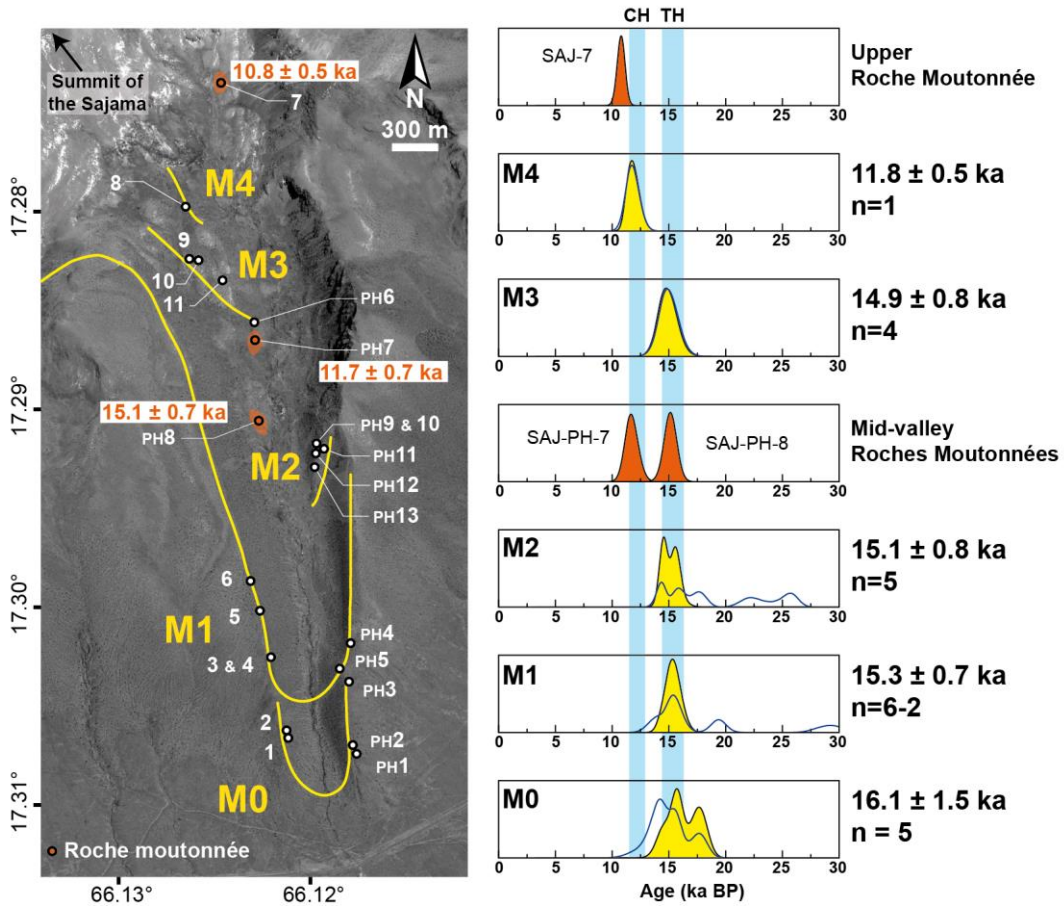

Figure 13. ^{3}He CRE ages on Nevado Sajama. Uncertainties are 1σ. The age PDF of each moraine is reported in yellow. Boulder ages contributing to moraine PDFs beyond 30 ka BP are not represented. Roches moutonnées and their age distributions are reported on the map in orange. For each PDF, the median age is reported. 'n' indicates the number of samples; when n is reported as 'n = A – B', A is the total number of boulders dated on the moraine and B is the number of boulders considered to be outliers. Blue curves are the raw PDFs before Bayesian processing, and the shaded histograms are the final PDFs from which ages were derived (see Section 3.1.5). Blue bars labeled 'TH' and 'CH' indicate the Tauca and Coipasa highstands, respectively.

4.1.4. ^{3}He moraine chronology of Cerro Tunupa

CRE age results from Cerro Tunupa are presented in Table 5 and Figure 14. The age distribution of moraine M1 moraine exhibits a major peak with four boulder ages clustered around 16 ka BP and one outlier older than 20 ka BP that was excluded from the age calculation. After Bayesian processing considering M2 as younger than M1, the four remaining boulders yielded an age of 16.3 ± 0.7 ka BP, synchronous with the end of the Tauca transgression and the first part of the Lake Tauca highstand. For moraine M2, imposing the Bayesian condition that mid-valley roches moutonnées TU-2 and TU-4 are younger than M2 excludes one young outlier at 10.7 ka BP and shifts the remaining distribution towards older ages, yielding a final age of 15.5 ± 0.5 ka BP.

695 The M3 moraine group exhibits more important scatter. Imposing the Bayesian condition that
696 the mid-valley roches moutonnées TU-2 and TU-4 are older partly narrows the M3 age distribution,
697 yielding an age of 13.4 ± 1.1 ka BP. Three roches moutonnées (TU-2, TU-4, TU-13-203) yield ages
698 clustered around 15.2–15.5 ka BP, and one (TU-13-04) a much older age of 21.9 ± 1.3 ka BP; this
699 probably indicates an inherited ^{3}He component. Given that moraine M3 is deposited above roches
700 moutonnées TU-2 and TU-13-203, it must have formed during a glacial re-advance (13–12.5 ka BP)
701 that occurred after the deglaciation at 15.2 ka BP.
702

Glacial Feature	Source	Sample	Latitude Dec°	Longitude Dec°	Altitude masl	Pyroxene Color	Li ppm	Eruption age[a] Ma	Pn $at.g^{-1}.yr^{-1}$	^3He_n 10^5 $at.g^{-1}$	^3He_c (1σ)[b] 10^7 $at.g^{-1}$	Thickness cm	Thick. Corr.[c] -	Shielding[d] -	Scaling Factor[e] -	Age (1σ)[f] ka
M1	Blard et al., 2009	TU-124	-19.8586	-67.6138	4292	-	-	-	-	-	1.99 ± 0.08	2.2	0.98	1.00	9.7	**15.7 ± 0.7**
		TU-1A	-19.8643	-67.6128	4260	-	-	-	-	-	2.02 ± 0.06	3.3	0.97	1.00	9.7	**16.2 ± 0.6**
		TU-1B	-19.8638	-67.6144	4290	-	-	-	-	-	2.21 ± 0.07	2.2	0.98	1.00	9.9	**17.1 ± 0.7**
		TU-1Cf	-19.8652	-67.6099	4206	-	-	-	-	-	2.96 ± 0.13	3.3	0.97	1.00	9.9	**23.1 ± 1.4**
		TU-1D	-19.8691	-67.6054	4083	-	-	-	-	-	1.83 ± 0.06	5.5	0.95	1.00	8.9	**16.2 ± 0.7**
M2	Blard et al., 2009	TU-119	-19.8599	-67.6138	4250	-	-	-	-	-	1.83 ± 0.06	0.5	1.00	0.99	9.4	**14.7 ± 0.6**
		TU-120	-19.8599	-67.6138	4250	-	-	-	-	-	1.79 ± 0.06	0.5	1.00	0.99	9.4	**14.4 ± 0.6**
		TU-121	-19.8590	-67.6147	4267	-	-	-	-	-	1.87 ± 0.13	0.5	1.00	0.99	9.5	**14.8 ± 0.9**
		TU-121 - R	-19.8590	-67.6147	4267	-	-	-	-	-	1.96 ± 0.09	0.5	1.00	0.99	9.6	**15.4 ± 0.7**
		TU-122	-19.8590	-67.6147	4267	-	-	-	-	-	1.74 ± 0.10	0.5	1.00	0.99	9.4	**14.0 ± 0.8**
		TU-123	-19.8588	-67.6149	4275	-	-	-	-	-	1.31 ± 0.05	0.5	1.00	0.98	9.2	**10.7 ± 0.5**
Roches Moutonnées	Blard et al., 2009	TU-4	-19.8570	-67.6180	4260	-	-	-	-	-	1.89 ± 0.07	2.2	0.98	0.98	9.6	**15.5 ± 0.6**
	Blard et al., 2009	TU-2	-19.8455	-67.6272	4450	-	-	-	-	-	2.08 ± 0.06	3.3	0.97	0.98	10.5	**15.7 ± 0.6**
	This Study	TU-13-04	-19.8430	-67.6271	4461	Black	87	1.20	0.3297	3.96E+05	3.19 ± 0.17	2.8	0.98	0.98	11.2	**21.9 ± 1.3**
		TU-13-203	-19.8442	-67.6278	4462	Black	66	1.38	0.2545	3.51E+05	2.04 ± 0.10	5.0	0.96	0.98	10.5	**15.3 ± 0.7**
M3	Blard et al., 2009	TU-3A	-19.8446	-67.6259	4415	-	-	-	-	-	1.57 ± 0.06	2.2	0.98	0.98	10.0	**12.2 ± 0.6**
		TU-3A - R	-19.8446	-67.6259	4415	-	-	-	-	-	1.63 ± 0.07	2.2	0.98	0.98	10.0	**12.7 ± 0.7**
		TU-3B	-19.8446	-67.6259	4415	-	-	-	-	-	1.81 ± 0.05	2.2	0.98	0.98	10.1	**14.1 ± 0.5**
	This Study	TU-13-201	-19.8443	-67.6268	4432	Black	51	0.57	0.4736	2.71E+05	1.86 ± 0.11	1.7	0.99	0.98	10.1	**14.0 ± 0.8**
		TU-13-201 - R	-19.8443	-67.6268	4432	Green	45	1.72	0.4179	7.18E+05	1.65 ± 0.07	1.7	0.99	0.98	10.1	**12.4 ± 0.7**
		TU-13-202	-19.8441	-67.6275	4457	Green	50	2.06	0.3340	6.88E+05	2.36 ± 0.09	5.0	0.96	0.98	10.7	**17.3 ± 0.8**
		TU-13-204	-19.8447	-67.6276	4456	Black	51	0.84	0.4651	3.92E+05	1.76 ± 0.10	5.0	0.96	0.98	10.2	**13.5 ± 0.8**
		TU-13-204 - R	-19.8447	-67.6276	4456	Green	48	1.70	0.4378	7.43E+05	1.65 ± 0.07	2.2	0.98	0.98	10.2	**12.4 ± 0.6**
		TU-13-01	-19.8424	-67.6286	4502	Black	61	1.27	0.2345	2.98E+05	2.15 ± 0.12	3.9	0.97	0.99	10.7	**15.6 ± 0.8**
		TU-13-02	-19.8426	-67.6278	4480	Black	54	1.49	0.2092	3.11E+05	2.36 ± 0.12	2.2	0.98	0.99	10.8	**16.8 ± 0.9**
		TU-13-03	-19.8426	-67.6275	4467	Black	48	1.49	0.1773	2.65E+05	3.23 ± 0.17	4.5	0.96	0.98	11.2	**22.5 ± 1.5**

R replicate. For the sample from this study, replicates have been used to compare ^3He concentrations from black and green pyroxenes

[a] (U-Th-Sm)/^4He age

[b] $He_c = He_{tot} - He_n - He_m$ (we considered $He_m = 8.5 \times 10^4$ $at.g^{-1}$ for all samples)

[c] Calculated with a density of 2.7 $g.cm^{-3}$ and an attenuation length of 160 $g.cm^{-2}$

[d] Shielding from Blard et al. (2009) calculated with the CRONUS application, shielding for samples from this study is negligible

[e] Global scaling factor that accounts for the geomagnetic correction

[f] SLHL PR: weighted mean of the rates from Blard et al. (2013a) and Delunel et al. (2016) - Scaling scheme: Lal modified - Atmosphere: ERA40 - VDM: Muscheler et al. (2005)

Table 5. Cerro Tunupa ^3He CRE age results.

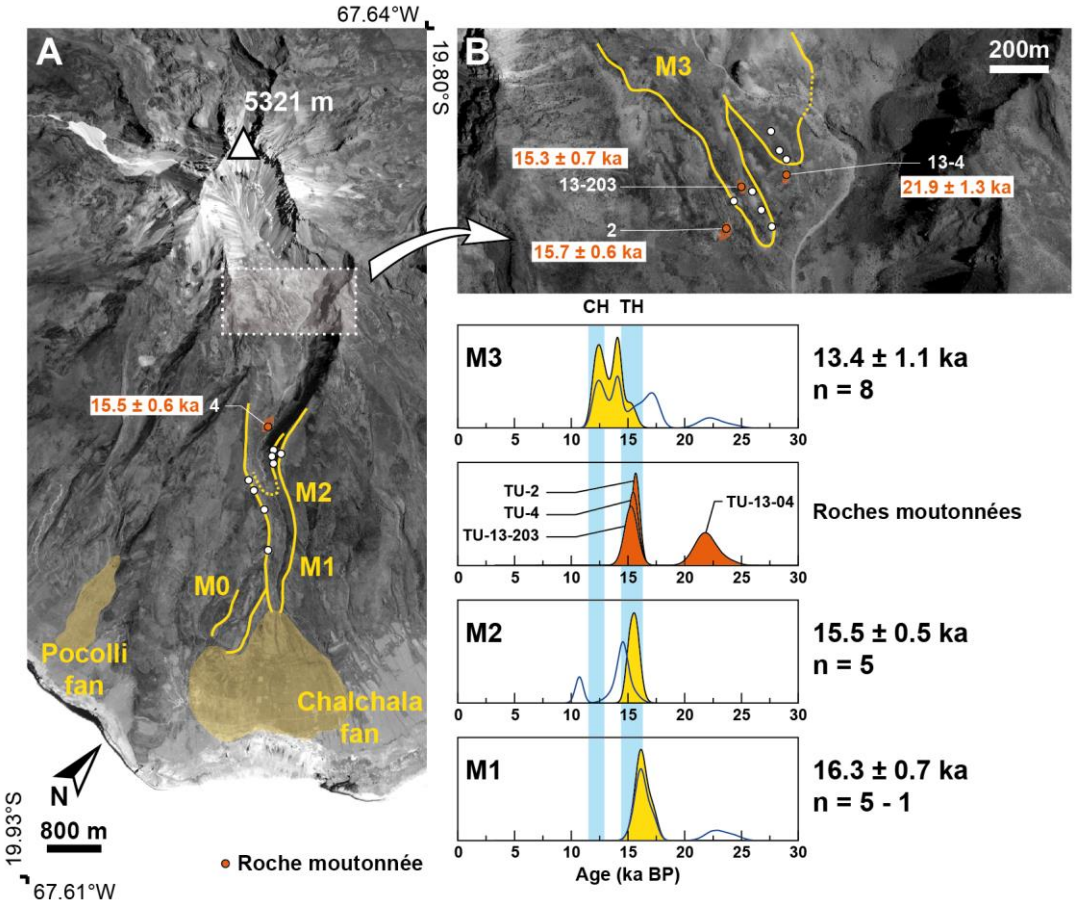

Figure 14. ^{3}He CRE ages on Cerro Tunupa. Uncertainties are 1σ. The age PDF is reported in yellow for each moraine. Boulder ages contributing to the moraine PDF beyond 30 ka BP are not represented. Roche moutonnées and their age distributions are reported on the map in orange. The median age is reported for each PDF. 'n' indicates the number of samples; when n is reported as 'n = A – B', A is the total number of boulders dated on the moraine and B is the number of boulders considered to be outliers. Blue curves are the raw PDFs before Bayesian processing, and the shaded histograms are the final PDFs from which ages were derived (see Section 3.1.5). Blue bars labeled 'TH' and 'CH' indicate the Tauca and Coipasa highstands, respectively.

4.1.5. ^{3}He moraine chronology of Cerro Luxar

CRE age results from Cerro Luxar are presented in Table 6 and Figure 15. The age results at this site present an important scatter, and moraine ages were refined after making several assumptions. For moraine M1, four clustered boulder ages form a major peak around 16 ka BP and the other six boulders returned distinct ages between 21 and 150 ka BP (data are only reported to 30 ka BP in Fig. 15). Five of these six older boulders lie atop frontal moraine branches (Fig. 15); subtle inflections of the moraine crest and changes in boulder density suggest that this distal part may be distinct from M1 and thus associated with an older moraine. We therefore consider these six boulders as outliers with

723 significant inherited ^{3}He components. Imposing the Bayesian condition that M2 is younger than M1, the
724 four remaining samples yield an age of 16.6 ± 0.7 ka BP for M1.

725 M2 presents an obvious outlier at 26 ka BP and a bi-modal peak distribution with the major
726 peak at 17.5 ka BP (n = 3) and the minor peak at 15.5 ka BP (n = 2). Imposing the Bayesian condition
727 that M1 is older and the roches moutonnées LUX-6 and LUX-7 are younger than M2 narrows the age
728 distribution and yields an age of 15.7 ± 0.8 ka BP. The two upper roches moutonnées LUX-6 and LUX-
729 7 have well-clustered ^{3}He ages, indicating a deglaciation of Cerro Luxar around 14.9 ka BP, coeval with
730 the end of the Lake Tauca highstand. The two boulder ages of M3 lie around 20 ka BP and are not
731 consistent with the younger ages (15 ka BP) of the stratigraphically older moraines M1 and M2. We
732 therefore discarded these two boulder ages and derived a Bayesian age distribution for M3 from the
733 PDFs of M2 and the roches moutonnées, considering that M3 is younger than M2 and older than the
734 roches moutonnées (see Section 3.1.5). This derived PDF yields an age of 15.3 ± 0.7 ka BP.

Glacial Feature	Source	Sample	Latitude	Longitude	Altitude	^3He_n [a]	^3He_c (1σ) [b]	Thickness	Thick. Corr. [c]	Shielding	Scaling Factor [d]	Age (1σ) [e]
			Dec°	*Dec°*	*masl*	10^5 *at.g*$^{-1}$	10^7 *at.g*$^{-1}$	*cm*	-	-	-	*ka*
M1	Martin et al., 2018	LUX-1	-21.0096	-68.0129	4230	3.18	**7.22 ± 0.18**	1.0	0.99	0.99	10.8	**50.8 ± 2.7**
		LUX-2	-21.0094	-68.0132	4236	3.18	**4.46 ± 0.17**	4.0	0.97	0.99	10.3	**33.7 ± 1.7**
		LUX-3	-21.0091	-68.0139	4263	3.18	**9.39 ± 0.34**	1.5	0.99	0.99	10.9	**65.4 ± 3.2**
		LUX-10	-21.0085	-68.0128	4228	3.18	**3.26 ± 0.11**	2.0	0.98	0.99	10.1	**24.6 ± 1.2**
		LUX-11	-21.0084	-68.0131	4244	3.18	**2.19 ± 0.08**	1.5	0.99	0.99	9.9	**16.9 ± 0.7**
		LUX-12	-21.0080	-68.0135	4265	3.18	**21.66 ± 0.54**	1.5	0.99	0.99	10.9	**150.6 ± 7.1**
		LUX-11-1	-21.0054	-68.0158	4384	3.18	**2.15 ± 0.09**	2.0	0.98	0.99	10.4	**15.8 ± 0.7**
		LUX-11-2	-21.0047	-68.0164	4418	3.18	**2.04 ± 0.07**	2.0	0.98	0.99	10.4	**15.0 ± 0.6**
		LUX-11-3	-21.0043	-68.0167	4429	3.18	**2.31 ± 0.06**	2.0	0.98	0.99	10.7	**16.5 ± 0.6**
		LUX-11-4	-21.0039	-68.0170	4440	3.18	**3.03 ± 0.09**	2.0	0.98	0.99	11.2	**20.6 ± 0.8**
M2	Martin et al., 2018	LUX-4	-21.0044	-68.0177	4320	3.18	**1.94 ± 0.10**	3.0	0.98	0.99	10.0	**15.0 ± 0.7**
		LUX-5	-21.0043	-68.0180	4383	3.18	**2.42 ± 0.11**	4.0	0.97	0.99	10.6	**17.7 ± 0.8**
		LUX-13	-21.0039	-68.0194	4420	3.18	**3.83 ± 0.15**	2.0	0.98	0.99	11.2	**26.2 ± 1.1**
		LUX-14	-21.0039	-68.0194	4420	3.18	**2.48 ± 0.10**	1.5	0.99	0.99	10.8	**17.5 ± 0.8**
		LUX-15	-21.0036	-68.0200	4431	3.18	**2.18 ± 0.09**	3.0	0.98	0.99	10.6	**15.8 ± 0.7**
		LUX-16	-21.0038	-68.0195	4415	3.18	**2.31 ± 0.09**	5.0	0.96	0.98	10.7	**16.9 ± 0.7**
M3	**This Study**	LUX-11-12	-21.0042	-68.0194	4450	3.18	**2.91 ± 0.20**	3.0	0.98	0.95	11.3	**20.8 ± 1.4**
		LUX-11-13	-21.0042	-68.0194	4454	3.18	**2.69 ± 0.12**	3.0	0.98	0.99	11.1	**18.9 ± 0.9**
Roches Moutonnées	**This Study**	LUX-6	-21.0044	-68.0312	4676	3.18	**2.19 ± 0.12**	5.0	0.96	0.98	11.7	**15.0 ± 0.8**
		LUX-7	-21.0044	-68.0312	4676	3.18	**2.15 ± 0.11**	5.0	0.96	0.98	11.7	**14.8 ± 0.7**

[a] Average value from Tunupa, Uturuncu and Sajama volcano

[b] $He_c = He_{tot} - He_n - He_m$ (we considered $He_m = 8.5 \times 10^4$ at.g^{-1} for all samples)

[c] Calculated with a density of 2.7 g.cm^{-3} and an attenuation length of 160 g.cm^{-2}

[d] Global scaling factor that accounts for the geomagnetic correction

[e] SLHL PR: weighted mean of the rates from Blard et al. (2013a) and Delunel et al. (2016) - Scaling scheme: Lal modified - Atmosphere: ERA40 - VDM: Muscheler et al. (2005)

Table 6. Cerro Luxar ^{3}He CRE age results.

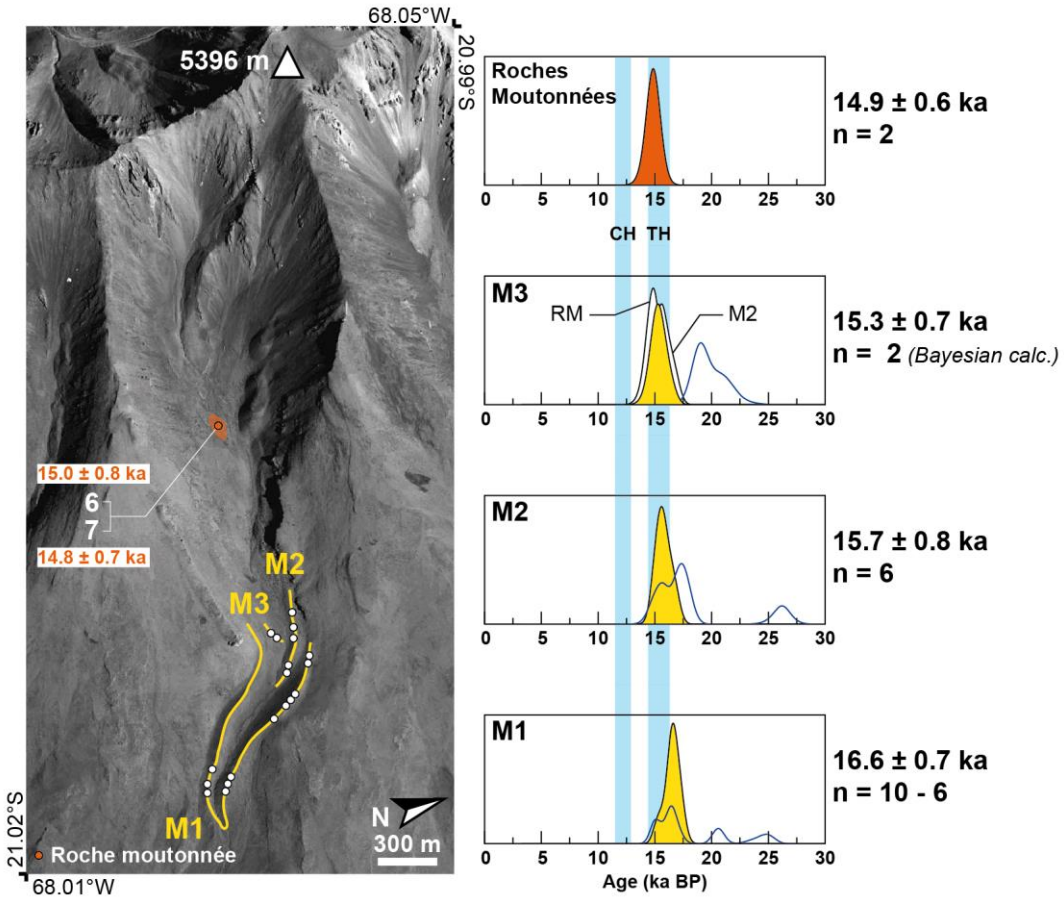

Figure 15. ^{3}He CRE ages on Cerro Luxar. Uncertainties are 1σ. The age PDFs are indicated for each moraine (yellow). Boulder ages contributing to the moraine PDFs beyond 30 ka BP are not represented. Roche moutonnées and their age distributions are reported on the map in orange. The median age is reported for each PDF. 'n' indicates the number of samples; when n is reported as 'n = A – B', A is the total number of boulders dated on the moraine and B is the number of boulders considered to be outliers. The blue curves are the raw PDFs before Bayesian processing, and the shaded histograms are the final PDFs from which ages were derived (see Section 3.1.5). Because the raw ages of M3 were not consistent with the youngest ages of the stratigraphically older moraines, the PDF of M3 was derived from those of M2 and the upper roches moutonnées (see Section 4.1.5). Blue bars labeled 'TH' and 'CH' indicate the Tauca and Coipasa highstands, respectively.

4.2. ELA results

The ELAs computed for each moraine are summarized in Table 7 and Figure 16. This figure also provides global context by comparing the ELA results with several other paleoclimatic proxies. All ELAs between the LGM and the Holocene range between 4,400 and 4,900 m asl. The paleo-ELA changes over the observed periods for Zongo Valley, Cerro Tunupa, and Nevado Sajama are approximately 400, 250, and 200 m, respectively. Comparison between the four sites is, however, limited because the Tunupa and Luxar glacial records stop at around 13 ka BP, whereas the Zongo and Sajama glacial chronologies extend to the Early Holocene (11–10 ka BP). The well-represented

moraines emplaced during the 16–15 ka BP period are synchronous with the Lake Tauca highstand during Heinrich Stadial 1 (Sylvestre et al., 1999; Blard et al., 2009, 2011a; Placzek et al., 2013; Martin et al., 2018). As previously reported by Martin et al. (2018), the ELAs coeval with HS1 show significant regional variability, from 4,388 to 4,800 m asl, reflecting significant heterogeneities of the paleoprecipitation field.

ELAs coeval with the Lake Coipasa highstand (Younger Dryas, c. 12 ka BP) determined from the moraines of Nevado Sajama, Zongo Valley, and Cerro Tunupa are characterized by a smaller variability, ranging between 4,650 and 4,850 m asl.

Site	Moraine	Age[a] *ka BP*	ELA[b] *masl*	Cooling vs. Present[c] *°C vs Present*	Local annual Rainfall vs. Present[c] $P_{Paleo} / P_{Present}$
Zongo Present ELA: 5410 masl[d]	IP3	17.0 ± 0.8	4450 ± 60	-4.9 ± 0.8	1.52 ± 0.24
	IP4	16.0 ± 0.8	4510 ± 60	-4.0 ± 0.6	1.76 ± 0.14
	IP5	13.6 ± 0.8	4560 ± 60	-4.5 ± 0.8	1.42 ± 0.26
	MV	12.6 ± 0.8	4640 ± 40	-3.6 ± 0.6	1.54 ± 0.18
	CQ1	11.6 ± 0.4	4730 ± 30	-3.0 ± 0.4	1.58 ± 0.13
	T1	12.4 ± 1.5	4760 ± 20	-2.9 ± 0.6	1.54 ± 0.23
	T2	11.0 ± 0.8	4790 ± 30	-3.0 ± 0.6	1.41 ± 0.21
	T3	9.8 ± 0.9	4800 ± 30	-3.4 ± 0.4	1.22 ± 0.12
	CQ3	10.7 ± 0.4	4770 ± 30	-3.4 ± 0.5	1.29 ± 0.16
	CQ4	10.1 ± 0.4	4840 ± 30	-3.1 ± 0.3	1.20 ± 0.04
Sajama Present ELA: 5520 masl[d]	M0	16.1 ± 1.5	4660 ± 40	-3.8 ± 1.1	1.81 ± 0.37
	M1	15.3 ± 0.7	4670 ± 30	-3.3 ± 0.8	2.05 ± 0.22
	M2	15.1 ± 0.8	4720 ± 30	-3.0 ± 0.9	2.01 ± 0.30
	M3	14.9 ± 0.8	4800 ± 30	-2.5 ± 0.9	1.99 ± 0.34
	M4	11.8 ± 0.5	4870 ± 30	-2.4 ± 0.9	1.80 ± 0.24
Tunupa Present ELA: 5560 masl[d]	M1	16.3 ± 0.7	4390 ± 40	-4.1 ± 1.1	3.09 ± 0.71
	M2	15.5 ± 0.5	4440 ± 40	-3.2 ± 0.5	3.56 ± 0.21
	M3	13.4 ± 1.1	4630 ± 30	-3.7 ± 1.4	2.20 ± 0.88
Luxar Present ELA: 5930 masl[d]	M1	16.6 ± 0.7	4700 ± 40	-4.6 ± 1.6	3.09 ± 0.95
	M2	15.7 ± 0.8	4750 ± 30	-3.4 ± 1.3	3.80 ± 0.72
	M3	15.3 ± 0.7	4760 ± 30	-3.5 ± 1.4	3.80 ± 0.82

[a] See calculation methods in Section 3.1 and results in Section 4.1
[b] AAR = 0.63 to 0.73 derived from observations on High Andes tropical glacier (Section 3.2)
[c] Uncertainty over the ELA and the present day climate conditions have been propagated
[d] Value computed from the relation of Condom et al. (2007) and the local climatic values from Table 1

Table 7. ELA, temperature and local precipitation results associated with the CRE moraine ages at the four studied sites. For Zongo Valley, we did not compute ELA and cooling vs. present for IP1 and IP2 because we were unable to derive a CRE age for these moraines (see Section 4.1.2), nor those for IPα, which was not part of the main Zongo Valley paleoglacial system (see Section 2.3.1).

.

4.3. Paleoclimatic results

The paleoclimatic inversion method described in Section 3.3 enables the determination of both the local temperature and precipitation associated with each moraine standstill. These results are reported in Table 7 and plotted in Figures 16–18.

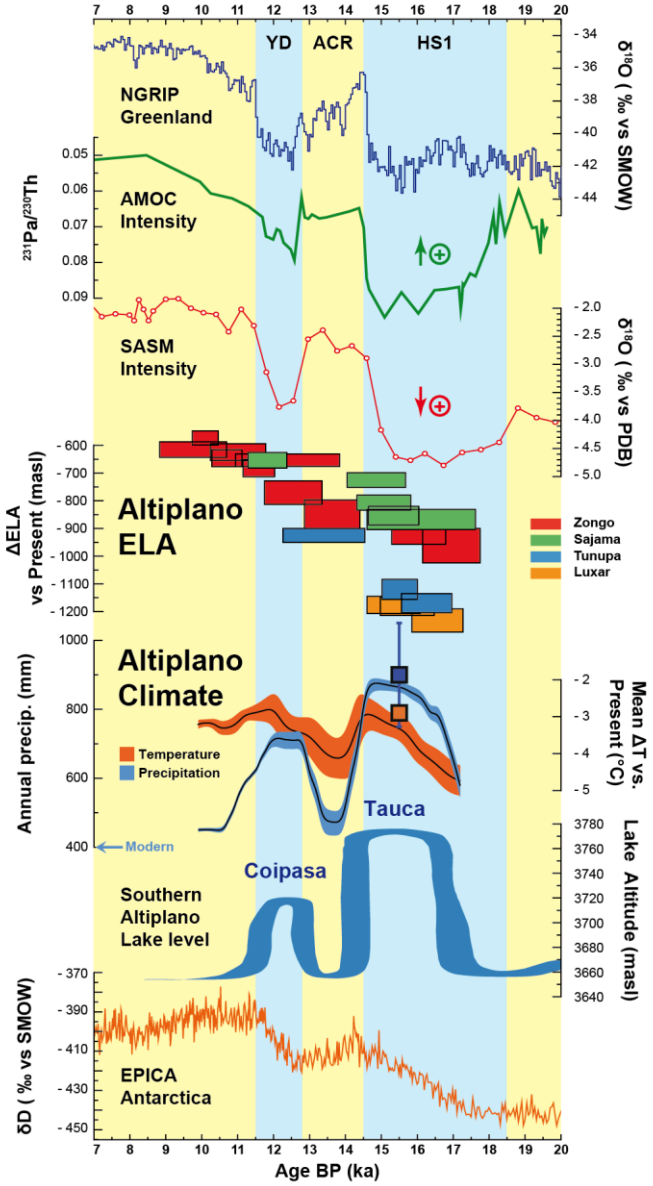

Figure 16. Late-glacial Altiplano ELA and regional precipitation and temperature compared to other late-glacial proxies for the 7–20 ka BP period. NGRIP: $\delta^{18}O$ (‰ vs. SMOW) of the North Greenland ice core (Andersen et al., 2004). AMOC: $^{231}Pa/^{230}Th$ ratio in marine sediments (McManus et al., 2004). SASM: $\delta^{18}O$ (‰ vs. PDB) from Botuvera Cave speleothem carbonates, SE Brazil (Wang et al., 2007). Altiplano ELA: Paleo-ELAs computed in this study for the four studied sites, with 1σ age uncertainties (box widths). Altiplano Climate: regional mean precipitation and temperature values derived from our reconstructions, including precipitation recycling (see Section 4.3.3). Lake level: Lake level reconstruction from shoreline dating in the southern basin of the Altiplano (Fig. 11). Data from Blard et al. (2011a), Placzek et al. (2006), Sylvestre et al. (1999), and the present study. EPICA: δD (‰ vs. SMOW) from the EPICA Dome C ice core (Jouzel et al., 2007).

4.3.1. Temperature results at the glacial sites

The remarkable setting of the Altiplano watershed allows us to interpret the synchronous local glacier and lake records and temporally reconstruct the local temperature for this region (Fig. 17). Reconstructed temperature shifts during the late-glacial period (compared to present day conditions) range from –5 to –2.5 °C. The four sites show behaviors consistent with progressive warming from –5 to –2.5 °C during the Lake Tauca transgression and highstand, followed by colder conditions around –4 °C between the two highstands and the progressive stabilization of the temperature shift at around –3 °C at the onset of the Holocene. The uncertainties associated with these temperature reconstructions are about 1 °C (1σ).

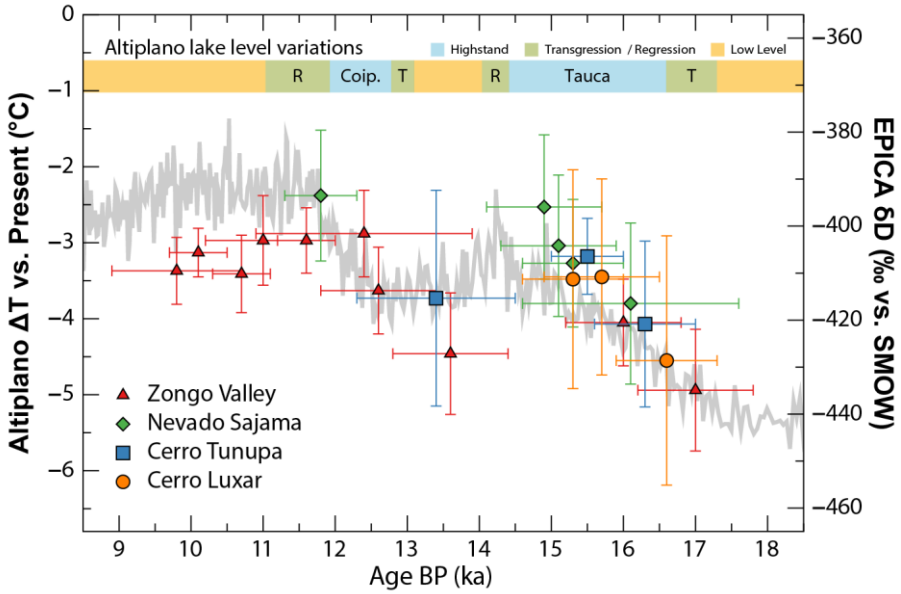

Figure 17. Late-glacial local temperature reconstruction inferred from our paleoglacier and paleolake inversion framework (see Section 3.3). Results are expressed relative to the present day mean annual temperature.

4.3.2. Precipitation results at the glacial sites

The reconstructed precipitation changes (reported here as the ratio $P_{Paleo}/P_{Present}$) at the four studied sites exhibit significantly different behaviors (Fig. 18). The most remarkable feature is the drastically increased precipitation ratio observed during the Tauca highstand for locations near the center of the paleolake. The rainfall ratio is close to 4 at Cerro Luxar and >3 at Cerro Tunupa, ≤2 at the Zongo and Sajama sites. This trend is due to both (i) the strong north-south gradient in the present-day precipitation over the basin, which amplifies the relative precipitation increase when moisture advection

over the basin increases, and (ii) the fact that these sites are too far from the lake to have been affected by substantial rainfall amplification due to local water recycling. The higher ratio observed at Cerro Luxar compared to Cerro Tunupa might appear counterintuitive because Cerro Luxar is near the southwestern shoreline edge of the paleolakes, whereas Cerro Tunupa is in the center of the lake. However, this feature directly results from the shape of the regional rainfall field.

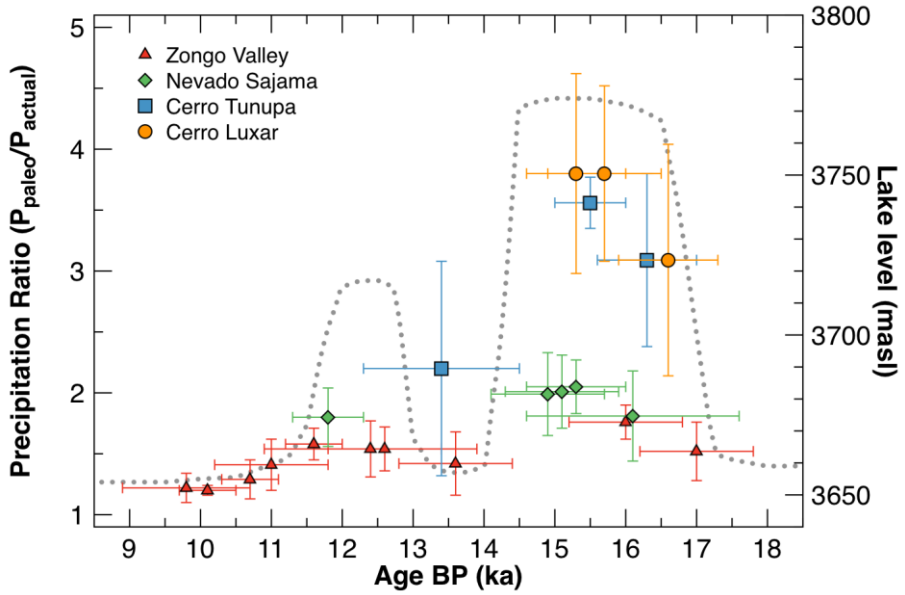

Figure 18. Late-glacial local precipitation reconstruction (derived from the paleoglacier and paleolake inversion framework; see Section 3.3). Results are normalized relative to present-day precipitation (Table 1).

4.3.3. Regional temperature and precipitation

From the local temperature reconstruction presented in Figure 17, we calculated the mean regional temperature (relative to present-day temperature) and precipitation curves over the entire deglaciation (17–10 ka BP, both curves in Fig. 16). We derived the regional temperature curve by temporally averaging the individual moraine points from the four sites and accounting for their individual uncertainties. Using this mean regional temperature curve and its uncertainty envelope, we used the inversion algorithm (see Section 3.3) to reconstruct the precipitation field over the basin and derive the mean regional annual precipitation curve (Fig. 16). During the deglaciation, the regional temperature curve is characterized by a millennial variability. The mean ΔT value (relative to present-day) increases from –5 to –2.5 °C between 17 and 14.5 ka BP, then decreases to –4.5 °C during the ACR, increases up to –2.5 °C during the Younger Dryas, and finally stabilizes around –3 °C at the onset

of the Holocene, between 11.5 and 10 ka BP. The uncertainty associated with this signal remains around ± 0.5 °C during most of the deglaciation period. Precipitation follows similarly: the mean annual rainfall increases from 530 to 960 mm during the Tauca transgression and highstand, then decreases to 510 mm between the two highstands, reaches 690 mm during the Coipasa highstand, and finally stabilizes around 450 mm at the onset of the Holocene. The uncertainty associated with this signal never exceeds ± 25 mm during the study period.

5. Discussion

5.1. Glacial chronologies

5.1.1. Zongo Valley

The updated glacial chronology of Zongo Valley yields meaningful results. Only three of the 13 analyzed moraines show very high scatter: IP1, IP2, and MV. Given their location, IP1 and IP2 must be older than 17 ka BP, and they are not discussed further in this study. The Bayesian constraints brought by IP5 and CQ1 on MV enabled us to derive its age with an uncertainty better than 1 kyr. Other moraines either present clear outliers (e.g. IP4) or relatively clustered ages. For these moraines, the Bayesian filtering had only a marginal effect on the age distributions. The exceptions to these general observations are the T1 and T2 Telata moraines that exhibit significant scatter; their age distributions were importantly modified by the Bayesian constraints. Nonetheless, their ELAs are in good agreement with those of the same age throughout the rest of the valley. IP3 and IP4 indicate that the local last glacial maximum (LLGM) occurred before 17 ka BP. The ELA changes remain limited between 17 and 13.5 ka BP in Zongo Valley (ΔELA < 100 m). A 10-km horizontal retreat from IP5 to CQ4 subsequently occurred over a 3–3.5 kyr interval, corresponding to an ELA rise of almost 300 m. IP5 is coeval with the ACR (14.5–12.9 ka BP) and CQ1 with the Younger Dryas (12.8–11.5 ka BP). The CQ3, CQ4, and Telata moraines are concomitant with the Pleistocene-Holocene transition.

5.1.2. Nevado Sajama

Smith et al. (2009) used ^{36}Cl cosmogenic data to establish the first glacial chronology for Nevado Sajama. In agreement with their results, our ^{3}He dataset confirms the presence of late-glacial moraines on Nevado Sajama. However, the important scatter of their ^{36}Cl ages (possibly due to inter-sample variability in Cl content; Schimmelpfennig et al., 2009) precludes a more detailed comparison with our results.

Nevado Sajama records a major glacial advance around 16 ka BP, coeval with the end of the transgression and the beginning of the Lake Tauca highstand. The ELA shift between 16 and 15 ka BP is less than 60 m (2 km of horizontal retreat), suggesting that climatic conditions remained relatively stable during this period. The age of moraine M4 is coeval with the end of the Coipasa highstand, and its corresponding ELA (4,871 m asl) is not significantly higher than that at the end of the Tauca highstand as observed on moraine M3 (ELA = 4,800 m asl). However, our results do not permit evaluation of whether the Sajama glaciers receded above the M4 moraine front or remained stationary between 15 and 12 ka BP. A major glacial retreat probably occurred after the end of the Coipasa highstand-Younger Dryas stadial.

5.1.3. Cerro Tunupa

Our recalculation does not substantially change the initial conclusions of Blard et al. (2009, 2013a). As they reported, the Tunupa moraines record a major glacial advance around 16.3 ka BP (M1), followed by the standstill that built moraine M2 synchronous to the Lake Tauca highstand-Heinrich 1 stadial (15.5 ± 0.5 ka BP). Our ^{3}He CRE ages of the upstream roches moutonnées confirm that this standstill was followed by a rather abrupt glacial retreat after 15 ka BP and an associated ELA shift of 200 m just before (or synchronous to, within uncertainties) the Lake Tauca regression at 14.5 ka BP (Fig. 14).

5.1.4. Cerro Luxar

As recently established by Martin et al. (2018), moraines M1 and M2 indicate rather stable climatic conditions synchronous to the Lake Tauca highstand from 16.1 to 15.2 ka BP, with an ELA

standing between 4,700 and 4,750 m asl. Additionally, our ^{3}He CRE ages of upstream roches moutonnées indicate a rapid glacial retreat just after 15 ka BP and nearly synchronous to the Lake Tauca regression (Fig. 15), as observed at Cerro Tunupa.

5.1.5. Overview

The Sajama, Tunupa, and Luxar moraines present rather similar glacial chronologies. They all record a major glacial standstills or re-advances around 16–15 ka BP coeval with the Tauca highstand. All three sites experienced a significant glacial retreat during the last centuries of the highstand or during the Lake Tauca regression. Tunupa and Luxar experienced the most significant ELA decrease, likely due to their proximity to the center of the paleolake. On Nevado Sajama, the ice tongue stabilized in the upper part of the valley during the Younger Dryas before later retreating.

Zongo Valley exhibits a slightly more complex pattern: although the Tauca moraine is also observed in this valley, the paleoglaciation there is characterized by a LLGM older than 17 ka BP, and the persistence of climatic conditions similar to those during the LLGM until 13.5 ka BP. The subsequent rapid and massive glacial retreat was followed by a marked standstill during the Younger Dryas and a progressive retreat during the Early Holocene. This geographic contrast between the paleoglacial behaviors of the Cordillera Real and the southeast Altiplano is consistent with the present day climatic setting of Andean glaciers (Sagredo and Lowell, 2012), probably due to the proximity of the Amazonian moisture source to Zongo Valley.

5.2. Robustness of the paleoclimatic inversion

5.2.1. Uncertainties on reconstructed temperatures

Our temperature reconstruction for the deglaciation period (Fig. 17) has an average uncertainty of ± 0.5 °C, which was propagated from all uncertainties arising from the parametrizations of the lake and glacier models. Some model parameters, such as AAR, are theoretically similar throughout a given valley, implying that the reported errors should be considered maximum values. Importantly, the temperature reconstructions for different sites yield similar and consistent values: the linear temperature increase between 17 and 15 ka BP (during the deglaciation) is defined by the paleoglacial records of

each of the four glaciated valleys. Nearly synchronous temperatures are compatible within less than 0.5 °C, highlighting the regional consistency of our reconstruction. The cooling period during 14–13 ka BP is evidenced by two moraines from different glacial sites (Zongo and Tunupa) that yield consistent temperature values. The final warming period during 13–11 ka BP is defined by several moraines of Zongo Valley and one moraine on Nevado Sajama, all of which are compatible within uncertainties. In summary, the trend in the temperature record is significant.

5.2.2. The climatic conditions recorded by a moraine exposure age: significance, uncertainty and signal filtering

Traditionally, exposure ages of block sitting on top moraines are considered as documenting the final episode of sediment piling and of moraine building, i.e. the final stage of a glacier advance or still stand (Bennett, 2001). Even if uncertainties remain on the exact timing of block stabilization regarding the glacier retreat after a glacier advance (Eichel et al., 2018), as well as on the CRN inheritance of a block acquired during its final supraglacial period of transport (Briner et al., 2005; Heyman et al., 2011), recent dating of Little Ice Age moraines in the Alps have shown that ^{10}Be exposure ages of blocks sitting on moraines are nearly synchronous with the glacier advances documented by historical chronicles (e.g. Schimmelpfennig et al., 2014). Such examples in the Alps suggests that this uncertainty might be lower than 0.1 kyr, i.e. much lower than the uncertainties reported for the exposure ages in the present study (0.5 to 1 kyr). The exact representativeness of CRN ages of boulders on moraine therefore probably has little bearing on the interpretation of the moraine ages described in this study. Nevertheless, it should be noted that the final uncertainty on the moraine ages, as well as the propagation of this uncertainty on the paleolake level to calculate paleo-temperatures and paleoprecipitation, implies that the paleoclimatic curves obtained are smoothed at the millennial scale and filtered from their high-frequency content. As such, our paleoclimatic reconstructions based on moraines preclude discussion on high frequency climate variation and abrupt transition at the centennial scale.

925 *5.2.3. Comparison with previous regional temperature and precipitation*
926 *reconstructions*

927 Our reconstruction provides the first continuous records of absolute temperature and
928 precipitation throughout the deglaciation period for the Altiplano. As such, our reconstructions can only
929 punctually be compared to other regional studies. Blard et al. (2009) and Martin et al. (2018) focused
930 on the Lake Tauca highstand (16–15 ka BP), whereas Placzek et al. (2013) established mean
931 precipitation and temperature records for three successive lake highstands: Lake Sajsi (24–20 ka BP),
932 Lake Tauca (16–15 ka BP), and Lake Coipasa (12 ka BP). Our temperature and precipitation records
933 for the Lake Tauca highstand are consistent with the 3 °C cooling and mean regional precipitation of
934 900 mm yr^{-1} ($P_{Tauca}/P_{Present} = 2.2$) obtained by Martin et al. (2018; square symbols in Fig. 16). However,
935 these paleoclimatic conditions differ from the cooler ($\Delta T_{Tauca} \approx -4$ to -7 °C) and drier conditions
936 ($P_{Tauca}/P_{Present} < 2$) inferred by Blard et al. (2009) and Placzek et al. (2013) for the Lake Tauca highstand.
937 This discrepancy probably arises from the combination of three factors. First, our study uses an up-to-
938 date and more accurate approach to estimate the spatial distribution of precipitation. This new approach
939 is based on our recent work (Martin et al., 2018), and is more relevant than those of the pioneer studies
940 of Blard et al. (2009) and Placzek et al. (2013) because the spatial distribution of precipitation now
941 accounts for both the entire regional ELA variability and the distributed lake recycling anomaly
942 throughout the southern part of the catchment. Second, we used a different model to convert paleo-ELAs
943 into paleoclimatic variables (P, T). Blard et al. (2009) applied a PDD model, which tends to overestimate
944 the temperature sensitivity of ablation in arid regions receiving snow accumulations < 500 mm yr^{-1}
945 (Blard et al., 2011b; Sicart et al., 2008), whereas we used the robust empirical model of Condom et al.
946 (2007). Third, we used newer data to define the present-day climatic conditions: whereas Placzek et al.
947 (2013) considered a mean annual temperature of 10.8 °C at 3,800 m asl for the entire Altiplano, our
948 compilation of present-day weather station data yielded spatially variable means from ~6.3 to 8.5 °C at
949 3,800 m asl (Table 1; Martin et al., 2018). Regarding the Early Holocene period (10–8 ka BP), Jomelli
950 et al. (2011) reported a cooling of ~3 °C based on Cerro Telata moraines, which is similar to that derived
951 herein for the nearby Zongo Valley. Although they used a PDD model, the consistency with our results

952 is likely due to the fact that this region is fed by abundant precipitation (annual snow accumulation >
953 1,000 mm a^{-1}). Indeed, under such wet conditions, PDD models yield an ELA-climate sensitivity similar
954 to that of the empirical model used here (Condom et al., 2007).

955 The glacier ice core $\delta^{18}O$ records from Huascarán (Peru) and Sajama (Bolivia) have been used
956 to suggest that Andean temperatures during the deglaciation were similar to those in Greenland and the
957 North Atlantic, with HS-1 notably being the coldest period of the past ~19 ka BP (Thompson et al.,
958 1995, 1998). However, other studies have argued that the O isotopic compositions of tropical ice cores
959 do not provide a pure temperature signal because they are also controlled by the composition of
960 precipitation and atmospheric processes (Ramirez et al., 2003). The $\delta^{18}O$ signal in tropical ice may also
961 have been biased by vapor originating from Lakes Tauca and Coipasa, water sources with high $\delta^{18}O$
962 values (Quesada et al., 2015).

963 **5.3. Regional and global paleoclimatic implications**

964 Our reconstruction of both absolute precipitation and temperature during the last deglaciation
965 represents a unique dataset documenting the regional and global paleoclimatic mechanisms affecting
966 the southern Tropical Andes. Our new reconstructions reveal that (i) precipitation variability over the
967 Altiplano reacted synchronously with the Greenland-Atlantic dynamic during the deglaciation
968 (Andersen et al., 2004; McManus et al., 2004), whereas (ii) temperatures were in phase with Antarctic
969 temperature fluctuations (Jouzel et al., 2007). These new observations are key in deciphering the
970 paleoclimatic connections between the Northern and Southern Hemispheres and the Tropics.

971 *5.3.1 Precipitation results*

972 Several studies have identified connections between precipitation in the Tropical Andes and the
973 abrupt climatic oscillations of the Northern Hemisphere during the last deglaciation (Baker et al., 2001;
974 Blard et al., 2011a; Crivellari et al., 2018; Fritz et al., 2007; Gayo et al., 2012; Haug, 2001; Licciardi et
975 al., 2009; Martin et al., 2018; Placzek et al., 2006). However, until now, a continuous absolute record
976 of Altiplano paleoprecipitation during the last deglaciation was not available. Filling this gap, our

977 reconstruction supports an interhemispheric connection between precipitation over the Altiplano,
978 temperatures in Greenland, and the Atlantic meridional overturning circulation (AMOC) during the
979 entire deglaciation (Fig. 16). However, our results do not allow us to extend this observation beyond the
980 Altiplano Basin to the entire tropical Andes.

981 Martin et al. (2018) reconstructed the spatial variability of precipitation at unprecedented resolution
982 during the Lake Tauca highstand (Heinrich 1 event) and suggested that atmospheric mechanisms
983 modulated the SASM, producing major precipitation changes over the Altiplano. Increases in
984 precipitation likely resulted from southward displacement and intensification of the Bolivian High (a
985 high-pressure cell), which enabled substantial westward moisture advection towards the Altiplano
986 Basin. A continental forcing of this phenomenon might be fluctuations of the South Atlantic
987 Convergence Zone (SACZ), which controls the position and intensity of the Bolivian High (Lenters and
988 Cook, 1999) and showed extreme fluctuations during the Tauca highstand ("Mega-SACZ" events;
989 Stríkis et al., 2015). Similar events can be invoked to explain the abundant precipitation during the
990 Coipasa highstand.

991 The mechanisms linking changes of the SASM to the global climate remain debated. Additional
992 reconstructions of continental precipitation during the last deglaciation based on inverse glacier
993 modeling could contribute to better identifying the controlling atmospheric patterns. However, the
994 southward migration of synoptic atmospheric features during cold periods in the North Atlantic has been
995 repeatedly observed or modeled for the Northern Westerlies (Roe and Lindzen, 2001; Zhang et al.,
996 2014), the Intertropical Convergence Zone (Crivellari et al., 2018; Kanner et al., 2012; Peterson, 2000),
997 and the Southern Westerlies (Anderson et al., 2009; Denton et al., 2010; Toggweiler et al., 2006).

998 *5.3.2 Temperature results*

999 Only a few empirical studies have suggested common Antarctic and Tropical atmospheric
1000 temperature patterns. The meta-analysis of Tropical Andean moraine ages by Jomelli et al. (2014)
1001 showed that most Tropical Andean glaciers had a greater extent during the ACR than during the Younger
1002 Dryas. They also used a transient general circulation model (GCM) simulation to show that the
1003 connection between Southern Hemispheric and Tropical temperatures results from a combination of

1004 several atmospheric mechanisms, including AMOC modulation, CO_2 level, precipitation, vegetation,
1005 and local heat budgets. However, Groot et al. (2011) presented a contradictory paleotemperature dataset;
1006 based on a continuous 284-kyr-long pollinic record from a core drilled in Lake Fúquene, Columbia
1007 (5°N, 2,540 m asl), they asserted that temperature fluctuations in Columbia follow North Atlantic-
1008 Greenland fluctuations on glacial-interglacial time scales.

1009 In this context, our results show that an Antarctic-like temperature pattern characterized the high
1010 Andes, at least as far north as 15°S, during the last deglaciation, with a linear warming trend of ~2.5 °C
1011 during 17–14.5 ka BP, a return to conditions ~1.5 °C colder during the ACR (14.5–13 ka BP), a second
1012 warming of ~1.5 to 2 °C during 13–12 ka BP, and a subsequent stabilization of temperatures during the
1013 early Holocene (Fig. 17). This trend is remarkably consistent with temperature variations in Antarctica
1014 over the same period, as recorded by the H isotopic composition of ice cores (Fig. 17). This correlation
1015 suggests a homogeneous, large-scale temperature evolution in the Southern Hemisphere, i.e. from the
1016 southernmost latitudes to the southern Tropical Andes, during the last deglaciation. This similarity
1017 between tropical and Antarctic temperatures may also result from a common response of both regions
1018 to independent, but synchronous, forcings. Barker et al. (2011) established that temperature variations
1019 in the Antarctic and Southern Ocean regions are partially controlled by the bipolar seesaw, and thus, by
1020 AMOC fluctuations. Moreover, at seasonal to inter-annual time scales, the southerly flow of Antarctic
1021 glacial air masses is thought to control significant cooling in the southern and mid-latitude Andes
1022 (Schneider et al., 2003). If the frequency of such airflow intrusions increased and persisted over
1023 millennial timescales, it could explain the Antarctic-like temperature pattern of the Altiplano as
1024 observed herein.

1025 However, the temperature pattern of the Altiplano observed during the last deglaciation could
1026 also reflect a regional response to variations in regional precipitation via their impact on the energy
1027 budget. This could explain the positive correlation between precipitation and temperature over the
1028 Altiplano, with the warmest periods being associated with the wettest events (Fig. 16). Further studies
1029 employing high-resolution GCM simulations over that Late Pleistocene-Holocene transition will be key
1030 to disentangling these various scenarios.

5.4. A note on the use of glacial fluctuations as paleoclimatic proxies

An important methodological conclusion that can be drawn from our paleoclimatic reconstruction is that paleoglacial fluctuations may not simply be a proxy for temperature that can be directly used to infer large-scale paleoclimatic changes. In dry regions where glacial mass balances are under a precipitation-limited regime, such a simplification may yield inaccurate conclusions. For example, our data show that, despite atmospheric warming during the last deglaciation (17–15 ka BP), Altiplano glaciers advanced due to increased precipitation concomitant with the Lake Tauca highstand (Fig. 18). Although temperature is the main control of glacier dynamics, substantial precipitation variations modulate glacial advances and retreats, and can counterbalance or even surpass the effects of slight warming. For example, according to equation (2), a precipitation increase of 1000 to 1600 $mm.yr^{-1}$ can compensate a 2°C warming. Such glacier fluctuations regionally driven by precipitations might appear as a rather counter intuitive result. According to this mechanism, local moisture increase during the YD may have triggered glacier readvances that have erased the moraines left by the former and colder period of the ACR.

Such obliteration could be of limited spatial extent, and could have occurred in areas affected by a marked local increase in precipitation, such as promoted by moisture recycling in the vicinity of a large lake. This might explain why preserved ACR moraines are less prevalent in the central Altiplano than in other regions of the wet Tropical Andes (Jomelli et al., 2014). Therefore, the potential importance of the respective roles of precipitation and temperature should be carefully considered in future paleoclimatic studies relying on paleo-ELA reconstructions, ideally by coupling the interpretation of paleo-ELA inventories with independent proxies of precipitation and temperature.

6. Concluding remarks

In Zongo Valley, the oldest glacial extent for which geochronological constraints are available (≥17 ka BP) was approximately maintained until 13.5 ka BP, and was followed by a massive glacial retreat until the early Holocene. This retreat was associated with an ELA variation of 300 m. Nevado Sajama, Cerro Tunupa, and Cerro Luxar exhibit moraines synchronous with the Tauca Lake highstand (c. 16 ka BP), followed by different retreat timings. For these three sites, the ELA rose by ~200 m after the end of the Tauca highstand.

At the scale of individual glacial sites, our precipitation reconstruction is characterized by a strong spatial variability during the Tauca highstand due to lake-enhanced precipitation. At the regional scale, precipitation variations over the Altiplano basin were paced by the Northern Hemispheric dynamic, with the wettest period on the Altiplano being synchronous to the cold HS1a and Younger Dryas events. Our regional temperature reconstruction shows good consistency with Antarctic temperatures: the temperature curve (relative to present-day temperatures) defines (i) a linear warming trend from –5 to –2.5 °C during 17–14.5 ka BP, (ii) a return to colder conditions (–4 °C) during 14.5–13 ka BP, (iii) a second warming after 13 ka BP (to –3 °C), followed by (iv) the stabilization of temperatures into the Early Holocene.

Because the conditions within the Altiplano basin were sufficiently cold for glacial settlement and growth, glacial dynamics were driven by the regional precipitation increase during the Lake Tauca and Lake Coipasa highstands, which explains the abundance of morainic records synchronous with the Tauca highstand despite warming temperatures. Outside of these periods, glaciers were driven by large-scale temperature variations. Our results provide an original framework for understanding why the ACR is more represented than the Younger Dryas among morainic records throughout the Tropical Andes, and why North Atlantic cooling events (coeval with Altiplano lake highstands), that enhanced local precipitation, correspond to glacial advances over the Altiplano basin. These results exemplify that paleoglacial variations cannot solely be interpreted in terms of temperature variations, and that regional precipitation patterns can significantly affect glacial dynamics.

Acknowledgments

This work was funded by the INSU EVE-LEFE program and the ANR Jeunes Chercheurs GALAC project (ANR-11-JS56-011-01). We greatly appreciated the logistical support of the Institut de Recherche pour le Développement (IRD) of La Paz (Bolivia) during our field trips between 2010 and 2013. The ASTER French national AMS facility (CEREGE, Aix-en-Provence) is supported by INSU/CNRS, the ANR through the "Equipements d'Excellence" program, IRD, and CEA. Field measurements of mass balance and ELA on Bolivian and Ecuadorian glaciers were provided by the Andean part of the Service National d'Observation GLACIOCLIM, funded by the French IRD, the Universidad Mayor de San Andres (IGEMA, IHH) in Bolivia and the Insituto Nacional de Meteorologia e Hidrologiain Ecuador.

We warmly thank C. Hautefeuille and Benj Barry for their contributions to the Luxar datings, P. Burnard, B. Tibari, and L. Zimmerman for essential help with the SFT mass spectrometer and related devices during analytic sessions, V. Mariotti and M. Prémaillon for their help during field trips and sample collection, Flo Gallo, M. Protin, and D. Brunstein for their support during ^{10}Be chemical analyses, and L. Tissandier and Y. Marrocchi for help with SEM and mineral analyses. We are grateful to the SARM-CNRS for high quality chemical analyses. E. Davy, R. Joussemet and the STEVAL crew (GeoRessources, Nancy) are acknowledged for their technical support during sample crushing and mineral separation. We thank R. Dennen and rd-editing.com for in-depth language editing. We are deeply grateful for the constructive feedback provided by the reviewers, which helped to improve the manuscript clarity.

References

Aceituno, P., 1996. Elementos del clima en el Altiplano Sudamericano. Rev. Geofis. 44, 37–55.

Ammann, C., Jenny, B., Kammer, K., Messerli, B., 2001. Late Quaternary Glacier response to humidity changes in the arid Andes of Chile (18–29°S). Palaeogeogr. Palaeoclimatol. Palaeoecol. 172, 313–326. https://doi.org/10.1016/S0031-0182(01)00306-6

Andersen, K.K., Azuma, N., Barnola, J.-M.J.-M., Bigler, M., Biscaye, P., Caillon, N., Chappellaz, J., Clausen, H.B., Dahl-Jensen, D., Fischer, H., Flückiger, J., Fritzsche, D., Fujii, Y., Goto-Azuma, K., Grønvold, K., Gundestrup, N.S., Hansson, M., Huber, C., Hvidberg, C.S., Johnsen, S.J., Jonsell, U., Jouzel, J., Kipfstuhl, S., Landais, A., Leuenberger, M., Lorrain, R., Masson-Delmotte, V., Miller, H., Motoyama, H., Narita, H., Popp, T., Rasmussen, S.O., Raynaud, D., Rothlisberger, R., Ruth, U., Samyn, D., Schwander, J., Shoji, H., Siggard-Andersen, M.-L.M.-L., Steffensen, J.P., Stocker, T., Sveinbjörnsdóttir, A.E., Svensson, A., Takata, M., Tison, J.-L.J.-L., Thorsteinsson, T., Watanabe, O., Wilhelms, F., White, J.W.C., 2004. High-resolution record of Northern Hemisphere climate extending into the last interglacial period. Nature 431, 147–51. https://doi.org/10.1038/nature02805

Anderson, R.F., Ali, S., Bradtmiller, L.I., Nielsen, S.H.H., Fleisher, M.Q., Anderson, B.E., Burckle, L.H., 2009. Wind-Driven Upwelling in the Southern Ocean and the Deglacial Rise in Atmospheric CO2. Science. 323, 1443–1448. https://doi.org/10.1126/science.1167441

Andrews, J.N., 1985. The isotopic composition of radiogenic helium and its use to study groundwater movement in confined aquifers. Chem. Geol. 49, 339–351. https://doi.org/10.1016/0009-2541(85)90166-4

Andrews, J.N., Kay, R.L.F., 1982. Natural production of tritium in permeable rocks. Nature 298, 361–363. https://doi.org/10.1038/298361a0

Argollo, J., Mourguiart, P., 2000. Late Quaternary climate history of the Bolivian Altiplano. Quat. Int. 72, 37–51. https://doi.org/10.1016/S1040-6182(00)00019-7

Baker, P. a, Seltzer, G.O., Fritz, S.C., Dunbar, R.B., Grove, M.J., Tapia, P.M., Cross, S.L., Rowe, H.D., Broda, J.P., 2001. The history of South American tropical precipitation for the past 25,000 years. Science 291, 640–3. https://doi.org/10.1126/science.291.5504.640

Balco, G., Stone, J.O., Lifton, N. a., Dunai, T.J., 2008. A complete and easily accessible means of calculating surface exposure ages or erosion rates from 10Be and 26Al measurements. Quat. Geochronol. 3, 174–195. https://doi.org/10.1016/j.quageo.2007.12.001

Barker, S., Diz, P., Vautravers, M.J., Pike, J., Knorr, G., Hall, I.R., Broecker, W.S., 2009. Interhemispheric Atlantic seesaw response during the last deglaciation. Nature 457, 1097–1102. https://doi.org/10.1038/nature07770

Barker, S., Knorr, G., Edwards, R.L., Parrenin, F., Putnam, A.E., Skinner, L.C., Wolff, E., Ziegler, M., 2011. 800,000 Years of Abrupt Climate Variability. Science 334, 347–51. https://doi.org/10.1126/science.1203580

Benn, D.I., Lehmkuhl, F., 2000. Mass balance and equilibrium-line altitudes of glaciers in high-mountain environments. Quat. Int. 65–66, 15–29. https://doi.org/10.1016/S1040-6182(99)00034-8

Benn, D.I., Owen, L.A., Osmaston, H.A., Seltzer, G.O., Porter, S.C., Mark, B., 2005. Reconstruction of equilibrium-line altitudes for tropical and sub-tropical glaciers. Quat. Int. 138–139, 8–21. https://doi.org/10.1016/j.quaint.2005.02.003

Bennett, M.R., 2001. The morphology, structural evolution and significance of push moraines. Earth-Science Rev. 53, 197–236. https://doi.org/10.1016/S0012-8252(00)00039-8

Blard, P.-H., Balco, G., Burnard, P.G., Farley, K.A., Fenton, C.R., Friedrich, R., Jull, A.J.T., Niedermann, S., Pik, R., Schaefer, J.M., Scott, E.M., Shuster, D.L., Stuart, F.M., Stute, M., Tibari, B., Winckler, G., Zimmermann, L., 2015. An inter-laboratory comparison of cosmogenic 3 He and radiogenic 4 He in the CRONUS-P pyroxene standard. Quat. Geochronol. 26, 11–19. https://doi.org/10.1016/j.quageo.2014.08.004

Blard, P.-H., Braucher, R., Lavé, J., Bourlès, D., 2013a. Cosmogenic 10Be production rate calibrated against 3He in the high Tropical Andes (3800–4900 m, 20–22° S). Earth Planet. Sci. Lett. 382, 140–149. https://doi.org/10.1016/j.epsl.2013.09.010

Blard, P.-H., Lavé, J., Farley, K. a., Fornari, M., Jiménez, N., Ramirez, V., 2009. Late local glacial maximum in the Central Altiplano triggered by cold and locally-wet conditions during the paleolake Tauca episode (17–15ka, Heinrich 1). Quat. Sci. Rev. 28, 3414–3427. https://doi.org/10.1016/j.quascirev.2009.09.025

Blard, P.-H., Lave, J., Farley, K. a., Ramirez, V., Jimenez, N., Martin, L.C.P., Charreau, J., Tibari, B., Fornari, M., 2014. Progressive glacial retreat in the Southern Altiplano (Uturuncu volcano, 22°S) between 65 and 14 ka constrained by cosmogenic 3He dating. Quat. Res. 82, 209–221. https://doi.org/10.1016/j.yqres.2014.02.002

Blard, P.-H., Lavé, J., Sylvestre, F., Placzek, C.J., Claude, C., Galy, V., Condom, T., Tibari, B., 2013b. Cosmogenic 3He production rate in the high tropical Andes (3800 m, 20°S): Implications for the local last glacial maximum. Earth Planet. Sci. Lett. 377–378, 260–275. https://doi.org/10.1016/j.epsl.2013.07.006

Blard, P.-H., Sylvestre, F., Tripati, A.K., Claude, C., Causse, C., Coudrain, A., Condom, T., Seidel, J.-L., Vimeux, F., Moreau, C., Dumoulin, J.-P., Lavé, J., 2011a. Lake highstands on the Altiplano (Tropical Andes) contemporaneous with Heinrich 1 and the Younger Dryas: new insights from 14C, U–Th dating and δ18O of carbonates. Quat. Sci. Rev. 30, 3973–3989. https://doi.org/10.1016/j.quascirev.2011.11.001

Blard, P.-H., Wagnon, P., Lavé, J., Soruco, A., Sicart, J.-E., Francou, B., 2011b. Degree-day melt models for paleoclimate reconstruction from tropical glaciers: calibration from mass balance and meteorological data of the Zongo glacier (Bolivia, 16° S). Clim. Past Discuss. 7, 2119–2158. https://doi.org/10.5194/cpd-7-2119-2011

Briner, J.P., Kaufman, D.S., Manley, W.F., Finkel, R.C., Caffee, M.W., 2005. Cosmogenic exposure dating of late Pleistocene moraine stabilization in Alaska. Geol. Soc. Am. Bull. 117, 1108. https://doi.org/10.1130/B25649.1

Broecker, W., Putnam, A.E., 2012. How did the hydrologic cycle respond to the two-phase mystery interval? Quat. Sci. Rev. 57, 17–25. https://doi.org/10.1016/j.quascirev.2012.09.024

Broecker, W.S., 1998. Paleocean circulation during the Last Deglaciation: A bipolar seesaw? Paleoceanography 13, 119. https://doi.org/10.1029/97PA03707

Bromley, G.R.M., Schaefer, J.M., Hall, B.L., Rademaker, K.M., Putnam, A.E., Todd, C.E., Hegland, M., Winckler, G., Jackson, M.S., Strand, P.D., 2016. A cosmogenic 10 Be chronology for the local last glacial maximum and termination in the Cordillera Oriental, southern Peruvian Andes: Implications for the tropical role in global climate. Quat. Sci. Rev. 148, 54–67. https://doi.org/10.1016/j.quascirev.2016.07.010

Carcaillet, J., Angel, I., Carrillo, E., Audemard, F. a., Beck, C., 2013. Timing of the last deglaciation in the Sierra Nevada of the Mérida Andes, Venezuela. Quat. Res. 80, 482–494. https://doi.org/10.1016/j.yqres.2013.08.001

Clayton, J.D., Clapperton, C.M., 1997. Broad synchrony of a Late-glacial glacier advance and the highstand of palaeolake Tauca in the Bolivian Altiplano. J. Quat. Sci. 12, 169–182. https://doi.org/10.1002/(SICI)1099-1417(199705/06)12:3<169::AID-JQS304>3.0.CO;2-S

Condom, T., 2002. Dynamiques d'extension lacustre et glaciaire associées aux modifications du climat dans les Andes Centrales. Université Paris VI, France.

Condom, T., Coudrain, A., Dezetter, A., Brunstein, D., Delclaux, F., Jean-Emmanuel, S., 2004. Transient modelling of lacustrine regressions: two case studies from the Andean Altiplano. Hydrol. Process. 18, 2395–2408.

https://doi.org/10.1002/hyp.1470
Condom, T., Coudrain, A., Sicart, J.E., Théry, S., 2007. Computation of the space and time evolution of equilibrium-line altitudes on Andean glaciers (10°N–55°S). Glob. Planet. Change 59, 189–202. https://doi.org/10.1016/j.gloplacha.2006.11.021
Crivellari, S., Chiessi, C.M., Kuhnert, H., Häggi, C., da Costa Portilho-Ramos, R., Zeng, J.-Y., Zhang, Y., Schefuß, E., Mollenhauer, G., Hefter, J., Alexandre, F., Sampaio, G., Mulitza, S., 2018. Increased Amazon freshwater discharge during late Heinrich Stadial 1. Quat. Sci. Rev. 181, 144–155. https://doi.org/10.1016/j.quascirev.2017.12.005
Cruz, F.W., Burns, S.J., Karmann, I., Sharp, W.D., Vuille, M., Cardoso, A.O., Ferrari, J.A., Silva Dias, P.L., Viana, O., 2005. Insolation-driven changes in atmospheric circulation over the past 116,000 years in subtropical Brazil. Nature 434, 63–66. https://doi.org/10.1038/nature03365
Dee, D.P., Uppala, S.M., Simmons, A.J., Berrisford, P., Poli, P., Kobayashi, S., Andrae, U., Balmaseda, M.A., Balsamo, G., Bauer, P., Bechtold, P., Beljaars, A.C.M., van de Berg, L., Bidlot, J., Bormann, N., Delsol, C., Dragani, R., Fuentes, M., Geer, A.J., Haimberger, L., Healy, S.B., Hersbach, H., Hólm, E. V., Isaksen, L., Kållberg, P., Köhler, M., Matricardi, M., McNally, A.P., Monge-Sanz, B.M., Morcrette, J.-J., Park, B.-K., Peubey, C., de Rosnay, P., Tavolato, C., Thépaut, J.-N., Vitart, F., 2011. The ERA-Interim reanalysis: configuration and performance of the data assimilation system. Q. J. R. Meteorol. Soc. 137, 553–597. https://doi.org/10.1002/qj.828
Delunel, R., Blard, P.-H., Martin, L.C.P., Nomade, S., Schlunegger, F., 2016. Long term low latitude and high elevation cosmogenic 3He production rate inferred from a 107ka-old lava flow in northern Chile; 22°S-3400ma.s.l. Geochim. Cosmochim. Acta 184, 71–87. https://doi.org/10.1016/j.gca.2016.04.023
Denton, G.H., Anderson, R.F., Toggweiler, J.R., Edwards, R.L., Schaefer, J.M., Putnam, A.E., 2010. The Last Glacial Termination. Science (80-.). 328, 1652–1656. https://doi.org/10.1126/science.1184119
Eichel, J., Draebing, D., Meyer, N., 2018. From active to stable: Paraglacial transition of Alpine lateral moraine slopes. L. Degrad. Dev. 29, 4158–4172. https://doi.org/10.1002/ldr.3140
Farber, D.L., Hancock, G.S., Finkel, R.C., Rodbell, D.T., 2005. The age and extent of tropical alpine glaciation in the Cordillera Blanca, Peru. J. Quat. Sci. 20, 759–776. https://doi.org/10.1002/jqs.994
Fox, A.N., 1993. Snowline altitude and climate at present and during the Last Pleistocene Glacial Maximum in the Central Andes (5°–28°S). Cornell University.
Fritz, S.C., Baker, P.A., Seltzer, G.O., Ballantyne, A., Tapia, P., Cheng, H., Edwards, R.L., 2007. Quaternary glaciation and hydrologic variation in the South American tropics as reconstructed from the Lake Titicaca drilling project. Quat. Res. 68, 410–420. https://doi.org/10.1016/j.yqres.2007.07.008
Garreaud, R., Vuille, M., Clement, A.C., 2003. The climate of the Altiplano: observed current conditions and mechanisms of past changes. Palaeogeogr. Palaeoclimatol. Palaeoecol. 194, 5–22. https://doi.org/10.1016/S0031-0182(03)00269-4
Garreaud, R.D., Vuille, M., Compagnucci, R., Marengo, J., 2009. Present-day South American climate. Palaeogeogr. Palaeoclimatol. Palaeoecol. 281, 180–195. https://doi.org/10.1016/j.palaeo.2007.10.032
Gayo, E.M., Latorre, C., Jordan, T.E., Nester, P.L., Estay, S.A., Ojeda, K.F., Santoro, C.M., 2012. Late Quaternary hydrological and ecological changes in the hyperarid core of the northern Atacama Desert (~21°S). Earth-Science Rev. 113, 120–140. https://doi.org/10.1016/j.earscirev.2012.04.003
Groot, M.H.M., Bogotá, R.G., Lourens, L.J., Hooghiemstra, H., Vriend, M., Berrio, J.C., Tuenter, E., Van der Plicht, J., Van Geel, B., Ziegler, M., Weber, S.L., Betancourt, A., Contreras, L., Gaviria, S., Giraldo, C., González, N., Jansen, J.H.F., Konert, M., Ortega, D., Rangel, O., Sarmiento, G., Vandenberghe, J., Van der Hammen, T., Van der Linden, M., Westerhoff, W., 2011. Ultra-high resolution pollen record from the northern Andes reveals rapid shifts in montane climates within the last two glacial cycles. Clim. Past 7, 299–316. https://doi.org/10.5194/cp-7-299-2011
Hastenrath, S., 1991. Climate Dynamics of the Tropics. Springer Netherlands, Dordrecht. https://doi.org/10.1007/978-94-011-3156-8
Haug, G.H., 2001. Southward Migration of the Intertropical Convergence Zone Through the Holocene. Science (80-.). 293, 1304–1308. https://doi.org/10.1126/science.1059725
Heyman, J., Stroeven, A.P., Harbor, J.M., Caffee, M.W., 2011. Too young or too old: Evaluating cosmogenic exposure dating based on an analysis of compiled boulder exposure ages. Earth Planet. Sci. Lett. 302, 71–80. https://doi.org/10.1016/j.epsl.2010.11.040
Jackson, M.S., Kelly, M.A., Russell, J.M., Doughty, A.M., Howley, J.A., Chipman, J.W., Cavagnaro, D., Nakileza, B., Zimmerman, S.R.H., 2019. High-latitude warming initiated the onset of the last deglaciation in the tropics. Sci. Adv. 5, eaaw2610. https://doi.org/10.1126/sciadv.aaw2610
Jomelli, V., Favier, V., He, F., Liu, Z., 2016. High altitude temperature changes in the tropical Andes over the last 15000 years estimated from a glaciological model. Glaciers Form. Clim. Chang. their Eff. Nov. Sci. Publ. New York.
Jomelli, V., Favier, V., Vuille, M., Braucher, R., Martin, L., Blard, P.-H.P.-H., Colose, C., Brunstein, D., He, F., Khodri, M., Bourlès, D.L.L., Leanni, L., Rinterknecht, V., Grancher, D., Francou, B., Ceballos, J.L.L., Fonseca, H., Liu, Z., Otto-Bliesner, B.L.L., 2014. A major advance of tropical Andean glaciers during the Antarctic cold reversal. Nature 513, 224–228. https://doi.org/10.1038/nature13546
Jomelli, V., Khodri, M., Favier, V., Brunstein, D., Ledru, M.-P., Wagnon, P., Blard, P.-H., Sicart, J.-E., Braucher, R., Grancher, D., Bourlès, D.L., Braconnot, P., Vuille, M., 2011. Irregular tropical glacier retreat over the Holocene epoch driven by progressive warming. Nature 474, 196–9. https://doi.org/10.1038/nature10150
Jouzel, J., Masson-Delmotte, V., Cattani, O., Dreyfus, G., Falourd, S., Hoffmann, G., Minster, B., Nouet, J., Barnola, J.M., Chappellaz, J., Fischer, H., Gallet, J.C., Johnsen, S., Leuenberger, M., Loulergue, L., Luethi, D., Oerter, H., Parrenin, F., Raisbeck, G., Raynaud, D., Schilt, A., Schwander, J., Selmo, E., Souchez, R., Spahni, R., Stauffer, B., Steffensen, J.P., Stenni, B., Stocker, T.F., Tison, J.L., Werner, M., Wolff, E.W., 2007. Orbital and Millennial Antarctic Climate Variability over the Past 800,000 Years. Science (80-.). 317, 793–796. https://doi.org/10.1126/science.1141038
Kanner, L.C., Burns, S.J., Cheng, H., Edwards, R.L., 2012. High-Latitude Forcing of the South American Summer Monsoon

During the Last Glacial. Science (80-.). 335, 570–573. https://doi.org/10.1126/science.1213397
Kelly, M. a., Lowell, T. V., Applegate, P.J., Phillips, F.M., Schaefer, J.M., Smith, C. a., Kim, H., Leonard, K.C., Hudson, A.M., 2015. A locally calibrated, late glacial 10 Be production rate from a low-latitude, high-altitude site in the Peruvian Andes. Quat. Geochronol. 26, 70–85. https://doi.org/10.1016/j.quageo.2013.10.007
Kuhn, M., 1989. The Response of the Equilibrium Line Altitude to Climate Fluctuations: Theory and Observations, in: Oerlemans, J. (Ed.), . Springer Netherlands, Dordrecht, pp. 407–417. https://doi.org/10.1007/978-94-015-7823-3_26
Kull, C., Grosjean, M., 2000. Late Pleistocene climate conditions in the north Chilean Andes drawn from a climate–glacier model. J. Glaciol. 46, 622–632. https://doi.org/10.3189/172756500781832611
Kull, C., Hänni, F., Grosjean, M., Veit, H., 2003. Evidence of an LGM cooling in NW-Argentina (22°S) derived from a glacier climate model. Quat. Int. 108, 3–11. https://doi.org/10.1016/S1040-6182(02)00190-8
Kull, C., Imhof, S., Grosjean, M., Zech, R., Veit, H., 2008. Late Pleistocene glaciation in the Central Andes: Temperature versus humidity control — A case study from the eastern Bolivian Andes (17°S) and regional synthesis. Glob. Planet. Change 60, 148–164. https://doi.org/10.1016/j.gloplacha.2007.03.011
Lal, D., 1991. Cosmic ray labeling of erosion surfaces: in situ nuclide production rates and erosion models. Earth Planet. Sci. Lett. 104, 424–439. https://doi.org/10.1016/0012-821X(91)90220-C
Leclercq, P.W., Oerlemans, J., Basagic, H.J., Bushueva, I., Cook, A.J., Le Bris, R., 2014. A data set of worldwide glacier length fluctuations. Cryosph. 8, 659–672. https://doi.org/10.5194/tc-8-659-2014
Lenters, J.D., Cook, K.H., 1999. Summertime Precipitation Variability over South America: Role of the Large-Scale Circulation. Mon. Weather Rev. 127, 409–431. https://doi.org/10.1175/1520-0493(1999)127<0409:SPVOSA>2.0.CO;2
Licciardi, J.M., Schaefer, J.M., Taggart, J.R., Lund, D.C., 2009. Holocene glacier fluctuations in the Peruvian Andes indicate northern climate linkages. Science 325, 1677–9. https://doi.org/10.1126/science.1175010
Lifton, N., 2016. Implications of two Holocene time-dependent geomagnetic models for cosmogenic nuclide production rate scaling. Earth Planet. Sci. Lett. 433, 257–268. https://doi.org/10.1016/j.epsl.2015.11.006
Lifton, N., Sato, T., Dunai, T.J., 2014. Scaling in situ cosmogenic nuclide production rates using analytical approximations to atmospheric cosmic-ray fluxes. Earth Planet. Sci. Lett. 386, 149–160. https://doi.org/10.1016/j.epsl.2013.10.052
Loibl, D., Lehmkuhl, F., Grießinger, J., 2014. Reconstructing glacier retreat since the Little Ice Age in SE Tibet by glacier mapping and equilibrium line altitude calculation. Geomorphology 214, 22–39. https://doi.org/10.1016/j.geomorph.2014.03.018
Mabry, J., Burnard, P., Blard, P.-H., Zimmermann, L., 2012. Mapping changes in helium sensitivity and peak shape for varying parameters of a Nier-type noble gas ion source. J. Anal. At. Spectrom. 27, 1012. https://doi.org/10.1039/c2ja10339g
Malone, A.G.O., Pierrehumbert, R.T., Lowell, T. V., Kelly, M.A., Stroup, J.S., 2015. Constraints on southern hemisphere tropical climate change during the Little Ice Age and Younger Dryas based on glacier modeling of the Quelccaya Ice Cap, Peru. Quat. Sci. Rev. 125, 106–116. https://doi.org/10.1016/j.quascirev.2015.08.001
Martin, L.C.P., Blard, P.-H., Balco, G., Lavé, J., Delunel, R., Lifton, N., Laurent, V., 2017. The CREp program and the ICE-D production rate calibration database: A fully parameterizable and updated online tool to compute cosmic-ray exposure ages. Quat. Geochronol. 38, 25–49. https://doi.org/10.1016/j.quageo.2016.11.006
Martin, L.C.P., Blard, P.-H., Lavé, J., Braucher, R., Lupker, M., Condom, T., Charreau, J., Mariotti, V., ASTER Team, Davy, E., 2015. In situ cosmogenic 10Be production rate in the High Tropical Andes. Quat. Geochronol. 30, 54–68. https://doi.org/10.1016/j.quageo.2015.06.012
Martin, L.C.P., Blard, P.-H., Lavé, J., Condom, T., Prémaillon, M., Jomelli, V., Brunstein, D., Lupker, M., Charreau, J., Mariotti, V., Tibari, B., Davy, E., 2018. Lake Tauca highstand (Heinrich Stadial 1a) driven by a southward shift of the Bolivian High. Sci. Adv. 4, eaar2514. https://doi.org/10.1126/sciadv.aar2514
Matsuda, J., Matsumoto, T., Sumino, H., Nagao, K., Yamamoto, J., Miura, Y., Kaneoka, I., Takahata, N., Sano, Y., 2002. The 3He/4He ratio of the new internal He Standard of Japan (HESJ). Geochem. J. 36, 191–195. https://doi.org/10.2343/geochemj.36.191
McManus, J.F., Francois, R., Gherardi, J.-M., Keigwin, L.D., Brown-Leger, S., 2004. Collapse and rapid resumption of Atlantic meridional circulation linked to deglacial climate changes. Nature 428, 834–837. https://doi.org/10.1038/nature02494
Meierding, T.C., 1982. Late Pleistocene Glacial Equilibrium-Line Front Range: A Comparison Altitudes in the Colorado of Methods. Quat. Res. 18, 289–310. https://doi.org/https://doi.org/10.1016/0033-5894(82)90076-X
Muscheler, R., Beer, J., Kubik, P.W., Synal, H. -a., 2005. Geomagnetic field intensity during the last 60,000 years based on 10Be and 36Cl from the Summit ice cores and 14C. Quat. Sci. Rev. 24, 1849–1860. https://doi.org/10.1016/j.quascirev.2005.01.012
New, M., Lister, D., Hulme, M., Makin, I., 2002. A high-resolution data set of surface climate over global land areas. Clim. Res. 21, 1–25. https://doi.org/10.3354/cr021001
Nishiizumi, K., Imamura, M., Caffee, M.W., Southon, J.R., Finkel, R.C., McAninch, J., 2007. Absolute calibration of 10Be AMS standards. Nucl. Instruments Methods Phys. Res. Sect. B Beam Interact. with Mater. Atoms 258, 403–413. https://doi.org/10.1016/j.nimb.2007.01.297
Nunnery, J.A., Fritz, S.C., Baker, P.A., Salenbien, W., 2019. Lake-level variability in Salar de Coipasa, Bolivia during the past ~40,000 yr. Quat. Res. 91, 881–891. https://doi.org/10.1017/qua.2018.108
Ohmura, A., Kasser, P., Funk, M., 1992. Climate at the Equilibrium Line of Glaciers. J. Glaciol. 38, 397–411. https://doi.org/10.3189/S0022143000002276
Osmaston, H., 2005. Estimates of glacier equilibrium line altitudes by the Area×Altitude, the Area×Altitude Balance Ratio and the Area×Altitude Balance Index methods and their validation. Quat. Int. 138–139, 22–31. https://doi.org/10.1016/j.quaint.2005.02.004

Palacios, D., Stokes, C.R., Phillips, F.M., Clague, J.J., Alcalá-Reygosa, J., Andres, N., Angel, I., Blard, P.-H., Briner, J.P., Hall, B.L., Dahms, D., Hein, A.S., Jomelli, V., Mark, B.G., Martini, M.A., Moreno, P., Riedel, J., Sagredo, E., Stansell, N.D., Vazquez-Selem, L., Vuille, M., Ward, D.J., 2020. The deglaciation of the Americas during the Last Glacial Termination. Earth-Science Rev. 103113. https://doi.org/10.1016/j.earscirev.2020.103113

Parnell, A.C., Buck, C.E., Doan, T.K., 2011. A review of statistical chronology models for high-resolution, proxy-based Holocene palaeoenvironmental reconstruction. Quat. Sci. Rev. 30, 2948–2960. https://doi.org/10.1016/j.quascirev.2011.07.024

Peterson, L.C., 2000. Rapid Changes in the Hydrologic Cycle of the Tropical Atlantic During the Last Glacial. Science (80-.). 290, 1947–1951. https://doi.org/10.1126/science.290.5498.1947

Placzek, C., Quade, J., Patchett, P.J., 2006. Geochronology and stratigraphy of late Pleistocene lake cycles on the southern Bolivian Altiplano: Implications for causes of tropical climate change. Geol. Soc. Am. Bull. 118, 515–532. https://doi.org/10.1130/B25770.1

Placzek, C.J., Quade, J., Patchett, P.J., 2013. A 130ka reconstruction of rainfall on the Bolivian Altiplano. Earth Planet. Sci. Lett. 363, 97–108. https://doi.org/10.1016/j.epsl.2012.12.017

Porter, S.C., 2000. Snowline depression in the tropics during the Last Glaciation. Quat. Sci. Rev. 20, 1067–1091. https://doi.org/10.1016/S0277-3791(00)00178-5

Quesada, B., Sylvestre, F., Vimeux, F., Black, J., Paillès, C., Sonzogni, C., Alexandre, A., Blard, P.-H., Tonetto, A., Mazur, J.-C., Bruneton, H., 2015. Impact of Bolivian paleolake evaporation on the δ18O of the Andean glaciers during the last deglaciation (18.5–11.7 ka): diatom-inferred δ18O values and hydro-isotopic modeling. Quat. Sci. Rev. 120, 93–106. https://doi.org/10.1016/j.quascirev.2015.04.022

Rabatel, A., Francou, B., Soruco, A., Gomez, J., Cáceres, B., Ceballos, J.L., Basantes, R., Vuille, M., Sicart, J.-E., Huggel, C., Scheel, M., Lejeune, Y., Arnaud, Y., Collet, M., Condom, T., Consoli, G., Favier, V., Jomelli, V., Galarraga, R., Ginot, P., Maisincho, L., Mendoza, J., Ménégoz, M., Ramirez, E., Ribstein, P., Suarez, W., Villacis, M., Wagnon, P., 2013. Current state of glaciers in the tropical Andes: a multi-century perspective on glacier evolution and climate change. Cryosph. 7, 81–102. https://doi.org/10.5194/tc-7-81-2013

Ramirez, E., Hoffmann, G., Taupin, J.., Francou, B., Ribstein, P., Caillon, N., Ferron, F.., Landais, A., Petit, J.., Pouyaud, B., Schotterer, U., Simoes, J.., Stievenard, M., 2003. A new Andean deep ice core from Nevado Illimani (6350 m), Bolivia. Earth Planet. Sci. Lett. 212, 337–350. https://doi.org/10.1016/S0012-821X(03)00240-1

Ramsey, C.B., 2009. BAYESIAN ANALYSIS OF RADIOCARBON DATES Christopher Bronk Ramsey. Radiocarbon 51, 337–360. https://doi.org/10.2458/azu_js_rc.v51i1.3494

Reimer, P., 2013. IntCal13 and Marine13 Radiocarbon Age Calibration Curves 0–50,000 Years cal BP. Radiocarbon 55, 1869–1887. https://doi.org/10.2458/azu_js_rc.55.16947

Roe, G.H., Lindzen, R.S., 2001. A one-dimensional model for the interaction between continental-scale ice sheets and atmospheric stationary waves. Clim. Dyn. 17, 479–487. https://doi.org/10.1007/s003820000123

Sagredo, E.A., Lowell, T.V., 2012. Climatology of Andean glaciers: A framework to understand glacier response to climate change. Glob. Planet. Change 86–87, 101–109. https://doi.org/10.1016/j.gloplacha.2012.02.010

Satgé, F., Espinoza, R., Zolá, R., Roig, H., Timouk, F., Molina, J., Garnier, J., Calmant, S., Seyler, F., Bonnet, M.-P., 2017. Role of Climate Variability and Human Activity on Poopó Lake Droughts between 1990 and 2015 Assessed Using Remote Sensing Data. Remote Sens. 9, 218. https://doi.org/10.3390/rs9030218

Schimmelpfennig, I., Benedetti, L., Finkel, R., Pik, R., Blard, P.-H., Bourlès, D., Burnard, P., Williams, A., 2009. Sources of in-situ 36Cl in basaltic rocks. Implications for calibration of production rates. Quat. Geochronol. 4, 441–461. https://doi.org/10.1016/j.quageo.2009.06.003

Schimmelpfennig, I., Williams, A., Pik, R., Burnard, P., Niedermann, S., Finkel, R., Schneider, B., Benedetti, L., 2011. Inter-comparison of cosmogenic in-situ 3He, 21Ne and 36Cl at low latitude along an altitude transect on the SE slope of Kilimanjaro volcano (3??S, Tanzania). Quat. Geochronol. 6, 425–436. https://doi.org/10.1016/j.quageo.2011.05.002

Schneider, C., Glaser, M., Kilian, R., Santana, A., Butorovic, N., Casassa, G., 2003. Weather Observations Across the Southern Andes at 53°S. Phys. Geogr. 24, 97–119. https://doi.org/10.2747/0272-3646.24.2.97

Segura, H., Junquas, C., Espinoza, J.C., Vuille, M., Jauregui, Y.R., Rabatel, A., Condom, T., Lebel, T., 2019. New insights into the rainfall variability in the tropical Andes on seasonal and interannual time scales. Clim. Dyn. 53, 405–426. https://doi.org/10.1007/s00382-018-4590-8

Seltzer, G.O., 1994. Climatic Interpretation of Alpine Snowline Variations on Millennial Time Scales. Quat. Res. 41, 154–159. https://doi.org/10.1006/qres.1994.1017

Shakun, J.D., Clark, P.U., Marcott, S.A., Brook, E.J., Lifton, N.A., Caffee, M., Shakun, W.R., 2015. Cosmogenic dating of Late Pleistocene glaciation, southern tropical Andes, Peru. J. Quat. Sci. 30, 841–847. https://doi.org/10.1002/jqs.2822

Sicart, J.E., Hock, R., Six, D., 2008. Glacier melt, air temperature, and energy balance in different climates: The Bolivian Tropics, the French Alps, and northern Sweden. J. Geophys. Res. 113, D24113. https://doi.org/10.1029/2008JD010406

Sissons, J.B., Sutherland, D.G., 1976. Climatic Inferences from Former Glaciers in the South-East Grampian Highlands, Scotland. J. Glaciol. 17, 325–346. https://doi.org/10.1017/S0022143000013617

Smith, C.A., Lowell, T. V., Caffee, M.W., 2009. Lateglacial and Holocene cosmogenic surface exposure age glacial chronology and geomorphological evidence for the presence of cold-based glaciers at Nevado Sajama, Bolivia. J. Quat. Sci. 24, 360–372. https://doi.org/10.1002/jqs.1239

Smith, J.A., Seltzer, G.O., Farber, D.L., Rodbell, D.T., Finkel, R.C., 2005. Early Local Last Glacial Maximum in the Tropical Andes. Science (80-.). 308, 678–681. https://doi.org/10.1126/science.1107075

Soruco, A., Vincent, C., Francou, B., Ribstein, P., Berger, T., Sicart, J.E., Wagnon, P., Arnaud, Y., Favier, V., Lejeune, Y., 2009. Mass balance of Glaciar Zongo, Bolivia, between 1956 and 2006, using glaciological, hydrological and geodetic methods. Ann. Glaciol. 50, 1–8. https://doi.org/10.3189/172756409787769799

Stauch, G., Lehmkuhl, F., 2010. Quaternary glaciations in the Verkhoyansk Mountains, Northeast Siberia. Quat. Res. 74,

145–155. https://doi.org/10.1016/j.yqres.2010.04.003
Stone, J.O., 2000. Air pressure and cosmogenic isotope production. J. Geophys. Res. Solid Earth 105, 23753–23759. https://doi.org/10.1029/2000JB900181
Stríkis, N.M., Chiessi, C.M., Cruz, F.W., Vuille, M., Cheng, H., de Souza Barreto, E.A., Mollenhauer, G., Kasten, S., Karmann, I., Edwards, R.L., Bernal, J.P., Sales, H. dos R., 2015. Timing and structure of Mega-SACZ events during Heinrich Stadial 1. Geophys. Res. Lett. 42, 5477-5484A. https://doi.org/10.1002/2015GL064048
Sylvestre, F., Servant, M., Servant-Vildary, S., Causse, C., Fournier, M., Ybert, J.-P., 1999. Lake-Level Chronology on the Southern Bolivian Altiplano (18°–23°S) During Late-Glacial Time and the Early Holocene. Quat. Res. 51, 54–66. https://doi.org/10.1006/qres.1998.2017
Thompson, L.G., Davis, M.E., Mosley-Thompson, E., Sowers, T.A., Henderson, K.A., Zagorodnov, V.S., Lin, P., Mikhalenko, V.N., Campen, R.K., Bolzan, J.F., Cole-Dai, J., Francou, B., 1998. A 25,000-Year Tropical Climate History from Bolivian Ice Cores. Science (80-.). 282, 1858–1864. https://doi.org/10.1126/science.282.5395.1858
Thompson, L.G., Mosley-Thompson, E., Davis, M.E., Lin, P.N., Henderson, K.A., Cole-Dai, J., Bolzan, J.F., Liu, K.B., 1995. Late Glacial Stage and Holocene Tropical Ice Core Records from Huascaran, Peru. Science (80-.). 269, 46–50. https://doi.org/10.1126/science.269.5220.46
Toggweiler, J.R., 2009. Climate change: Shifting Westerlies. Science (80-.). 323, 1434–1435. https://doi.org/10.1126/science.1169823
Toggweiler, J.R., Russell, J.L., Carson, S.R., 2006. Midlatitude westerlies, atmospheric CO 2 , and climate change during the ice ages. Paleoceanography 21, n/a-n/a. https://doi.org/10.1029/2005PA001154
Uppala, S.M., KÅllberg, P.W., Simmons, a. J., Andrae, U., Bechtold, V.D.C., Fiorino, M., Gibson, J.K., Haseler, J., Hernandez, A., Kelly, G. a., Li, X., Onogi, K., Saarinen, S., Sokka, N., Allan, R.P., Andersson, E., Arpe, K., Balmaseda, M. a., Beljaars, a. C.M., Berg, L. Van De, Bidlot, J., Bormann, N., Caires, S., Chevallier, F., Dethof, A., Dragosavac, M., Fisher, M., Fuentes, M., Hagemann, S., Hólm, E., Hoskins, B.J., Isaksen, L., Janssen, P. a. E.M., Jenne, R., Mcnally, a. P., Mahfouf, J.-F., Morcrette, J.-J., Rayner, N. a., Saunders, R.W., Simon, P., Sterl, A., Trenberth, K.E., Untch, A., Vasiljevic, D., Viterbo, P., Woollen, J., 2005. The ERA-40 re-analysis. Q. J. R. Meteorol. Soc. 131, 2961–3012. https://doi.org/10.1256/qj.04.176
Vera, C., Higgins, W., Amador, J., Ambrizzi, T., Garreaud, R., Gochis, D., Gutzler, D., Lettenmaier, D., Marengo, J., Mechoso, C.R., Nogues-Paegle, J., Dias, P.L.S., Zhang, C., 2006. Toward a Unified View of the American Monsoon Systems. J. Clim. 19, 4977–5000. https://doi.org/10.1175/JCLI3896.1
Vuille, M., 1999. Atmospheric circulation over the Bolivian Altiplano during dry and wet periods and extreme phases of the Southern Oscillation. Int. J. Climatol. 19, 1579–1600. https://doi.org/10.1002/(SICI)1097-0088(19991130)19:14<1579::AID-JOC441>3.0.CO;2-N
Vuille, M., Francou, B., Wagnon, P., Juen, I., Kaser, G., Mark, B.G., Bradley, R.S., 2008. Climate change and tropical Andean glaciers: Past, present and future. Earth-Science Rev. 89, 79–96. https://doi.org/10.1016/j.earscirev.2008.04.002
Vuille, M., Keimig, F., 2004. Interannual Variability of Summertime Convective Cloudiness and Precipitation in the Central Andes Derived from ISCCP-B3 Data. J. Clim. 17, 3334–3348. https://doi.org/10.1175/1520-0442(2004)017<3334:IVOSCC>2.0.CO;2
Wang, X., Auler, A.S., Edwards, R.L., Cheng, H., Ito, E., Wang, Y., Kong, X., Solheid, M., 2007. Millennial-scale precipitation changes in southern Brazil over the past 90,000 years. Geophys. Res. Lett. 34, 1–5. https://doi.org/10.1029/2007GL031149
Ward, D.J., Cesta, J.M., Galewsky, J., Sagredo, E., 2015. Late Pleistocene glaciations of the arid subtropical Andes and new results from the Chajnantor Plateau, northern Chile. Quat. Sci. Rev. 128, 98–116. https://doi.org/10.1016/j.quascirev.2015.09.022
Xu, C.-Y., Singh, V.P., 2000. Evaluation and generalization of radiation-based methods for calculating evaporation. Hydrol. Process. 14, 339–349. https://doi.org/10.1002/(SICI)1099-1085(20000215)14:2<339::AID-HYP928>3.0.CO;2-O
Zech, J., Zech, R., Kubik, P.W., Veit, H., 2009. Glacier and climate reconstruction at Tres Lagunas, NW Argentina, based on 10Be surface exposure dating and lake sediment analyses. Palaeogeogr. Palaeoclimatol. Palaeoecol. 284, 180–190. https://doi.org/10.1016/j.palaeo.2009.09.023
Zhang, X., Lohmann, G., Knorr, G., Purcell, C., 2014. Abrupt glacial climate shifts controlled by ice sheet changes. Nature 512, 290–294. https://doi.org/10.1038/nature13592
Zhou, J., Lau, K.-M., 1998. Does a Monsoon Climate Exist over South America? J. Clim. 11, 1020–1040. https://doi.org/10.1175/1520-0442(1998)011<1020:DAMCEO>2.0.CO;2
Zimmermann, L., Blard, P.H., Burnard, P., Medynski, S., Pik, R., Puchol, N., 2012. A New Single Vacuum Furnace Design for Cosmogenic 3He Dating. Geostand. Geoanalytical Res. 36, 121–129. https://doi.org/10.1111/j.1751-908X.2011.00145.x

Supplementary Information

S.1. Additional ^{10}Be data for Zongo Valley

Moraine	Sample	Latitude	Longitude	Altitude	^{10}Be (1σ)	Thickness	Thick. Corr.[a]	Shielding[b]	Scaling Factor[c]	Age (1σ)[d]
		Dec°	*Dec°*	*masl*	*10^5 at.g^{-1}*	*cm*	-	-	-	*ka*
T1	B1	-16.2601	-68.1132	4529	4.87 ± 0.42	4	0.97	0.99	10.0	**12.5 ± 1.1**
	B2	-16.2610	-68.1123	4609	5.02 ± 0.43	4	0.97	0.98	10.4	**12.5 ± 1.1**
	B3	-16.2580	-68.1136	4434	3.49 ± 0.20	3	0.98	0.96	9.4	**9.7 ± 0.6**
	B4	-16.2611	-68.1123	4698	3.36 ± 0.34	3	0.98	0.99	10.5	**8.2 ± 0.8**
T2	B5	-16.2606	-68.1121	4581	3.32 ± 0.18	4	0.97	0.97	10.0	**8.7 ± 0.5**
	B6	-16.2586	-68.1136	4475	4.74 ± 0.19	4	0.97	0.98	9.8	**12.6 ± 0.6**
	B7	-16.2597	-68.1118	4536	4.46 ± 0.27	3	0.97	0.98	10.0	**11.5 ± 0.7**
	B8	-16.2605	-68.1119	4580	4.23 ± 0.14	4	0.97	0.98	10.1	**10.9 ± 0.4**
	B9	-16.2574	-68.1098	4605	3.94 ± 0.43	4	0.97	0.98	10.2	**10.1 ± 1.0**
	B10	-16.2605	-68.1118	4575	3.85 ± 0.48	4	0.97	0.99	10.0	**9.9 ± 1.2**
	B11	-16.2578	-68.1122	4503	3.29 ± 0.45	4	0.97	0.94	9.7	**9.2 ± 1.2**
	B12	-16.2599	-68.1121	4534	4.25 ± 0.12	4	0.97	1.00	9.9	**10.9 ± 0.4**
	B13	-16.2576	-68.1110	4559	0.60 ± 0.35	4	0.96	0.97	9.1	**1.7 ± 1.0**
	B14	-16.2573	-68.1093	4624	2.92 ± 0.79	4	0.96	0.97	10.1	**7.7 ± 1.8**
	B15	-16.2597	-68.1119	4479	4.41 ± 0.13	3	0.97	0.98	9.8	**11.6 ± 0.4**
	B16	-16.2575	-68.1093	4619	4.52 ± 0.21	4	0.97	0.99	10.4	**11.2 ± 0.5**
	B17	-16.2601	-68.1109	4601	4.38 ± 0.12	4	0.97	0.98	10.3	**11.1 ± 0.4**
	B18	-16.2601	-68.1109	4553	4.27 ± 0.64	4	0.97	0.98	10.0	**11.1 ± 1.5**
	B19	-16.2601	-68.1115	4553	4.37 ± 0.24	4	0.97	0.98	10.1	**11.3 ± 0.6**
	B20	-16.2601	-68.1109	4584	4.44 ± 0.14	3	0.97	0.98	10.2	**11.3 ± 0.4**
	B21	-16.2580	-68.1097	4579	4.05 ± 0.15	4	0.96	0.98	10.1	**10.4 ± 0.4**
	B22	-16.2602	-68.1105	4540	4.59 ± 0.13	3	0.97	0.98	10.1	**11.8 ± 0.4**
	B23	-16.2600	-68.1102	4561	3.89 ± 0.19	4	0.97	0.97	10.0	**10.2 ± 0.5**
	B24	-16.2602	-68.1101	4562	3.84 ± 0.34	4	0.96	0.98	10.0	**10.1 ± 0.9**
	B25	-16.2578	-68.1090	4608	4.02 ± 0.29	4	0.96	0.99	10.2	**10.2 ± 0.7**
	B26	-16.2601	-68.1099	4547	4.45 ± 0.10	4	0.97	0.98	10.1	**11.5 ± 0.3**
	B27	-16.2578	-68.1086	4619	4.03 ± 0.51	4	0.97	0.98	10.2	**10.2 ± 1.2**
	B28	-16.2594	-68.1097	4562	3.52 ± 0.40	4	0.97	0.97	9.9	**9.2 ± 1.0**
	B29	-16.2594	-68.1097	4562	3.48 ± 0.25	3	0.97	0.97	9.9	**9.1 ± 0.7**
	B30	-16.2576	-68.1084	4630	4.53 ± 0.21	4	0.96	0.98	10.4	**11.3 ± 0.5**
	B31	-16.2606	-68.1081	4605	3.53 ± 0.45	4	0.97	0.98	10.1	**9.1 ± 1.1**
	B32	-16.2593	-68.1092	4551	4.31 ± 0.16	4	0.97	0.98	10.0	**11.1 ± 0.4**
	B33	-16.2599	-68.1090	4548	4.14 ± 0.49	4	0.97	0.98	10.0	**10.7 ± 1.2**
T3	B34	-16.2599	-68.1090	4548	4.58 ± 0.34	4	0.97	0.98	10.1	**11.7 ± 0.8**
	B35	-16.2575	-68.1076	4632	3.86 ± 0.40	4	0.97	0.98	10.3	**9.8 ± 1.0**
	B36	-16.2594	-68.1124	4706	4.16 ± 0.16	4	0.97	0.97	10.6	**10.3 ± 0.4**
	B37	-16.2598	-68.1071	4612	3.23 ± 0.24	4	0.97	0.98	10.1	**8.3 ± 0.6**
	B38	-16.2597	-68.1069	4640	3.65 ± 0.20	3	0.98	0.98	10.3	**9.2 ± 0.5**
	B39	-16.2596	-68.1070	4734	4.16 ± 0.15	3	0.98	0.98	10.7	**10.0 ± 0.4**
	B40	-16.2594	-68.1070	4642	3.92 ± 0.15	3	0.98	0.98	10.3	**9.8 ± 0.4**
	B41	-16.2598	-68.1068	4639	3.59 ± 0.35	3	0.98	0.99	10.2	**9.0 ± 0.8**
	B42	-16.2579	-68.1064	4630	3.97 ± 0.15	3	0.97	0.97	10.3	**10.1 ± 0.4**
	B43	-16.2592	-68.1069	4642	4.08 ± 0.15	3	0.98	0.98	10.3	**10.2 ± 0.4**
	B44	-16.2600	-68.1061	4647	4.02 ± 0.17	3	0.98	0.99	10.3	**10.0 ± 0.5**
	B45	-16.2592	-68.1069	4641	4.42 ± 0.15	3	0.98	0.98	10.4	**10.9 ± 0.4**
	B46	-16.2591	-68.1066	4607	2.75 ± 0.20	4	0.97	0.98	9.9	**7.2 ± 0.5**
	B47	-16.2574	-68.1061	4646	3.95 ± 0.39	4	0.97	0.98	10.3	**9.9 ± 0.9**
	B48	-16.2577	-68.1060	4640	4.08 ± 0.42	3	0.97	0.98	10.3	**10.2 ± 1.0**
	B49	-16.2577	-68.1060	4641	4.17 ± 0.27	4	0.97	0.97	10.4	**10.6 ± 0.7**
	B50	-16.2595	-68.1054	4648	3.65 ± 0.20	3	0.98	0.97	10.3	**9.2 ± 0.5**
	B51	-16.2599	-68.1050	4655	3.78 ± 0.13	3	0.98	0.98	10.3	**9.4 ± 0.4**
	B52	-16.2592	-68.1054	4652	4.04 ± 0.14	3	0.98	0.97	10.4	**10.1 ± 0.4**
	B53	-16.2594	-68.1044	4668	3.63 ± 0.13	3	0.98	0.98	10.4	**9.0 ± 0.4**
	B54	-16.2586	-68.1047	4671	4.24 ± 0.15	3	0.98	0.99	10.5	**10.3 ± 0.4**
	B55	-16.2592	-68.1045	4667	4.24 ± 0.15	3	0.98	0.98	10.5	**10.4 ± 0.4**
	B56	-16.2586	-68.1048	4669	4.34 ± 0.15	3	0.98	0.99	10.5	**10.6 ± 0.4**
	B57	-16.2594	-68.1041	4666	4.33 ± 0.15	3	0.98	0.97	10.5	**10.7 ± 0.4**
	B58	-16.2571	-68.1016	4703	0.31 ± 0.04	3	0.98	0.99	10.0	**0.8 ± 0.1**
	B59	-16.2572	-68.1016	4734	0.09 ± 0.01	3	0.98	0.98	10.8	**0.20 ± 0.03**

[a] Calculated with a density of 2.7 g.cm^{-3} and an attenuation length of 160 g.cm^{-2}

[b] Calculated using the CRONUS shielding application

[c] Global scaling factor that accounts for the geomagnetic correction

[d] PR: weighted mean of Kelly et al. (2013), Blard et al. (2013b) and Martin et al. (2015) - Scaling: Lal modified - Atmosphere: ERA40 - VDM: Muscheler et al. (2005)

Table S1a. Recalculated ages for Cerro Telata, Zongo Valley, from the data of Jomelli et al. (2011).

Moraine	Sample	Mass of quartz	Measured $^{10}Be/^{9}Be$[a]	^{10}Be counts	Blank $^{10}Be/^{9}Be$[b]	^{9}Be carrier	$^{10}Be \pm 1\sigma$[c]
		g	-	-	-	*at*	10^{5} *at.g*$^{-1}$
MV	MB9	3.74	1.00E-13	187	2.68E-15	2.06E+19	5.38 ± 0.29
	MB10	12.36	3.11E-13	1224	2.68E-15	2.07E+19	5.16 ± 0.16
	MB11	6.44	1.39E-13	1012	2.68E-15	2.07E+19	4.38 ± 0.16
	MB12	1.99	7.79E-14	618	2.68E-15	2.07E+19	7.82 ± 0.38
	MB13	2.14	4.23E-14	344	2.68E-15	2.04E+19	3.79 ± 0.24
	MB14	6.28	1.60E-13	170	2.68E-15	2.06E+19	5.16 ± 0.26
	Zong-13-01	12.13	8.78E-14	965	1.46E-15	4.18E+19	2.97 ± 0.11
	Zong-13-02	11.03	7.79E-14	887	1.46E-15	4.19E+19	2.90 ± 0.11
	Zong-13-03	10.93	5.58E-14	564	1.46E-15	4.18E+19	2.08 ± 0.10
	Zong-13-04	7.92	6.64E-14	799	1.46E-15	4.18E+19	3.43 ± 0.15
CQ1	CNB1	3.96	9.89E-14	308	2.68E-15	2.05E+19	4.99 ± 0.31
	CNB2	7.84	1.82E-13	1215	2.68E-15	2.07E+19	4.74 ± 0.16
	CNB3	7.49	1.79E-13	1230	2.68E-15	2.06E+19	4.85 ± 0.16
	CNB4	14.08	3.15E-13	696	2.68E-15	2.05E+19	4.56 ± 0.19
	CNB5	6.80	1.61E-13	804	2.68E-15	2.04E+19	4.76 ± 0.19
CQ3	CNB16	13.10	2.38E-13	1110	3.89E-15	2.11E+19	3.77 ± 0.13
	CNB17	22.38	4.49E-13	1155	3.89E-15	2.08E+19	4.15 ± 0.15
	CNB18	8.60	1.68E-13	1218	3.89E-15	2.11E+19	4.03 ± 0.13
	CNB19	7.37	1.48E-13	364	3.89E-15	2.10E+19	4.11 ± 0.25
	CNB20	15.86	2.84E-13	779	3.89E-15	2.10E+19	3.71 ± 0.14
CQ4	CNB11	19.32	3.64E-13	1240	3.89E-15	2.11E+19	3.94 ± 0.13
	CNB13	9.43	1.80E-13	797	3.89E-15	2.12E+19	3.96 ± 0.17
	CNB15	11.05	2.06E-13	1212	3.89E-15	2.11E+19	3.88 ± 0.13

[a] $^{10}Be/^{9}Be$ ratios were analyzed at the ASTER AMS facility and normalized to the $^{10}Be/^{9}Be$ ratio of the SRM 4325 NIST material: $(2.79\pm0.03) \times 10^{-11}$ (Nishiizumi et al., 2017).

[b] Ratio are averages from 4 to 6 blanks for MV and CQ1. The ratio for CQ3 and 4 is based on 1 blank. All blanks were realized during the same session as the samples.

[c] Uncertainties are propagated taking into account counting statistics and errors from blank measurements.

Table S1b. Raw ^{10}Be and ^{9}Be data of the new samples at Zongo Valley.

S.2. Hydrologic connection between the Altiplano sub-basins

We used the shoreline archive to provide hydrological constraints on our climatic inversions based the on hydrologic budget of the southern basin lake at a given level. Because the hydrologic connection between the four basins of the Altiplano during the late-glacial period has not been proven, computing the relevant hydrologic budget required that we determine which basins were connected to the southern basin for a given set of ΔT and ΔP values (relative to present-day values).

We computed the hydrological balance of each sub-basin watershed balance sequentially to evaluate the connection between each basin and its downstream counterpart(s). First, we computed the Titicaca overflow toward the Poopo basin, then the annual hydrologic budgets for the Poopo basin, allowing lake-level adjustments from one year to another until reaching a steady state. If this steady state corresponds to an overflow towards the Coipasa basin, we determine the corresponding input for the Coipasa. We applied the same approach to the Coipasa basin to see if it overflows into the Uyuni basin. We thusly identified the basins hydrologically connected with the southern basin, for which we know the lake level from shoreline ages. We finally computed the hydrological budget for the identified basins and solved for ΔT and ΔP.

S.3. Calculation of the lake-induced precipitation anomaly, computation of the *A* grids

The initial steps of this calculation are presented in Section 3.3.5. Within each sector, the punctual $A_{\text{Tauca}}(x, y)$ value was associated to its normalized distance r^*_S to the barycenter, taken as the actual distance divided by the sector's lake radius. From these values, a scatter plot of $A_{\text{Tauca}} = f(r^*_S)$ was constructed for each sector, and a curve averaging the point cloud was constructed. Thus, for the Tauca highstand, we produced a set of 20 curves describing the radial evolution of the anomaly from the barycenter of Lake Tauca along the normalized distance r^*_S. Because each of these curves averages this behavior over a given angular sector, we associated each $A(r^*_S)$ curve with θ_S, the angle (in radians) between the bisector of sector S and a reference vector (due south).

Then, for any time t of the last deglaciation, we proceeded as follows. We first derived the lake level from the shoreline dataset. We then derived the lake extent from this elevation and the DEM of the basin, and calculated its barycenter. From the barycenter, we divided the basin into 20 angular sectors and calculated the mean lake radius per sector (see Section 3.3.5). We then calculated r^*_i and θ_i for each point i in the sector. We then used the set of 20 $A(r^*_S)$ curves in θ_S-r^*_S space to perform a 2D polar interpolation of the values of A in θ_i-r^*_i space. We were thus able to calculate the grid A for any lake configuration of the study period. This algorithm was implemented such that during the Tauca highstand, the anomaly algorithm was bypassed and the grid A input into the lake model was the original grid directly derived from the results of Martin et al. (2018). The reconstructed anomaly fields (given as $\beta \times A$) for the Coipasa and Tauca highstands are shown in Figure 10, and a graphical illustration of the anomaly algorithm is provided in Figure S3.

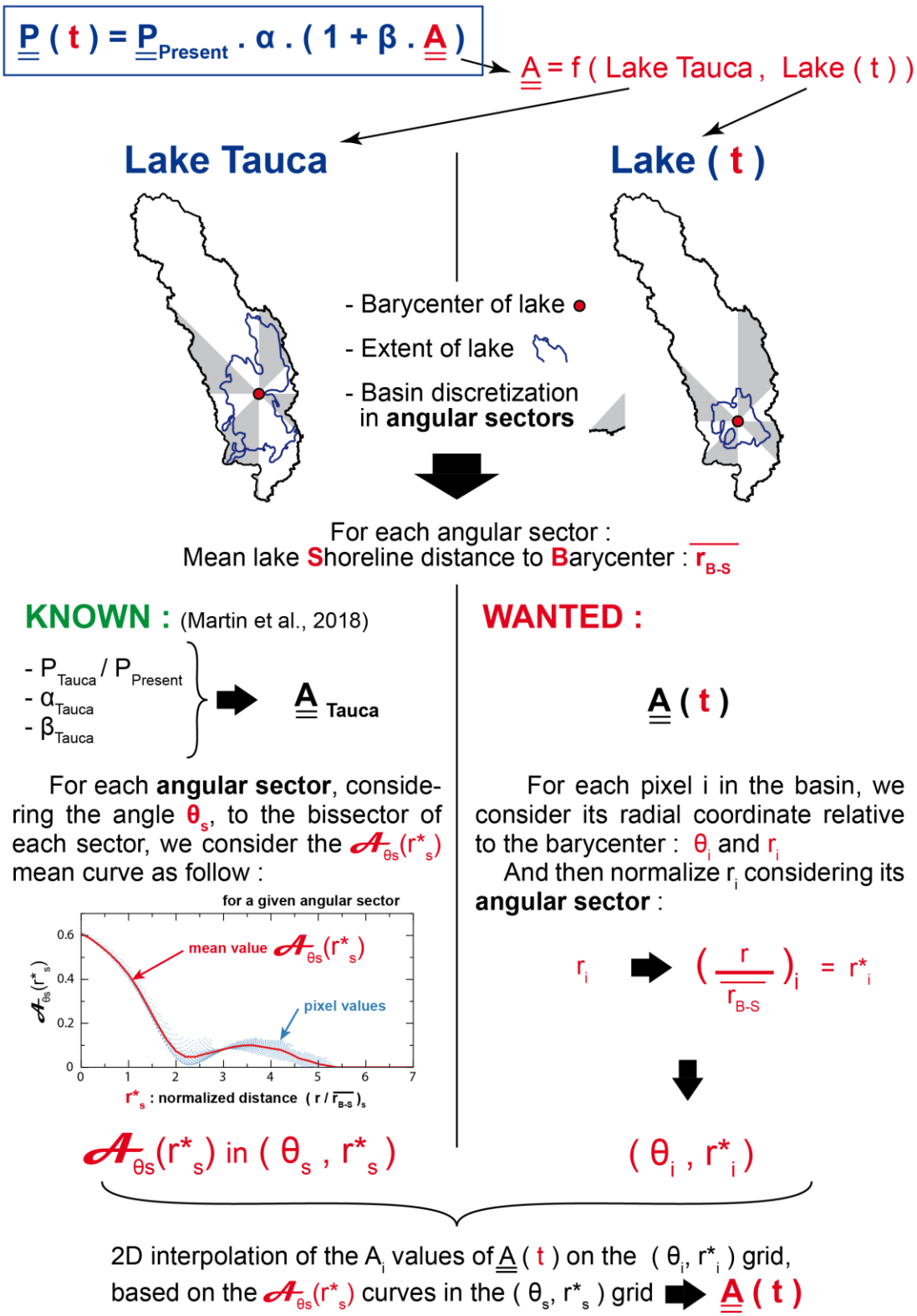

Figure S3. Workflow to compute the precipitation anomaly grid. The workflow describes the computation of matrix A as described in Section 3.3.5 and Equation (3). Matrix A was computed based on the Tauca highstand case study of Martin et al. (2018). The matrix A for the Tauca highstand was discretized from the barycenter of Lake Tauca into different angular sectors ("pie slices") such that it can be summed as a set of curves describing the decrease of A with distance from the barycenter. These curves were then used for any lake configuration during the last deglaciation by employing a scaling procedure that accounts for the location of the lake and its spatial extent. We note that for legibility, the schematic diagram s divided into eight angular sectors instead of the twenty used in the computation.

S.4. Calculation of the lake-induced precipitation Anomaly, calibration of the β parameter

Based on empirical precipitation data for present-day lakes, the amplification value β seems to be linked to lake size (Table S4, Fig. S4). Because the sizes of Lake Coipasa (32,300 km^2) and Lake Tauca (52,000 km^2) differ, and because we also dealt with their transgressive and regressive states synchronous with the reported ice extents, we calibrated β to account for this size-dependence (see Section 3.3.5 and Equation 4) using the data presented in Table S4 and Figure S4.

Lake	Surface (km^2)	Observed β	Uncertainty
Lake Mweru	5022	0.2	0.1
Lake Titicaca	8562	0.4	0.1
Lake Malawi	29429	0.8	0.1
Lake Victoria	68800	0.9	0.1

Table S4. Dataset used to empirically calibrate β. Source: www.lakebasin.org.

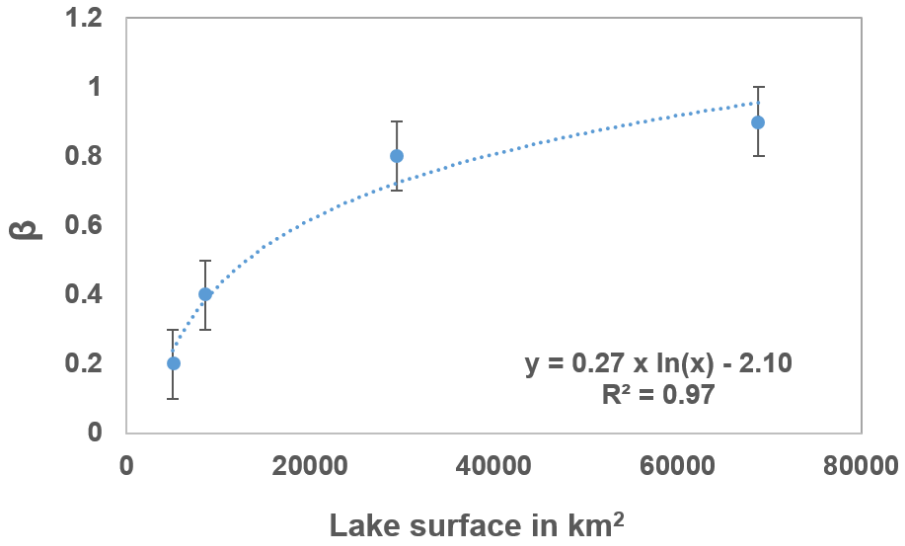

Figure S4. Calibration of the precipitation amplification factor β against lake size (surface area km^2).

S.5. Impact of the scaling scheme model on the CRE age computations

To assess the dependence of the computed ages to the scaling procedure, we used CREp (https://crep.otelo.univ-lorraine.fr) to re-compute all the ages of this study using a different scaling framework. In Fig. S5, we compare the ages obtained with the Lal/Stone ('Lm') time-dependent scaling model (Balco et al., 2008) and the geomagnetic database of Muscheler et al. (2005) to those obtained with the LSD scaling model (Lifton et al., 2014) and the Lifton (2016) geomagnetic database. Both calculations rely on the ERA40 atmospheric database (Uppala et al., 2005). This comparison demonstrates that our results show little dependence on the scaling procedure. The Lm scaling tends to produce ages 400 years older than the LSD scaling. Given the uncertainties on the measurements, this difference indicates that 90% of the computed ages are compatible within 1σ. For the other 10%, the average 1σ incompatibility is 100 years. Hence, the CRE ages have very limited model dependence, underlying the robustness of the reported glacial chronologies.

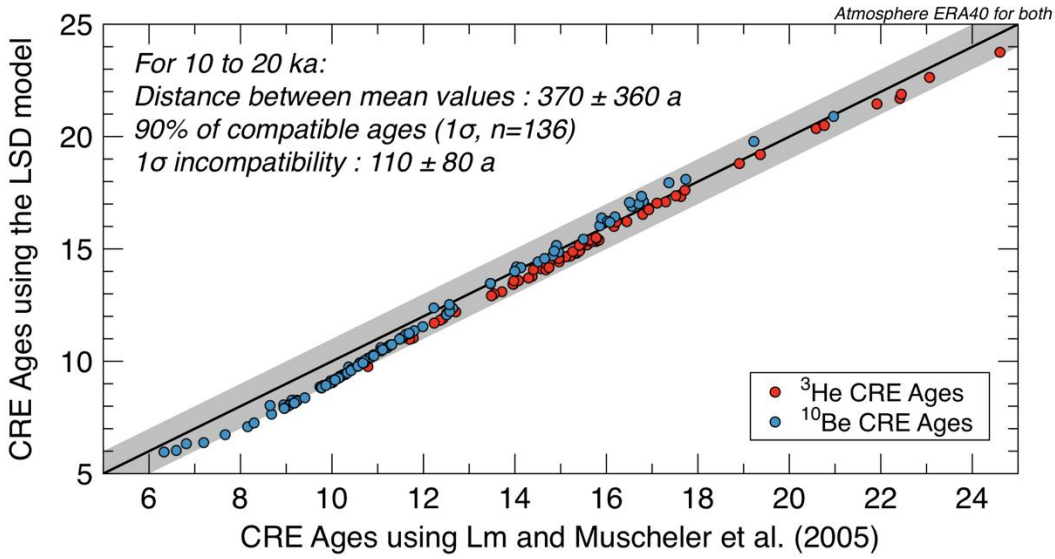

Figure S5. Comparison between two scaling procedures to compute CRE ages with the CREp online calculator (https://crep.otelo.univ-lorraine.fr). For this study, we used the Lm scaling model (Balco et al., 2008) and the geomagnetic database of Muscheler et al. (2005). We compare our results to those obtained using the LSD scaling model (Lifton et al., 2014) and the geomagnetic data compiled by Lifton (2016). We used the spatialized atmosphere ERA40 (Uppala et al., 2005) for both calculations

S.6. Illustration of the Bayesian filtering process on the age data

Figure S6 schematically illustrates how stratigraphic relations between moraines are used to filter the age PDFs.

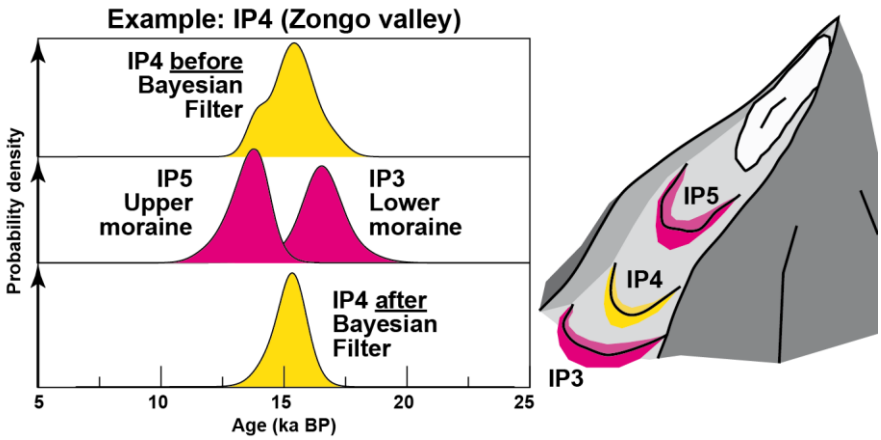

Figure S6. Illustration of the Bayesian filtering process in the case of moraine IP4 in Zongo Valley. The raw age distribution of the upper and lower moraines that stratigraphically bracket IP4 are used to filter the raw age distribution of IP4 and improve the accuracy of its age.